Università degli Studi di Udine
Dottorato di Ricerca in
Scienze dell'Ingegneria Energetica e Ambientale
XXXIV Ciclo

Technische Universität Wien
Doktoratsstudium der
Technischen Wissenschaften Maschinenbau

Interaction of thermal and solutal stratification with turbulence in wall-bounded flows

Pejman Hadi Sichani

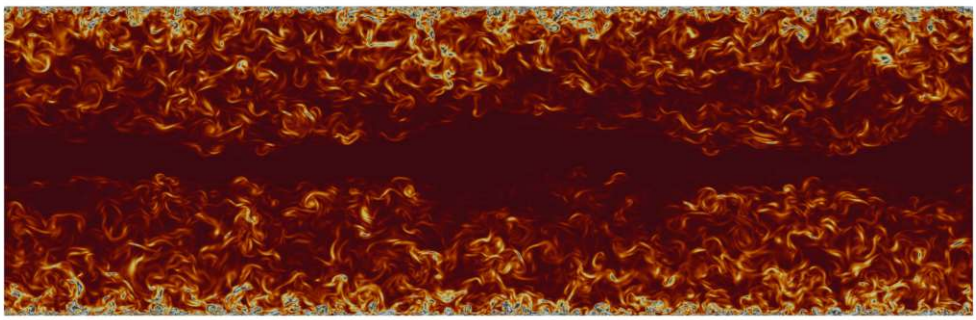

BOARD MEMBERS

Prof. Colm-Cille Patrick Caulfield	Reviewer
Prof. Herman Clercx	Reviewer
Prof. Manuel García-Villalba	Committee member
Prof. Maurizio Quadrio	Committee member
Prof. Herbert Steinrück	Committee member
Prof. Alfredo Soldati	Supervisor
Prof. Cristian Marchioli	Supervisor
Dr. Francesco Zonta	Co-Supervisor
Prof. Cristian Marchioli	Doctorate Chair

Author's e-mail:
hadisichani.pejman@spes.uniud.it
pejman.sichani@tuwien.ac.at

Author's address:
Dipartimento Politecnico di Ingegneria e Architettura
Università degli Studi di Udine
Via delle Scienze 206
33100 Udine, Italy
Web: `DIEGM - University of Udine`

Institute of Fluid Mechanics and Heat Transfer
Technische Universität Wien
Getreidemarkt 9/E322
1060 Wien, Austria
Web: `ISW - TU Wien`

Cover:
Instantaneous two-dimensional rendering maps of turbulent viscous dissipation, ϵ_k, on a cross-section located at the channel center ($Re_\tau = 1000$, $Ri_\tau = 300$ and $Pr = 0.71$). Dark red corresponds to zero and light blue to the maximum magnitude of turbulent viscous dissipation. The stratification is strong enough to suppress the turbulence activity at the channel center completely.

Abstract

In this thesis, we investigate numerically the physical mechanisms that govern the dynamics of a stratified fluid flow. Two different cases of practical interest are considered: stable thermal stratification in wall-bounded turbulence, and double diffusive convection (DDC) subject to shear in a confined fluid layer. We first investigated the interaction between stable thermal stratification and wall-bounded turbulence. Current physical mechanisms and scaling laws in stratified channel turbulence have been tested by Direct Numerical Simulations (DNS) up to shear Reynolds number $Re_\tau = 550$. In this study, we aim at extending present results to higher Reynolds numbers, by running a series of DNSs of stratified channel turbulence at $Re_\tau = 1000$ and shear Richardson number – which measures the relative importance of buoyancy compared to inertia – in the range $0 \leq Ri_\tau \leq 300$. By increasing stratification, active turbulence is sustained only in the near-wall region, whereas intermittent turbulence, modulated by the presence of non-turbulent wavy structures (Internal Gravity Waves, IGW), is observed at the channel core. In such conditions, the wall-normal transport of momentum and heat is considerably reduced compared to the case of non-stratified turbulence. A careful characterization of the flow-field statistics shows that, despite temperature and wall-normal velocity fluctuations being very large at the channel center, the mean value of their product – the buoyancy flux – vanishes for $Ri_\tau \geq 200$. We show that this behavior is due to the presence of a $\sim \pi/2$ phase delay between the temperature and the wall-normal velocity signals: when wall-normal velocity fluctuations are large (in magnitude), temperature fluctuations are almost zero, and viceversa. This constitutes a blockage effect to the wall-normal exchange of energy. In addition, we present the scaling law for friction factor C_f, and we propose a new scaling for the Nusselt number, Nu. These scaling laws, which seem robust over the explored range of parameters, complement and extend previous experimental and numerical data up to $Re_\tau = 1000$, and are expected to help the development of improved models and parametrizations of stratified flows at large Re_τ. We also investigate the energetics and mixing in wall-bounded stably stratified turbulence, and we propose a new parameterization for the irreversible flux Richardson number R_f^* – which is a measures for irreversible mixing – as a function of gradient Richardson number Ri_g. In the second part of this thesis, we examine the effect of mixed slip/no-slip boundary conditions on DDC subject to shear in a confined fluid layer. DDC results from the competing action of a stably stratified, rapidly-diffusing scalar (temperature) and an unstably stratified, slowly diffusing scalar (salinity), which is characterized by fingering instabilities. This problem has five governing parameters: The salinity Prandtl number, Pr_s (momentum to salinity diffusivity ratio); the salinity Rayleigh number, Ra_s (measure of the fluid instability due to salinity differences); the Lewis number, Le (thermal to salinity diffusivity ratio); the density ratio, Λ (measure of the effective flow stratification), and the shear rate, Γ. We investigate fingering dynamics at varying shear rate via highly-resolved numerical simulations. Simulations are performed at fixed Pr_s , Ra_s ,

Le and Λ, while the effect of shear is accounted for by considering different values of Γ. Preliminary results show that shear tends to damp the growth of fingering instability, leading to highly anisotropic DDC dynamics associated with the formation of regular salinity. In turn, these dynamics result in significant modifications of the vertical heat transport and solute concentration.

Contents

1 Introduction

When the fluid density increases with depth (the acceleration due to gravity points downwards), the fluid is said to be stably stratified. A schematic of a stably stratified fluid, where light fluid is located on top of heavy fluid, is illustrated in Fig. 1.1. Consider a small fluid parcel, shown in Fig. 1.1. Suppose the fluid parcel is raised adiabatically a small distance above its initial position, without exchanging mass with its surroundings. At the new position, the density of the fluid parcel is higher than that of its surroundings, and the fluid parcel experiences a downward buoyancy force. This buoyancy force tends to bring the fluid parcel back to its initial position, and therefore the equilibrium is stable. Stable stratification can be observed in a wealth of situations in which the underlying flow is turbulent. Stably stratified turbulence occurs in both unbounded [61, 93, 62] and bounded [106, 107, 16] configurations (for further details see [142]).

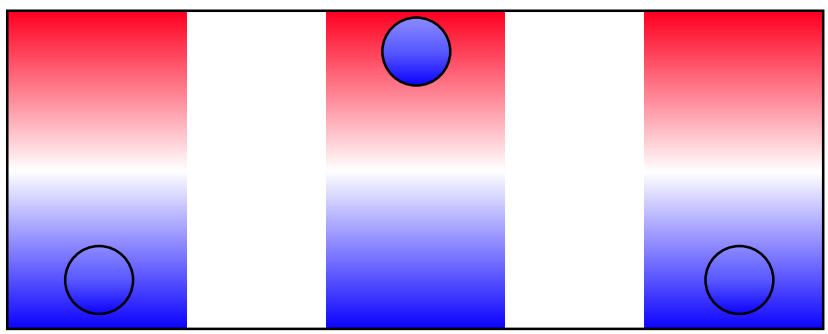

FIGURE 1.1 – Schematic of a stably stratified fluid, where warm fluid is located on top of the cold fluid.

In this thesis, we are particularly concerned with the occurrence of stably-stratified turbulence in a channel confined by two solid walls. The flow is heated from the top and cooled from the bottom so that warm and thus lighter fluid overlays cold and thus heavier fluid. This flow is subject to a vertical (wall-normal) buoyancy force that, interacting with turbulence, can strongly change momentum, energy and mass transport. The study of stably-stratified turbulence in presence of boundaries is of

great importance in a number of industrial and environmental processes, from energy supply/removal in heat transfer equipments and chemical/nuclear reactors [19, 86], to weather forecasting [99] or pollutant dispersion in the atmospheric boundary layer [97]. The complex physics of wall-bounded stably-stratified turbulence is governed by the interplay between inertial and buoyancy forces, flavored also by the presence of viscous forces and thermal diffusion. This interplay is commonly quantified in terms of three main dimensionless numbers: the Reynolds number Re – ratio of inertial to viscous forces –, the Richardson number Ri – ratio of buoyancy to inertial forces – and the Prandtl number Pr – ratio of momentum to thermal diffusivities.

Since the first works of Monin & Obukhov [73] and Bolgiano [10], which were motivated by the study of the atmospheric boundary layer, a number of field measurements, experiments, simulations and theoretical models have been developed [22, 142, 15], with the main purpose of inferring flow stability properties and suitable scaling laws for the relevant global quantities (i.e. energy/momentum fluxes, length scales, mixing efficiency) as a function of the observed/imposed stratification. Reportedly, detailed experimental measurements of stratified flows, in particular in proximity of a wall, are extremely challenging and difficult to realize when non-optical techniques are employed [3, 54, 78]. Yet, accurate measurements by optical techniques have become available only recently [129], and have contributed a lot to the advancement in the field, though their accuracy in the near wall region remains still problematic.

In this context, numerical simulations – granting access to the entire velocity and temperature field down to the region very close to the wall – have emerged as a valuable tool to understand and characterize the local as well as the global structure of the flow. It is therefore not surprising that Large Eddy Simulations and Direct Numerical Simulations (LES and DNS) of thermally stratified channel turbulence have been performed more and more frequently in the last twenty years. Among the first numerical studies of wall-bounded stratified flows, Garg et al. [29] employed wall-resolved LES to compute the dynamics of incompressible stratified turbulence in both close and open channel flow configurations at a constant Reynolds and Prandtl numbers ($Re_\tau = 180$ and $Pr = 0.71$) but at different Richardson number Ri_τ (i.e., different stratification levels). Note that subscript τ indicates parameters expressed in wall-units, i.e. using the shear velocity u_τ as reference velocity. Based on the value of Ri_τ, the flow was divided into a buoyancy-affected flow ($Ri_\tau < 30$, characterized by general turbulence attenuation), a buoyancy-controlled flow ($30 < Ri_\tau < 45$, with the possibility of transient and local flow relaminarization) and a buoyancy-dominated flow ($Ri_\tau > 45$, with a complete flow relaminarization). Similar trends, showing the occurrence of local flow laminarization, were observed by Iida et al. [46] in their DNSs of stratified channel turbulence at similar Reynolds and Richardson numbers ($Re_\tau = 150$, $Ri_\tau \leq 40$). As discussed by Armenio & Sarkar [2], such findings were however in contrast with the linear stability analysis of Gage & Reid [26] that, compared to the results of Garg et al. [29] and Iida et al. [46], predicted a complete flow laminarization to occur only at much higher values of Ri_τ. A clearcut explanation of this inconsistency was given only later [72, 28]. In particular, performing DNS of stratified channel turbulence up to $Re_\tau = 550$ and $Ri_\tau = 960$, and employing large computational domains, García-Villalba & del Álamo [28] were able to show that the local flow laminarization at subcritical values of Ri_τ occurs when the computational domain is not large

enough to contain the minimal flow unit required to sustain turbulence. In such an instance, laminar patches appear, increase in size, and become as large as the entire computational domain, hence making a back transition to turbulence – which would be observed in larger computational domains – not possible.

All previous studies were particularly important since they demonstrated not only that the overall momentum and heat transfer rates are reduced for increasing stratification, but also that the structure of wall-bounded turbulence can be selectively modified. The current state of DNS research in the field of stably-stratified channel turbulence is summarized in the (Re_τ, Ri_τ) phase space diagram shown in Fig. 1.2 [adapted from 142]. The black solid line represents the boundary ideally separating the laminar region (above the curve), from the turbulent one (below the curve). This curve, which has been obtained by best fit of data reported in [26], should not be taken as a sharp boundary between two regimes, but more likely as a blurry transition region in which the flow is expected to (gradually) change behavior from turbulent to laminar flow. There is indeed strong evidence that, when the marginal stability curve is approached, the flow becomes intermittent (stratification is so strong that laminar patches appear in the near wall-region, although the mean flow is still able to sustain turbulence, see [28, 12]). The symbols below the curve represent previous DNS simulations [46, 72, 137, 28, 144], which reach the maximum Reynolds number $Re_\tau = 550$. Simulations at a larger Reynolds number were performed more recently by other authors [17, 38, 130], but in different flow configurations (i.e. Couette flow or open channel). For weakly to moderate stratification, buoyancy-driven wave like motions (Internal Gravity Waves, IGW) appear at the channel core and coexist with classical near-wall turbulence (see inset "Flow 1" below the curve highlighting the presence of IGW via visualization of temperature contours on a longitudinal section of the channel). In this case, statistics still scale well in wall units. As already mentioned, when stratification is increased so to approach the marginal stability curve, the situations is more complicated, since buoyancy is able to influence not only the flow region far from the boundary, but also the region close to it. This generally leads to the collapse of near wall turbulence and to the corresponding appearance of laminar patches. For very strong stratification – stronger than the critical strength dictated by the marginal stability curve –, the flow becomes laminar (see inset "Flow 2" above the curve, showing a complete laminarization of the flow). It is worth noting that there is still a bit of uncertainty about the complete relaminarization of strongly stratified flows. Recently, Donda et al. [18] have argued that the laminarization process induced by stratification is an inherently transient phenomenon, which is always followed by a recovery of turbulence provided that sufficiently large finite amplitude perturbation are imposed on the laminarized state and provided that sufficient time for flow acceleration is allowed [142].

With the final aim of assessing current physical description and corresponding parametrizations of stratified wall-bounded turbulence at high Reynolds numbers, we perform a series of DNS of stably-stratified channel flow at $Re_\tau = 1000$, i.e. well beyond the current state-of-the art limit of $Re_\tau = 550$ (see Fig. 1.2), and for $0 \leq Ri_\tau = 300$. Computations at high Reynolds number are crucial in this field, given the lack of indications that results obtained by low Reynolds number simulations can be upscaled to the scale of real phenomena, especially in environmental and

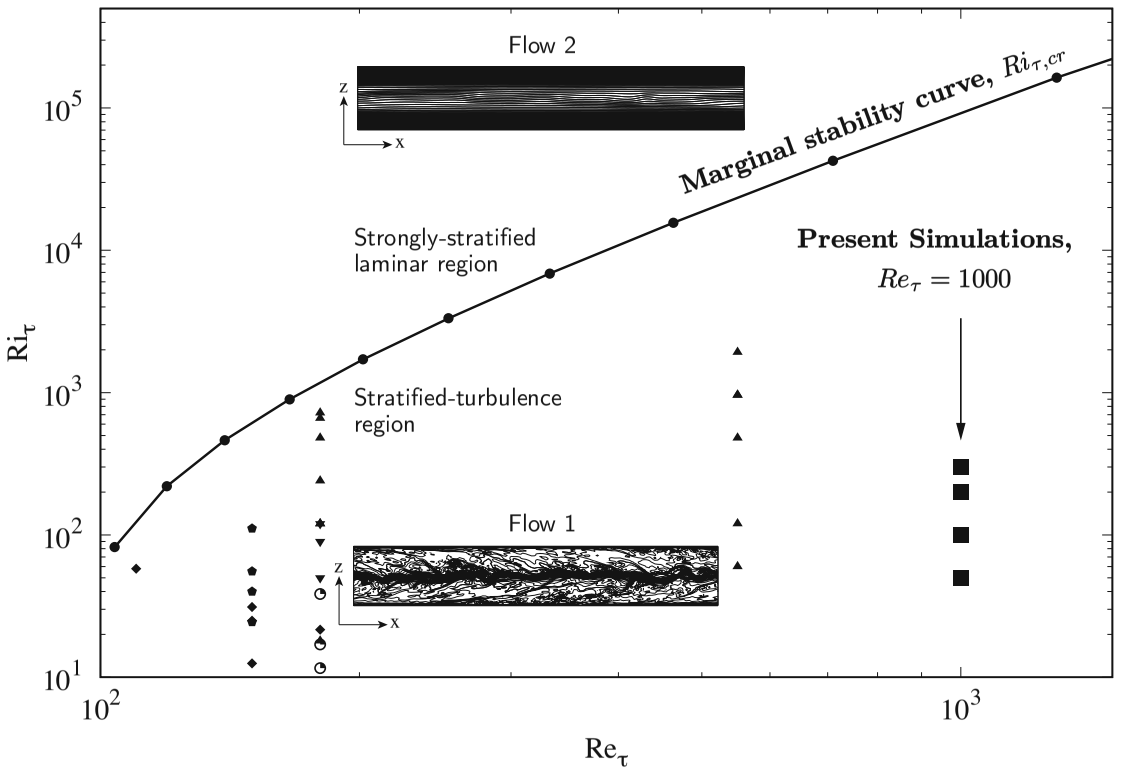

FIGURE 1.2 – Comprehensive sketch of the $(Re_\tau - Ri_\tau)$ diagram for stratified turbulence in closed channels [adapted from 142]. Circles represent the critical $Ri_{\tau,cr}$ (marginal stability curve) obtained from the linear stability analysis of [26], and properly rearranged to fit for the present parameter space. The proposed parametrization of the marginal stability curve (solid line) is: $\log(Ri_{\tau,cr}) = m \cdot [\log(Re_\tau)]^b + n \cdot [\log(Re_\tau) - d]^a + c$, where the value of the parameters is $a = -0.1843$, $b = 1.047$, $c = 1.914$, $d = 1.927$, $m = 1.651$ and $n = -2.204$ [142]. The symbols below the curve – in the range $0 \leq Re_\tau \leq 550$ – represent previous DNS simulations found in literature [28, 144, 137, 46, 72]. The simulations performed in this work are indicated by the filled squares (■). The two insets, labelled Flow 1 and Flow 2, are used to visualize the typical flow structure (temperature contours) in the stratified-turbulence region (Flow 1) and in the strongly-stratified laminar region (Flow 2).

large-scale industrial applications. The present study represents a first effort in this direction: The detailed dataset produced by the present computationally-intensive simulations at high Re_τ, can definitely help LES and RANS to develop reliable subgrid scale and turbulence closure models that properly account for buoyancy effects in realistic applications.

There are physical situations in which the fluid density depends on two scalar fields such as Double diffusion convection (DDC). These complex situations are ordinary occurrences in oceans, where temperature gradient is the stabilizing factor and salinity gradient produces instabilities. DDC is a mixing process driven by the difference in the molecular diffusivities of two scalar fields, such as heat and salt, within a confined fluid layer [90, 27, 91, 100]. When a fluid layer experiences an unstable gradient of the slowly-diffusing scalar and a stable gradient of the rapidly-diffusing scalar, a convective instability can occur: Such instability, referred to as fingering convection hereinafter [60], leads to the formation of narrow upgoing and downgoing columns of fluid that develop in the bulk of the flow and favour scalar transport across the layer [120, 64, 114]. The resulting flow structure is also characterized by the formation of a thin boundary layer of the slowly-diffusing scalar, which superposes to the velocity boundary layer [135]. Because of its relevance in many important applications, ranging from mixing in large water bodies [90, 82, 109] to electrodeposition cells [52], double-diffusive convection has received a lot of attention since the pioneering works of Stern [112] and Turner [120]. When the diffusing scalars are temperature and salinity, in particular, scaling laws for key parameters of DDC (such as the non-dimensional salinity flux, the salinity Rayleigh number, which measures the strength of the salinity difference, and the density ratio of the buoyancy forces induced by two scalar differences) have been derived recently by Yang et al. [135], exploiting a generalisation of the Grossmann-Lohse theory originally developed for traditional Rayleigh-Bénard convection [136]. The driving mechanism for DDC in the fingering regime is shown in Fig. 1.3 schematically. Consider a small fluid parcel in a system in which the warm salty fluid is located on top of the cold fresh fluid. Assume that the parcel of fluid is displaced downward (the acceleration due to gravity points downwards). Since temperature is the rapidly diffusing scalar, the fluid parcel rapidly exchanges heat with its surroundings, so to reach the thermal equilibrium. Differently from the temperature, the solutal concentration of the parcel does not reach the equilibrium state as quickly as the temperature due to the low molecular diffusivity of the salt. When the fluid parcel is cooled to the point where its temperature becomes equal to its surroundings, the parcel's density exceeds the density of the surrounding fluid, and the parcel proceeds to sink further.

In some situations, e.g. buoyant outflows in water bodies, double-diffusive convection is affected by shear, which can be produced by bulk motion of water masses like those produced by adjacent intruding layers [55, 117, 92]. The effect of shear on the growth of double-diffusive convection has been the subject of several studies (from the pioneering work of Linden [63], who focused on eddies impinging upon a density step where salt fingers were growing, to the more recent numerical works by Smyth & Kimura [104, 105], Radko et al. [92], and Konopliv et al. [55] and experimental works by Wells et al. [128] and Fernandes & Krishnamurti [21]. The main effect observed in both laboratory and numerical investigations was the alignment of the fingers in

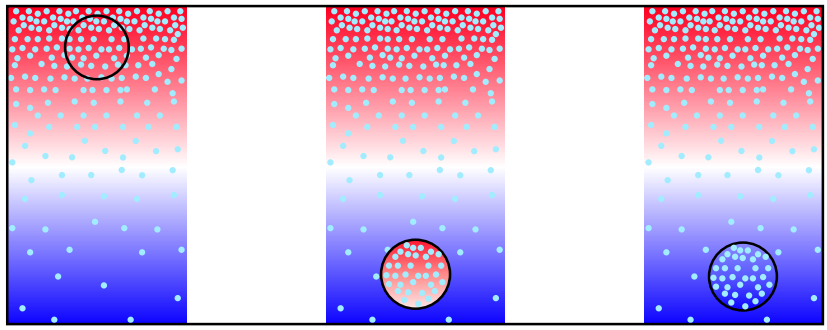

FIGURE 1.3 – Schematic of the driving mechanism for DDC in the fingering regime.

the direction of shear, which leads to the formation of sheet-like structures and to a reduction of vertical double-diffusive transport rates compared to those measured in three-dimensional DDC in the absence of shear [92]. In the plane perpendicular to the direction of shear, however, double diffusion can still produce vertically-elongated filaments similar to those observed in zero-shear DDC [92]. It should be noted that most of the numerical investigations of DDC convection in shear flow were conducted using linear stability analysis [63, 117], which allows for the identification of the most unstable modes responsible for the onset of convection, or transient growth analysis [55], which was used to identify the maximum perturbation growth of the fingers by means of a suitably-defined optimization problem. Only a few studies are based on fully-resolved three-dimensional simulations of the flow. In particular, Smyth & Kimura [105] performed direct simulations of DDC in the presence of shear-induced Kelvin-Helmholtz instabilities, whereas Radko et al. [92] examined the case of DDC subject to stochastic shear. We also observe that a precise identification of shear effects on the local diffusive and convective contributions to the total scalar fluxes in the gravity direction is lacking, the discussion being focused on the global transport parameters of the flow (e.g. salinity and thermal Nusselt number). In the present work, we quantify the modifications on DDC induced by the superposition of a mean shear, which introduces a symmetry breaking effect into the flow. We also examine the resulting change in the scalar fluxes, determining the relative importance of their diffusive and convective parts. This problem is of relevance in a number of applications [109] and, to the best of our knowledge, is investigated here for the first time. To this aim, we perform fully-resolved three-dimensional simulations of double-diffusive convection within a fluid layer bounded by a solid (no-slip) wall at the bottom and a slip surface (mimicking a non-homogeneous convection layer associated with an anisotropic scalar distribution) at the top. The effect of a steady shear on fingering formation within a no-slip/slip layer is expected to magnify the asymmetric distribution of the diffusing scalars (temperature and salinity) across the layer, which is due to the fact that horizontal fluid motions are allowed at the slip boundary, yet forbidden at the no-slip boundary. This flow configuration allows us to complement previous studies of DDC between two no-slip walls (see [37, 133, 6, 52] among others), or two free-

slip walls [82] or between a no-slip wall and a flux-free boundary [105]. Indeed, as demonstrated by Yang et al. [134] for the case of zero-shear vertically-bounded DDC in the fingering regime, comparison of different boundary conditions allows deeper physical understanding of fingering dynamics. In addition, our study could provide useful indications regarding the applicability of laboratory experiments, which are usually performed between no-slip walls, and of numerical studies, which use the free-slip condition to approximate an interface in natural environments, to actual DDC flows (like those occurring in water bodies). As mentioned, an important feature of this flow is the contribution to salinity transport given by diffusive and convective mechanisms, which will be analyzed in separation. We will discuss how these two contributions can influence each other and, at the same time, be influenced by the applied shear. We will also show how the resulting complex interplay can lead to interesting phenomena such as the occurrence of local counter gradient diffusive fluxes: These may influence the global heat and mass transfer rates leading to quantitative changes in the Nusselt numbers.

Thesis outline

- **Chapter 2: Mathematical and physical description of stratified shear flows**

  In this chapter, the physical and mathematical models used to describe the dynamics of stratified shear flows are presented. The governing equations of stably-stratified turbulence and DDC under Oberbeck-Boussinesq (OB) approximation are introduced. The validity range of OB approximation is briefly discussed, and adimensionalization of the variables is presented.

- **Chapter 3: Methodology**

  In this chapter, the discretization of governing equations, the numerical method and its implementation are reported. The solution procedure is discussed in details and the spectral representation of the equations are shown. In the last part, the performances of the numerical implementation is investigated.

- **Chapter 4: Interaction between stable stratification and turbulence**

  In this chapter, building on top of a detailed analysis of the flow-field structure and statistics, we discuss the influence of stratification on the wall-normal transport of momentum and heat, and we present possible parametrizations and scaling laws for the friction factor and for the Nusselt number. We also briefly discuss the effect of buoyancy on eddy size using energy spectral density analysis.

- **Chapter 5: Energetics and mixing in wall-bounded stably-stratified turbulence**

  In this chapter, the energy budget equations are introduced. The effect of stratification on sink/source terms of different energy budget equations is examined. The irreversible mixing in stably-stratified turbulence is quantified using irreversible flux Richardson number and a new parametrizations is presented for

the irreversible flux Richardson number as a function of gradient Richardson number.

- **Chapter 6: Shear effects on double diffusive convection**

  In this chapter, we investigate the influence of shear on DDC. We discuss the flow structure and the observed fingering dynamics first, complementing this phenomenological description with a statistical characterization of velocity, temperature and salinity distributions as well as heat and salinity fluxes.

2

Mathematical and physical description of stratified shear flows

This chapter presents the physical and mathematical description of stratified shear flows. In section 2.1, we demonstrate the physical and mathematical models used to describe wall-bounded stably stratified turbulent flows. We introduce the general compressible form of the governing equations (Non-Oberbeck-Boussinesq, NOB) in subsection 2.1.1. In subsection 2.1.2, we briefly present the Oberbeck-Boussinesq (OB) approximation and the assumptions on which OB approximation is based. We introduce the governing equations under OB approximation in a dimensional form in subsection 2.1.3. Finally, we discuss the ranges of validity of the OB approximation in subsection 2.1.4. In section 2.2, introduce the governing equations for a DDC problem. Specifically, we introduce the governing equations of a DDC system in the dimensional form under OB approximation in subsection 2.2.1. Finally, we introduce two different scalings employed in the framework of this thesis to prescribe the imposed shear to a DDC configuration in subsection 2.2.2.

2.1 Stably-stratified turbulence

2.1.1 General Form of the Governing Equations

The complete system of continuity, momentum and energy equations for a Newtonian fluid with variable properties and a second viscosity [119] equal to zero represents the most common starting point for the analysis of stably-stratified turbulence [7]. This set of equations in dimensional form (denoted by the superscript *) is:

$$\frac{D\rho^*}{Dt^*} + \rho^* \frac{\partial u_i^*}{\partial x_i^*} = 0 \,, \tag{2.1}$$

$$\rho^* \frac{Du_i^*}{Dt^*} = -\frac{\partial P^*}{\partial x_i^*} - \rho^* g^* \delta_{3,i}^* + \mu^* \frac{\partial \Gamma_{ij}^*}{\partial x_j^*} + \Gamma_{ij}^* \frac{\partial \mu^*}{\partial x_j^*} \,, \tag{2.2}$$

$$\rho^* c_p^* \frac{D\theta^*}{Dt^*} = \lambda^* \frac{\partial^2 \theta^*}{\partial x_j^{*2}} + \frac{\partial \lambda^*}{\partial x_j^*} \frac{\partial \theta^*}{\partial x_j^*} + \beta_\theta^* \theta^* \frac{DP^*}{Dt^*} + \mu^* \Phi^* \ , \tag{2.3}$$

where u_i^* is the i^{th} component of the velocity vector, P^* is pressure, θ^* is temperature and g^* is the gravitational acceleration. Note that

$$\Gamma_{ij}^* = \frac{\partial u_i^*}{\partial x_j^*} + \frac{\partial u_j^*}{\partial x_i^*} - \frac{2}{3} \frac{\partial u_k^*}{\partial x_k} \delta_{ij}^*, \quad \Phi^* = \frac{1}{2} \Gamma_{ij}^* \left(\frac{\partial u_i^*}{\partial x_j^*} + \frac{\partial u_j^*}{\partial x_i^*} \right) \tag{2.4}$$

are the rate of strain tensor (Γ_{ij}^*) and the rate of dissipation of mechanical energy due to viscosity (Φ^*). The thermophysical fluid properties are density ρ^*, viscosity μ^*, specific heat c_p^*, thermal conductivity λ^* and thermal expansion coefficient $\beta_\theta^* = -1/\rho^* \left(\partial \rho^* / \partial \theta^*\right)_p$. Definition of fluid properties as a function of temperature and pressure is required for a full specification of the problem. To this aim, suitable laws for the determination of the fluid properties are given in form as [142]

$$\begin{gathered} \rho^* = \rho^*(\theta^*, P^*); \quad c_p^* = c_p^*(\theta^*, P^*); \quad \mu^* = \mu^*(\theta^*, P^*) \\ \beta_\theta^* = \beta_\theta^*(\theta^*, P^*); \quad \lambda^* = \lambda^*(\theta^*, P^*). \end{gathered} \tag{2.5}$$

Analytical expressions and correlations derived from thermodynamics and/or experimental measurements [5, 98, 74, 143, 144] are commonly employed to define Eq. 2.5. The general form of the governing equations is given by Eqs. 2.1-2.3, which are complemented with explicit laws to particularize Eq. 2.5 [142].

2.1.2 Oberbeck-Boussinesq (OB) approximation

It is not only required to have a gravity field for a buoyancy-driven flow to occur, but it is also crucial to have density variation. It should be noted that the density variation is different from the variable density in a flow field. The exact governing equations are uncompromising, and therefore some approximations are required. The Oberbeck-Boussinesq (OB) approximation [77, 11] is the simplest approximation that includes buoyancy in the physics of the flow. It is the basis of most of what is known about natural convection [34]. The OB approximation is built on top of the hypothesis that the fluid density fluctuations are small enough to be neglected in the continuity equation and only play a role in the gravitational term of the momentum equation (i.e., where ρ^* is multiplied by the acceleration due to gravity g^*) [142]. The assumption of a constant ρ^* but in the gravitational term is possible to be made because the acceleration due to gravity is in general much larger than any other local value of the fluid acceleration (i. e. $|g^*| \gg |Du_i^*/Dt^*|$), and therefore the product $\rho^* g^*$ can produce large effects even when relative density fluctuations with respect to the reference density ρ_0^* are very small (i.e. $\left(\rho^* - \rho_0^*\right)/\rho_0^* \ll 1$) [142]. By employing the OB approximation, all thermophysical properties of the fluid are assumed to be constant and uniform.

2.1.3 Governing Equations

We consider a stably stratified turbulent flow inside an horizontal straight channel, shown in Fig. 2.1. The channel is bounded by two solid walls at $z = \pm h^*$, with h^* being

the channel half height. The origin of the coordinate system is located at the center of the channel and the $x-$, $y-$ and $z-$axes point in the streamwise, spanwise and wall-normal directions, respectively. Note that, throughout this thesis, the position vector (x_1, x_2, x_3) and the velocity vector (u_1, u_2, u_3) are also referred to as (x, y, z) and (u_x, u_y, u_z), respectively. A stable stratification in the wall-normal direction z is maintained by keeping a positive temperature difference $\Delta\theta^* = \theta_t^* - \theta_b^*$ between the top (fixed temperature θ_t^*) and the bottom (fixed temperature θ_b^*) walls. At the same time, the flow is driven along the streamwise direction x by an imposed mean pressure gradient. The governing balance equations 2.1-2.3 under OB approximation in dimensional form and in tensor notation (repeated index implies summation) read as

$$\frac{\partial u_i^*}{\partial x_i^*} = 0 \,, \tag{2.6}$$

$$\rho^* \frac{\partial u_i}{\partial t^*} = -\rho^* u_j^* \frac{\partial u_i^*}{\partial x_j^*} + \mu^* \frac{\partial^2 u_i^*}{\partial x_j^{*2}} - \frac{\partial p^*}{\partial x_i^*} + \left(\rho^* - \rho_{ref}^*\right) g^* + \delta_{1,i}^*, \tag{2.7}$$

$$\rho^* c_p^* \frac{\partial \theta^*}{\partial t^*} + \rho^* c_p^* u_j^* \frac{\partial \theta^*}{\partial x_j^*} = \lambda^* \frac{\partial^2 \theta^*}{\partial x_j^{*2}}, \tag{2.8}$$

where p^* is the fluctuating kinematic pressure and $\delta_{1,i}^*$ is the mean pressure gradient that drives the flow (note that $\delta_{i,j} = 1$ if $i = j$, while $\delta_{i,j} = 0$ if $i \neq j$).

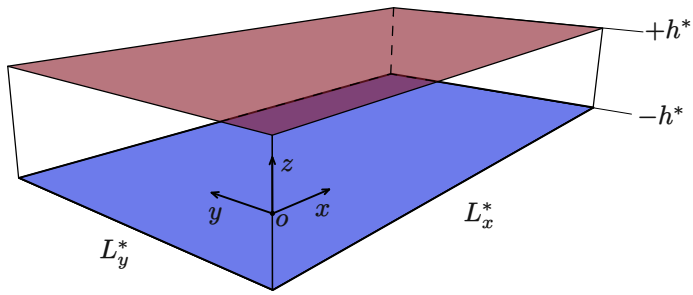

FIGURE 2.1 – Sketch of the computational domain used to run the simulations of stably-stratified turbulent channel flow. The closed channel is bounded by solid walls at $z = \pm h^*$. The channel has dimensions L_x^* in the streamwise direction (x^*), L_y^* in the spanwise direction (y^*) and $2h^*$ in the wall-normal direction (z^*). The reference frame is centered in o, located at the channel mid-plane.

Variables are made dimensionless as follows:

$$\begin{aligned} &\rho = \frac{\rho^*}{\rho_0^*}; \quad \mu = \frac{\mu^*}{\mu_0^*}; \quad \lambda = \frac{\lambda^*}{\lambda_0^*}; \quad c_p = \frac{c_p^*}{c_{p,0}^*}; \quad x_i = \frac{x_i^*}{h^*}; \\ &u_i = \frac{u_i^*}{u_\tau^*}; \quad t = \frac{t^* u_\tau^*}{h^*}; \quad p = \frac{p^*}{\rho_0^* u_\tau^{*2}}; \quad \theta = \frac{\theta^* - \theta_0^*}{\Delta\theta^*/2}. \end{aligned} \tag{2.9}$$

The reference velocity for adimensionalization is the friction velocity $u_\tau^* = \sqrt{\frac{\tau_w^*}{\rho_0^*}}$, where τ_w^* is the shear stress at the wall, whereas the reference temperature is the centerline

temperature $\theta_0^* = (\theta_t^* + \theta_b^*)/2$. Note that subscript 0 is used to represent thermophysical fluid properties at the reference temperature.

With the assumption of uniform thermophysical properties, the governing balance equations (Eq. 2.6-2.8) in dimensionless form read as:

$$\frac{\partial u_i}{\partial x_i} = 0 \,, \tag{2.10}$$

$$\frac{\partial u_i}{\partial t} = S_i + \frac{1}{Re_\tau}\left(\frac{\partial^2 u_i}{\partial {x_j}^2}\right) - \frac{\partial p}{\partial x_i} \,, \tag{2.11}$$

$$\frac{\partial \theta}{\partial t} = S_\theta + \frac{1}{Re_\tau Pr}\left(\frac{\partial^2 \theta}{\partial {x_j}^2}\right). \tag{2.12}$$

The S-terms contain the non-linear convective terms, the dimensionless mean pressure gradient and the buoyancy term:

$$S_i = -u_j \frac{\partial u_i}{\partial x_j} + \delta_{i,1} + \delta_{i,3} Ri_\tau \theta, \tag{2.13}$$

$$S_\theta = -u_j \frac{\partial \theta}{\partial x_j} \,. \tag{2.14}$$

In the above equations, $\delta_{i,3}$ is the Kronecker delta (used to account for the buoyancy term in the wall-normal direction only), whereas

$$Re_\tau = \frac{u_\tau^* h^*}{\nu_0^*}, \quad Pr = \frac{\mu_0^* c_{p,0}^*}{\lambda_0^*}, \quad Ri_\tau = \frac{g^* \beta_{\theta_0}^* \frac{\Delta\theta^*}{2} h}{{u_\tau^*}^2}, \tag{2.15}$$

are respectively the shear Reynolds number, the Prandtl number and the shear Richardson number, defined in terms of the thermophysical properties at the reference temperature θ_0^*. In the above dimensionless parameters, $\beta_{\theta_0}^*$ and ν_0^* are the thermal expansion coefficient and the kinematic viscosity at the reference temperature, and are defined as

$$\beta_\theta^* = -\frac{1}{\rho^*}\left(\frac{\partial \rho^*}{\partial T^*}\right)_p; \quad \nu_0^* = \frac{\mu_0^*}{\rho_0^*}. \tag{2.16}$$

Eqs. 2.10-2.14 include buoyancy effects. However, the same equations can be used to analyze neutrally-buoyant flows, simply assuming a vanishing shear Richardson number ($Ri_\tau = 0$).

In the numerical simulations of wall-bounded stratified flows [29, 2, 28], Ri_τ is commonly used to characterize the flow regimes. Unlike numerical simulations, using Ri_τ in experiment deals with some limitations. These limitations in experiments are linked to the difficulty in the determination of the shear velocity u_τ (it requires precise evaluation of the wall shear stress). Therefore, in experiments the bulk Richardson number Ri_b is usually preferred, since the bulk velocity is an easier quantity to access [142].

2.1.4 Range of validity of the approximate equations

Albeit simple, the OB approximation (Eqs. 2.10-2.14) was extensively used to investigate important flow physics in the broad field of buoyancy-influenced flows [8, 32, 121]. It is important to note that OB approximation can only represent a good approximation of the exact equations (Eqs. 2.1-2.3) within specific ranges of variation of the key parameters [110, 70, 34, 75, 76], and therefor employing OB approximation beyond these ranges is not physically justified. The accuracy error caused by the assumption of constant density in the continuity equation can be evaluated by computing the ratio between the material derivative of density $\rho^{*^{-1}} D\rho^*/Dt^*$ and the divergence of the velocity field $\partial u_j^*/\partial x_j^*$ [57, 118]. By introducing suitable length (l_0^*), velocity (u_0^*) and temperature ($\Delta\theta_0^*$) scales, we get

$$\frac{\rho^{*^{-1}} D\rho^*/Dt^*}{\partial u_j^*/\partial x_j^*} = \frac{\beta_\theta^* D\theta^*/Dt^*}{\partial u_j^*/\partial x_j^*} \simeq \frac{\beta_\theta^* \Delta\theta^* \left(u_0^*/l_0^*\right)}{u_0^*/l_0^*} = \beta_\theta^* \Delta\theta^*. \tag{2.17}$$

Following assumptions are made for derivation of Eq. 2.17:

- u_0^* is small compared to the speed of sound c (Mach number $Ma = u_0/c < 0.3$).
- pressure variations in the fluid are slow compared to acoustic pressure waves.

The criteria for the OB approximation to be valid is $\beta_\theta^* \Delta\theta^* \ll 1$. This criteria represent only a rough estimate abut the boundaries for the validity of the OB approximation. Gray and Giorgini [34] introduced precise boundaries for the validity of the OB approximation by starting from the full non-linear equations in compressible form and writing all the fluid properties as a linear Taylor expansion of temperature and pressure, i.e.:

$$\begin{aligned}
\rho^* &= \rho_0^* \left[1 - \beta_0^* \left(\theta^* - \theta_0^*\right) + \gamma_0^* \left(P^* - P_0^*\right)\right], \\
c_p^* &= c_{p0}^* \left[1 - a_0^* \left(\theta^* - \theta_0^*\right) + b_0^* \left(P^* - P_0^*\right)\right], \\
\mu^* &= \mu_0^* \left[1 - c_0^* \left(\theta^* - \theta_0^*\right) + d_0^* \left(P^* - P_0^*\right)\right], \\
\beta_\theta^* &= \beta_{\theta_0}^* \left[1 - e_0^* \left(\theta^* - \theta_0^*\right) + f_0^* \left(P^* - P_0^*\right)\right], \\
\lambda^* &= \lambda_0^* \left[1 - m_0^* \left(\theta^* - \theta_0^*\right) + n_0^* \left(P^* - P_0^*\right)\right],
\end{aligned} \tag{2.18}$$

where

$$\begin{aligned}
a^* &= \frac{1}{c_p^*}\frac{\partial c_p^*}{\partial \theta^*}, \quad b^* = \frac{1}{c_p^*}\frac{\partial c_p^*}{\partial P^*}, \quad c^* = \frac{1}{\mu^*}\frac{\partial \mu^*}{\partial \theta^*}, \quad d^* = \frac{1}{\mu^*}\frac{\partial \mu^*}{\partial P^*}, \\
e^* &= \frac{1}{\beta_\theta^*}\frac{\partial \beta^*}{\partial \theta^*}, \quad f^* = \frac{1}{\beta_\theta^*}\frac{\partial \beta^*}{\partial P^*}, \quad m^* = \frac{1}{\lambda^*}\frac{\partial \lambda^*}{\partial \theta^*}, \quad n^* = \frac{1}{\lambda^*}\frac{\partial \lambda^*}{\partial P^*}, \\
\beta_\theta^* &= -\frac{1}{\rho^*}\frac{\partial \rho^*}{\partial \theta^*}, \quad \gamma^* = \frac{1}{\rho^*}\frac{\partial \rho^*}{\partial P^*},
\end{aligned} \tag{2.19}$$

are the fluid property coefficients. Leading order approximation of the resulting equations was the tool used by Gray and Giorgini [34] to derived a set of constraints for

the range of validity of OB approximation. These constraints are introduced as

$$\begin{aligned}
&\epsilon_1^* = \beta_{\theta_0}^* \Delta\theta^* \leq \delta^*, \quad \epsilon_2^* = \gamma_0^* \rho_0^* g^* h^* \leq \delta^*, \quad \epsilon_3^* = c_0^* \Delta\theta^* \leq \delta^*, \\
&\epsilon_4^* = d_0^* \rho_0^* g^* h^* \leq \delta^*, \quad \epsilon_5^* = a_0^* \rho_0^* g^* h^* \leq \delta^*, \quad \epsilon_6^* = b_0^* \rho_0^* g^* h^* \leq \delta^*, \\
&\epsilon_7^* = m_0^* \Delta\theta^* \leq \delta^*, \quad \epsilon_8^* = n_0^* \rho_0^* g^* h^* \leq \delta^*, \quad \epsilon_9^* = e_0^* \Delta\theta^* \leq \delta^* \\
&\epsilon_{10}^* = f_0^* \rho_0^* g^* h^* \leq \delta^*, \quad \epsilon_{11}^* = \beta_{\theta_0}^* g^* h^* / c_{p0}^* \leq \delta^*, \quad \epsilon_{12}^* = \epsilon_{11}^* \theta_0^* / \Delta\theta \leq \delta^*,
\end{aligned} \tag{2.20}$$

where $\delta^* = 0.1$ is a small enough number, which leads to a maximum error of 10% in the estimate of the fluid property. In Eq. 2.20, the h^* (channel half height) is substituted as the characteristic size of the problem. Recently, Pons and Quéré [87] propose a further restrictive condition for the validity range of OB approximation, i.e. $\epsilon_{12} < 0.02$, for the work done by pressure forces and the heat generated by viscous losses to be negligible. Altogether, these constraints set the boundaries for an explicit evaluation of the validity ranges of the OB approximation [142]. For air, the most restrictive conditions are ϵ_1^* (variation of ρ^* with θ^*), ϵ_2^* (variation of ρ^* with P^*) and ϵ_{12}^* (pressure work term). For water, the most restrictive conditions are ϵ_9^* (variation of β^* with T^*), ϵ_8^* (variation of λ^* with P^*) and ϵ_{12}^* (pressure work term) [142]. Outside the validity range of OB approximation, more complex Non-Oberbeck-Boussinesq (NOB) models (incompressible NOB or Low-Mach approximation) must be employed.

2.2 Double diffusive convection

2.2.1 Governing equations

We consider the problem of DDC in a horizontal layer bounded by a no-slip bottom wall and a slip top surface that are orthogonal to gravity (pointing downwards) and are separated by a distance $2h^*$. The flow, which is incompressible and Newtonian, is driven by the competition between the stabilizing distribution of temperature and the destabilizing distribution of salinity. We define the temperature and salinity difference cross the fluid layer as $\Delta s^* = s_t^* - s_b^*$ and $\Delta\theta = \theta_t^* - \theta_b^*$, where subscripts t and b refer to the top and bottom boundary, respectively. Naturally, $\Delta s^* > 0$ and $\Delta\theta^* > 0$. Employing the OB approximation, the fluid density can be prescribed as a linear function of s^* and θ^*, and it can be written in the following form:

$$\rho^*(\theta^*, s^*) = \rho_0^* \left[1 - \beta_\theta^* \theta^* + \beta_s^* s^*\right] \tag{2.21}$$

Note that, ρ_0^* is the reference density of the fluid at reference temperature and salinity. β_s^* is the volumetric salinity expansion coefficients. Both temperature and salinity are expressed with respect to their reference values $\theta_0^* = (\theta_b^* + \theta_t^*)/2$ and $s_0^* = (s_b^* + s_{top}^*)/2$. Here, we introduce the governing equations that describe the problem directly in dimensionless form as

$$\frac{\partial u_i}{\partial x_i} = 0 \quad , \tag{2.22}$$

$$\frac{\partial u_i}{\partial t} + u_j \frac{\partial u_i}{\partial x_j} = -\frac{\partial p}{\partial x_i} + \sqrt{\frac{Pr_s}{Ra_s}} \frac{\partial^2 u_i}{\partial {x_j}^2} + \delta_{i,3}(\Lambda\theta - s) + \delta_{1,i} \quad , \tag{2.23}$$

$$\frac{\partial \theta}{\partial t} + u_j \frac{\partial \theta}{\partial x_j} = Le \sqrt{\frac{1}{Pr_s Ra_s}} \frac{\partial^2 \theta}{\partial {x_j}^2} \quad , \tag{2.24}$$

$$\frac{\partial s}{\partial t} + u_j \frac{\partial s}{\partial x_j} = \sqrt{\frac{1}{Pr_s Ra_s}} \frac{\partial^2 s}{\partial {x_j}^2} \quad , \tag{2.25}$$

For adimensionalization of the governing equations, we used the same normalization demonstrated in Eq. 2.9 except for the velocity. Salinity is a new variable in the governing equations of DDC. Therefore, salinity and velocity are made dimensionless as follows:

$$u_i = \frac{u_i^*}{\sqrt{g^* \beta_s^* h^* (\Delta s^*/2)}}, \quad s = \frac{s^* - s_0^*}{\Delta s^*/2}. \tag{2.26}$$

The dimensionless numbers that appear in equations 2.22-2.25 are the Lewis number Le, the density ratio Λ, the salinity Rayleigh number Ra_s and the salinity Prandtl number Pr_s. These are defined as:

$$Ra_s = \frac{g^* \beta_s^* \Delta s^* (2h^*)^3}{\kappa_s^* \nu^*} \quad , \quad Pr_s = \frac{\nu^*}{\kappa_s^*} \quad , \quad Le = \frac{\kappa_\theta^*}{\kappa_s^*} \quad , \quad \Lambda = \frac{\beta_\theta^* \Delta \theta^*}{\beta_s^* \Delta s^*}, \tag{2.27}$$

where κ_θ^* and κ_s^* are the thermal and salt diffusivities, respectively [133]. To keep the consistency of used notation between the governing equations of stably-stratified turbulence and DDC, we rewrite the governing Eqs. 2.22-2.25 using S-terms (containing non-linear convective terms, the dimensionless mean pressure gradient and the buoyancy term) as

$$\frac{\partial u_i}{\partial x_i} = 0 \, , \tag{2.28}$$

$$\frac{\partial u_i}{\partial t} = S_i + \sqrt{\frac{Pr_s}{Ra_s}} \left(\frac{\partial^2 u_i}{\partial {x_j}^2} \right) - \frac{\partial p}{\partial x_i} \, , \tag{2.29}$$

$$\frac{\partial \theta}{\partial t} = S_\theta + Le \sqrt{\frac{1}{Pr_s Ra_s}} \left(\frac{\partial^2 \theta}{\partial {x_j}^2} \right). \tag{2.30}$$

$$\frac{\partial s}{\partial t} = S_s + \sqrt{\frac{1}{Pr_s Ra_s}} \left(\frac{\partial^2 s}{\partial {x_j}^2} \right). \tag{2.31}$$

For the problem of DDC, the S-terms can be written as

$$S_i = -u_j \frac{\partial u_i}{\partial x_j} + \delta_{i,1} + \delta_{i,3}(\Lambda \theta - s), \tag{2.32}$$

$$S_\theta = -u_j \frac{\partial \theta}{\partial x_j} \, , \tag{2.33}$$

$$S_s = -u_j \frac{\partial s}{\partial x_j} \, . \tag{2.34}$$

2.2.2 Convective and diffusive scaling of the shear

In addition to the controlling parameters defined in Eq. 2.27, a further parameter that controls the flow is the imposed shear. In dimensionless form, it is defined as:

$$\Gamma = \frac{u_m^*}{U^*} \quad , \tag{2.35}$$

where u_m^* is the imposed mean velocity at the top boundary and U^* is a suitable reference velocity scale for the DDC process. In convection-diffusion problems, we can define one velocity scale based on convection and one based on diffusion. The most common choice one can find in the literature [132, 133, 134] is to scale all velocities by the free-fall velocity of the convective plumes, defined as $U^* = \sqrt{g^* \beta_s^* h^* (\Delta s^*/2)}$. Following archival literature on buoyancy induced flows, we take the free fall velocity U^* as a reference scale.

An alternative choice, perhaps more related to the physics of the process under investigation here, is to normalize the shear velocity by a diffusive velocity U_d^*, which appears to be the natural velocity scale for the dynamics of salt finger formation in our flow. Note that the renormalization based on diffusive scaling is in principle not appropriate when diffusion is not playing a dominant role, like for example in collective instability waves, intrusions and thermohaline staircases, all cases for which we expect the buoyancy scaling to be more appropriate [90, 133]. To define U_d^*, we first need to set a reference diffusive length scale. In the present problem, we can adopt the definition by Radko [90], which in this case is:

$$d^* = \left(\frac{\kappa_\theta^* \nu^*}{g^* \beta_\theta^* \frac{\partial \langle \theta^* \rangle}{\partial z^*}} \right)^{\frac{1}{4}}, \tag{2.36}$$

where the mean temperature gradient $\partial\langle\theta\rangle/\partial z$ is used instead of the salinity gradient since temperature is the rapidly diffusing scalar. Using the diffusive length scale d^*, we obtain a diffusive velocity $U_d^* = \kappa_\theta^*/d^*$, and therefore a (diffusive) dimensionless shear velocity Γ_d. As it can be seen from Eq. 2.36, the internal scale d^* does not depend on the thickness of the diffusive layer(in this case, channel height $2h^*$). If the thickness of diffusive layer gets much larger compared to the internal scale d^*, the vertical boundaries lose their significance for the mechanisms in the interior of the physical domain. Since we are interested in the response of the system to the shear, we will rescale the applied velocity as a function of the diffusion velocity. The diffusion velocity is defined as $\frac{\kappa_\theta^*}{d^*}$. To express Γ in diffusive scaling, we define diffusion shear velocity rate Γ_d as

$$\Gamma_d = \frac{u_m^* d^*}{\kappa_\theta^*}. \tag{2.37}$$

In the diffusive velocity only the stabilizing scalar is playing a role, whereas the destabilizing scalar is causing the free-fall velocity. In this particular problem, transport parameters are such that the temperature transfer is dominated by diffusion, thus leading the temperature gradient to attain a constant value, which in dimensionless units is $\frac{\partial\langle\theta\rangle}{\partial z} \simeq 1$. Thermal Nusselt number is computed in section 6.3, and it is close

to unity in our problem. Taking Eq. 2.35, Eq. 2.36 and Eq .2.37 and taking the fact into account that the thermal Nusselt number is close to unity, we end up with the following formulation for the ratio between the two shear velocities. Therefore, we obtain:

$$\frac{\Gamma_d}{\Gamma} = \frac{1}{2}\left(\frac{Ra_s {Pr_\theta}^2}{Le\Lambda}\right)^{\frac{1}{4}}. \tag{2.38}$$

3 Methodology

3.1 Numerical approach

Throughout this thesis we will analyze two different physical problems (stably-stratified wall-bounded turbulence and DDC under the effect of shear). The procedure of the numerical solution shares many similarities between these two problems. Therefore, in this chapter, we only represent the numerical scheme for the problem of stably-stratified turbulence. Schematic representation of the numerical algorithm for both problems is shown in Appendix B. In this chapter, the numerical approach developed for the solution of Eqs. 2.10-2.12 is discussed. The general overview of the numerical approach is as follows: The dimensionless system of equations has been spatially-discretized using a pseudo-spectral approach [14, 45, 84] with Fourier discretization in the streamwise (x) and spanwise (y) directions and Chebyshev polynomials in the wall-normal (z) direction. The adoption of Fourier series in the x and y directions implicitly enforces periodic boundary conditions on all variables along these directions. All variables are Eulerian and are solved on the same computational grid. A uniform grid spacing is adopted in the streamwise and spanwise directions (Fourier discretization), while in the wall-normal direction Chebyshev-Gauss-Lobatto points were chosen, thus leading to a much finer grid close to the channel walls. As customarily done in pseudo-spectral methods, convective/non-linear terms are computed in physical space and then transformed to wavenumber space using a dealiasing procedure (2/3 rule).

3.2 Solution Procedure

The present scheme solves for the balance equations of motion Eqs. 2.10-2.12 through the elimination of pressure. The pressure field can be removed upon taking the curl of the Navier-Stokes equation, to give:

$$\frac{\partial \omega_k}{\partial t} = \epsilon_{ijk} \frac{\partial S_j}{\partial x_i} + \frac{1}{Re} \nabla^2 \omega_k, \tag{3.1}$$

where $\omega_k = \epsilon_{ijk} \frac{\partial u_j}{\partial x_i}$ is the $k-th$ component of the vorticity vector. Note that the $S-$terms in Eq. 3.1 have already been introduced in subsection 2.1.3. Taking twice the

curl of Eq. 2.11 and using Eq. 2.10 together with the vectorial identity $\nabla \times (\nabla \times \mathbf{v}) = \nabla(\nabla \cdot \mathbf{v}) - \nabla^2 \mathbf{v}$, a 4^{th}-order equation in u_i can be obtained:

$$\frac{\partial(\nabla^2 u_i)}{\partial t} = \nabla^2 S_i - \frac{\partial}{\partial x_i}\left(\frac{\partial S_j}{\partial x_j}\right) + \frac{1}{Re}\nabla^4 u_i. \tag{3.2}$$

Eqs. 3.1-3.2 can be written with respect to the normal components, *i.e.* for ω_3 and u_3:

$$\frac{\partial \omega_3}{\partial t} = \frac{\partial S_2}{\partial x_1} - \frac{\partial S_1}{\partial x_2} + \frac{1}{Re}\nabla^2 \omega_3. \tag{3.3}$$

$$\frac{\partial(\nabla^2 u_3)}{\partial t} = \nabla^2 S_3 - \frac{\partial}{\partial x_3}\left(\frac{\partial S_j}{\partial x_j}\right) + \frac{1}{Re}\nabla^4 u_3. \tag{3.4}$$

These two equations are numerically solved for ω_3 and u_3. With ω_3 and u_3 known, u_1 and u_2 can be obtained by solving the following equations simultaneously:

$$\frac{\partial u_1}{\partial x_1} + \frac{\partial u_2}{\partial x_2} = -\frac{\partial u_3}{\partial x_3}, \tag{3.5}$$

$$\frac{\partial u_2}{\partial x_1} - \frac{\partial u_1}{\partial x_2} = \omega_3. \tag{3.6}$$

Eqs. 3.5 and 3.6 derive, respectively, from continuity and from the definition of vorticity. Although not needed for time advancement of the solutions, pressure can be obtained by solving a Poisson-type equation after all velocity components have been found:

$$\nabla^2 p = \frac{\partial S_j}{\partial x_j}. \tag{3.7}$$

Once the velocity field is known, the temperature field can be obtained from the solution of the energy balance equation:

$$\frac{\partial T}{\partial t} = S_T + \frac{1}{Re_\tau Pr}\left(\frac{\partial^2 T}{\partial {x_j}^2}\right). \tag{3.8}$$

A schematic representation of the algorithm is shown in Appendix B.

3.3 Spectral Representation of Solutions

To represent the solution in space, finite Fourier expansion in the homogeneous (x_1 and x_2) directions is used:

$$f(x_1, x_2, x_3) = \sum_{|n_1|}^{\frac{N_1}{2}} \sum_{|n_2|}^{\frac{N_2}{2}} \hat{f}(k_1, k_2, x_3) e^{i(k_1 x_1 + k_2 x_2)}, \tag{3.9}$$

where $\hat{f}$ represents the Fourier coefficients of a general dependent function, $i = \sqrt{-1}$, N_1 and N_2 are the number of Fourier modes retained in the series, and the summation

indices n_1 and n_2 are chosen so that $-\frac{N_1}{2}+1 \leq n_1 \leq \frac{N_1}{2}$ and $-\frac{N_2}{2}+1 \leq n_2 \leq \frac{N_2}{2}$. The wavenumbers k_1 and k_2 are given by:

$$k_1 = \frac{2\pi n_1}{L_1} \tag{3.10}$$

$$k_2 = \frac{2\pi n_2}{L_2}, \tag{3.11}$$

with L_1 and L_2 being the periodicity lengths in the streamwise and spanwise directions. Because of the orthogonality of the Fourier functions, the Fourier transform $\hat{f}$ can be obtained as:

$$\hat{f}(k_1, k_2, x_3) = \frac{1}{N_1 N_2} \sum_{|n_1|}^{\frac{N_1}{2}} \sum_{|n_2|}^{\frac{N_2}{2}} f(x_1, x_2, x_3) e^{-i(k_1 x_1 + k_2 x_2)}, \tag{3.12}$$

where x_1 and x_2 are chosen to be the transform locations

$$x_1 = \frac{n_1}{N_1} L_1 \tag{3.13}$$

$$x_2 = \frac{n_2}{N_2} L_2. \tag{3.14}$$

In the cross-stream (wall-normal) direction x_3, Chebyshev polynomials are used to represent the solution,

$$\hat{f}(k_1, k_2, x_3) = \sum_{n_3=0}^{N_3'} a(k_1, k_2, n_3) T_n(x_3), \tag{3.15}$$

where the prime denotes that the first term is halved. The Chebyshev polynomial of order n_3 in x_3 is defined as

$$T_{n_3}(x_3) = \cos(n_3 \arccos(x_3)), \tag{3.16}$$

with $-1 \leq x_3 \leq 1$. Orthogonality also exist for Chebyshev polynomials, which leads to the following inverse transformation:

$$\hat{a}(k_1, k_2, n_3) = \frac{2}{N_3} \sum_{n_3=0}^{N_3'} \hat{a}(k_1, k_2, x_3) T_{n_3}(x_3). \tag{3.17}$$

In physical space the collocation points along the cross-stream direction are related to Chebyshev indexes in the following way:

$$x_3 = \cos\left(\frac{n_3 \pi}{N_3}\right), \tag{3.18}$$

The advantage of using Chebyshev polynomials to represent the solution in the cross-stream direction is that such a representation gives very good resolution in the regions

close to the boundaries, because the collocation points cluster there (in wall bounded flows, resolution close to the wall is very important, since large gradients of the solutions occur there). In Fig. 3.1, a representation of the first six polynomials is given. For in-depth discussion on Chebyshev polynomials and their applications in numerical analysis, see Fox and Parker [24].
Therefore, the spectral representation (in all three directions) of a generic dependent variable takes the final form

$$f(x_1,x_2,x_3)=\sum_{|n_1|}^{\frac{N_1}{2}}\sum_{|n_2|}^{\frac{N_2}{2}}\sum_{n_3=0}^{N_3'}\hat{a}(k_1,k_2,n_3)e^{i(k_1x_1+k_2x_2)}T_{n_3}(x_3), \tag{3.19}$$

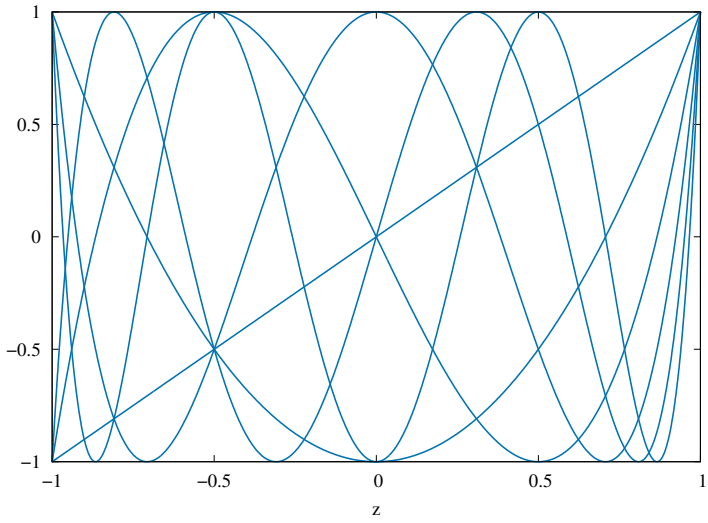

FIGURE 3.1 – The standardized Chebishev polynomials $T_r(x_3)$ (with $r=0,..6$) in computational space for $-1\leq x_3\leq 1$.

3.4 Discretization of the equations

3.4.1 Momentum equations

With the spectral representation given by Eq. 3.9, Eq. 3.4 can be written as

$$\begin{aligned}\frac{\partial}{\partial t}\left(\frac{\partial^2}{\partial x_3^2}-k^2\right)\hat{u}_3=&\left(\frac{\partial^2}{\partial x_3^2}-k^2\right)\hat{S}_3\\&-\frac{\partial}{\partial x_3}\left(ik_1\hat{S}_1+ik_2\hat{S}_2+\frac{\partial}{\partial x_3}\hat{S}_3\right)\\&+\frac{1}{Re}\left(\frac{\partial^2}{\partial x_3^2}-k^2\right)\left(\frac{\partial^2}{\partial x_3^2}-k^2\right)\hat{u}_3,\end{aligned} \tag{3.20}$$

where $k^2 = k_1^2 + k_2^2$. Time-advancement of Eq. 3.20 is performed adopting a IMplicit-EXplicit scheme (IMEX); S-terms are integrated explicitly with an Adams-Bashforth scheme, while the other terms implicitly. A Crank-Nicolson scheme is used to integrate the implicit terms of the second order equation for the wall-normal vorticity and of the fourth order equation for the wall-normal velocity. The implicit part of the two energy and salinity transport equations is integrated with an implicit Euler scheme; this choice reduces the unphysical high frequency oscillations that could arise from the steep gradients of the equations [4, 138]. At the first time step an explicit Euler scheme is used for the explicit part of all the equations. The time-differenced form of Eq. 3.20, based on the above schemes, is

$$\begin{aligned}\left(\frac{\partial^2}{\partial x_3^2} - k^2\right)\frac{(\hat{u}_3^{n+1} - \hat{u}_3^n)}{\Delta t} =& \frac{3}{2}\left(\frac{\partial^2}{\partial x_3^2} - k^2\right)\hat{S}_3^n - \frac{1}{2}\left(\frac{\partial^2}{\partial x_3^2} - k^2\right)\hat{S}_3^{n-1} \\ &- \frac{\partial}{\partial x_3}\, ik_1\left(\frac{3}{2}\hat{S}_1^n - \frac{1}{2}\hat{S}_1^{n-1}\right) \\ &- \frac{\partial}{\partial x_3}\, ik_2\left(\frac{3}{2}\hat{S}_2^n - \frac{1}{2}\hat{S}_2^{n-1}\right) \\ &- \frac{\partial^2}{\partial x_3^2}\left(\frac{3}{2}\hat{S}_3^n - \frac{1}{2}\hat{S}_3^{n-1}\right) \\ &+ \frac{1}{Re}\left(\frac{\partial^2}{\partial x_3^2} - k^2\right)\left(\frac{\partial^2}{\partial x_3^2} - k^2\right)\frac{(\hat{u}_3^{n+1} + \hat{u}_3^n)}{2},\end{aligned} \tag{3.21}$$

where superscripts $n-1$, n and $n+1$ indicate three successive time levels. By defining $\gamma = \frac{\Delta t}{2\,Re}$ we can rearrange Eq. 3.21:

$$\begin{aligned}&\left[1 - \gamma\left(\frac{\partial^2}{\partial x_3^2} - k^2\right)\right]\left(\frac{\partial^2}{\partial x_3^2} - k^2\right)\hat{u}_3^{n+1} = \\ &- k^2\left(\frac{3}{2}\hat{S}_3^n - \frac{1}{2}\hat{S}_3^{n-1}\right)\Delta t \\ &- \frac{\partial}{\partial x_3}\, ik_1\left(\frac{3}{2}\hat{S}_1^n - \frac{1}{2}\hat{S}_1^{n-1}\right)\Delta t \\ &- \frac{\partial}{\partial x_3}\, ik_2\left(\frac{3}{2}\hat{S}_2^n - \frac{1}{2}\hat{S}_2^{n-1}\right)\Delta t \\ &+ \left(\gamma\frac{\partial^2}{\partial x_3^2} + (1 - \gamma k^2)\right)\left(\frac{\partial^2}{\partial x_3^2} - k^2\right)\hat{u}_3^n.\end{aligned} \tag{3.22}$$

Introducing $\beta^2 = \frac{1+\gamma k^2}{\gamma}$ and recalling that $\frac{\partial \hat{u}_3}{\partial x_3} = -ik_1\hat{u}_1 - ik_2\hat{u}_2$ from continuity, we can manipulate the last term on the RHS of Eq. 3.22:

$$
\begin{aligned}
&-\gamma\left(\frac{\partial^2}{\partial x_3^2}-\beta^2\right)\left(\frac{\partial^2}{\partial x_3^2}-k^2\right)\hat{u}_3^{n+1} = \\
&-k^2(\frac{3}{2}\hat{S}_3^n - \frac{1}{2}\hat{S}_3^{n-1})\Delta t - k^2(\gamma\frac{\partial^2}{\partial x_3^2} + (1-\gamma k^2))\hat{u}_3^n \\
&-\frac{\partial}{\partial x_3}\, ik_1(\frac{3}{2}\hat{S}_1^n - \frac{1}{2}\hat{S}_1^{n-1})\Delta t - \frac{\partial}{\partial x_3}\, ik_1(\gamma\frac{\partial^2}{\partial x_3^2} + (1-\gamma k^2))\hat{u}_1^n \\
&-\frac{\partial}{\partial x_3}\, ik_2(\frac{3}{2}\hat{S}_2^n - \frac{1}{2}\hat{S}_2^{n-1})\Delta t - \frac{\partial}{\partial x_3}\, ik_2(\gamma\frac{\partial^2}{\partial x_3^2} + (1-\gamma k^2))\hat{u}_2^n
\end{aligned}
\tag{3.23}
$$

.

By introducing the historical terms:

$$
\begin{aligned}
\hat{H}_1^n &= (\frac{3}{2}\hat{S}_1^n - \frac{1}{2}\hat{S}_1^{n-1})\Delta t + (\gamma\frac{\partial^2}{\partial x_3^2} + (1-\gamma k^2))\hat{u}_1^n, \\
\hat{H}_2^n &= (\frac{3}{2}\hat{S}_2^n - \frac{1}{2}\hat{S}_2^{n-1})\Delta t + (\gamma\frac{\partial^2}{\partial x_3^2} + (1-\gamma k^2))\hat{u}_2^n, \\
\hat{H}_3^n &= (\frac{3}{2}\hat{S}_3^n - \frac{1}{2}\hat{S}_3^{n-1})\Delta t + (\gamma\frac{\partial^2}{\partial x_3^2} + (1-\gamma k^2))\hat{u}_3^n,
\end{aligned}
\tag{3.24}
$$

Eq. 3.23 becomes:

$$
\left(\frac{\partial^2}{\partial x_3^2}-\beta^2\right)\left(\frac{\partial^2}{\partial x_3^2}-k^2\right)\hat{u}_3^{n+1} = \frac{1}{\gamma}(k^2\hat{H}_3^n + \frac{\partial}{\partial x_3}(ik_1\hat{H}_1^n + ik_2\hat{H}_2^n)).
\tag{3.25}
$$

If we put $\hat{H}^n = k^2\hat{H}_3^n + \frac{\partial}{\partial x_3}(ik_1\hat{H}_1^n + ik_2\hat{H}_2^n)$ we come to the final form of the equation:

$$
\left(\frac{\partial^2}{\partial x_3^2}-\beta^2\right)\left(\frac{\partial^2}{\partial x_3^2}-k^2\right)\hat{u}_3^{n+1} = \frac{\hat{H}^n}{\gamma}.
\tag{3.26}
$$

Defining $\hat{\phi} = \left(\frac{\partial^2}{\partial x_3^2}-k^2\right)\hat{u}_3^{n+1}$ the above fourth-order equation becomes a system of two second-order equations:

$$
\left(\frac{\partial^2}{\partial x_3^2}-\beta^2\right)\hat{\phi} = \frac{\hat{H}^n}{\gamma},
\tag{3.27}
$$

$$
\left(\frac{\partial^2}{\partial x_3^2}-k^2\right)\hat{u}_3^{n+1} = \hat{\phi}.
\tag{3.28}
$$

These equations are solved with the following four boundary conditions:

$$
\begin{aligned}
&\hat{u}_3^{n+1}(\pm 1) = 0 \qquad (a) \\
&\frac{\partial \hat{u}_3^{n+1}}{\partial x_3}(\pm 1) = 0 \qquad (b).
\end{aligned}
\tag{3.29}
$$

The lack of real boundary conditions for $\hat{\phi}$ can be circumvented by decomposing it into three parts:

$$\hat{\phi} = \hat{\phi}_1 + \hat{A}\phi_2 + \hat{B}\phi_3, \tag{3.30}$$

where constants $\hat{A}$ and $\hat{B}$ are to be determined. These three individual components of $\hat{\phi}$ satisfy:

$$\begin{aligned}
&\left(\frac{\partial^2}{\partial x_3^2} - \beta^2\right)\hat{\phi}_1 = \frac{\hat{H}^n}{\gamma}, && \hat{\phi}_1(1) = 0, && \hat{\phi}_1(-1) = 0;\\
&\left(\frac{\partial^2}{\partial x_3^2} - \beta^2\right)\phi_2 = 0, && \phi_2(1) = 0, && \phi_2(-1) = 1;\\
&\left(\frac{\partial^2}{\partial x_3^2} - \beta^2\right)\phi_3 = 0, && \phi_3(1) = 1, && \phi_3(-1) = 0.
\end{aligned} \tag{3.31}$$

Likewise $\hat{u}_3^{n+1}$ can be split into:

$$\hat{u}_3 = \hat{u}_{3,1} + \hat{A}u_{3,2} + \hat{B}u_{3,3}. \tag{3.32}$$

Once the solution of Eqs. 3.31 has been carried out, we can solve:

$$\begin{aligned}
&\left(\frac{\partial^2}{\partial x_3^2} - \beta^2\right)\hat{u}_{3,1} = \hat{\phi}_1, && \hat{u}_{3,1}(1) = 0, && \hat{u}_{3,1}(-1) = 0\\
&\left(\frac{\partial^2}{\partial x_3^2} - \beta^2\right)u_{3,2} = \phi_2, && u_{3,2}(1) = 0, && u_{3,2}(-1) = 0\\
&\left(\frac{\partial^2}{\partial x_3^2} - \beta^2\right)u_{3,3} = \phi_3, && u_{3,3}(1) = 1, && u_{3,3}(-1) = 0.
\end{aligned} \tag{3.33}$$

Finally the unknown constants $\hat{A}$ and $\hat{B}$ are determined applying the boundary conditions of Eq. 3.29(b) to $\hat{u}_3^{n+1}$ written in terms of its components:

$$\begin{aligned}
&\frac{\partial \hat{u}_{3,1}}{\partial x_3}(1) + \hat{A}\frac{\partial u_{3,2}}{\partial x_3}(1) + \hat{B}\frac{\partial u_{3,3}}{\partial x_3}(1) = 0,\\
&\frac{\partial \hat{u}_{3,1}}{\partial x_3}(-1) + \hat{A}\frac{\partial u_{3,2}}{\partial x_3}(-1) + \hat{B}\frac{\partial u_{3,3}}{\partial x_3}(-1) = 0.
\end{aligned} \tag{3.34}$$

With $\hat{A}$ and $\hat{B}$ determined, $\hat{u}_3^{n+1}$ is fully known. The above systems of equations are solved using a Chebyshev method so the solutions $\hat{u}_3^{n+1}$ will be represented by Chebyshev coefficients in the wall normal direction x_3. Therefore, the solution $\hat{u}_3^{n+1}$ will be a function of k_1, k_2 and n_3:

$$\hat{u}_3^{n+1} = \hat{u}_3^{n+1}(k_1, k_2, n_3), \tag{3.35}$$

where $0 < n_3 < N_3$, N_3 being the number of coefficients and collocation points in the wall normal direction. Recalling Eq. 3.9, the solution in space will be:

$$u_3^{n+1}(x_1, x_2, x_3) = \sum_{|n_1|}^{\frac{N_1}{2}} \sum_{|n_2|}^{\frac{N_2}{2}} \sum_{n_3=0}^{N_3'} \hat{u}_3^{n+1}(k_1, k_2, n_3) e^{i(k_1 x_1 + k_2 x_2)} T_{n_3}(x_3), \tag{3.36}$$

The other two velocity components will be determined through the normal vorticity component $\hat{\omega}_3$. Following a discretization procedure similar to that of Eq. 3.4, we can write:

$$\left(\frac{\partial^2}{\partial x_3^2} - \beta^2\right)\hat{\omega}_3^{n+1} = -\frac{(ik_1\hat{H}_2^n - ik_2\hat{H}_1^n)}{\gamma}, \tag{3.37}$$

with boundary conditions:

$$\hat{\omega}_3^{n+1} = ik_1\hat{u}_2 - ik_2\hat{u}_1 = 0 \qquad x_3 = \pm 1. \tag{3.38}$$

Once vorticity is known, $\hat{u}_1^{n+1}$ and $\hat{u}_2^{n+1}$ can be determined from solving:

$$-ik_2\hat{u}_1^{n+1} + ik_1\hat{u}_2^{n+1} = \hat{\omega}_3^{n+1}, \tag{3.39}$$

$$ik_1\hat{u}_1^{n+1} + ik_2\hat{u}_2^{n+1} = -\frac{\partial\hat{u}_3^{n+1}}{\partial x_3}, \tag{3.40}$$

that come from the definition of $\hat{\omega}_3$ and from continuity equation, respectively. Pressure can be calculated by the transformed Poisson equation Eq. 3.7:

$$\left(\frac{\partial^2}{\partial x_3^2} - \beta^2\right)\hat{p}^{n+1} = ik_1\hat{S}_1^{n+1} + ik_2\hat{S}_2^{n+1} + \frac{\partial\hat{S}_3^{n+1}}{\partial x_3}. \tag{3.41}$$

Boundary conditions for $\hat{p}^{n+1}$ can be obtained by the transformed form of Eq. 2.7 in the x_3 direction applied at $x_3 = \pm 1$.
The above scheme is used to evaluate the solutions in the Fourier-Chebyshev space for $k^2 \neq 0$. The case $k^2 = 0$ corresponds to the solution averaged over an $x_1 - x_2$ plane. In this case the solution procedure is simpler: upon time discretization the x_1 and x_2 components of Eq. 2.11 in the Fourier-Chebyshev space after time discretization give:

$$\left(\frac{\partial^2}{\partial x_3^2} - \frac{1}{\gamma}\right)\hat{u}_1^{n+1} = -\frac{\hat{H}_1}{\gamma}, \tag{3.42}$$

$$\left(\frac{\partial^2}{\partial x_3^2} - \frac{1}{\gamma}\right)\hat{u}_2^{n+1} = -\frac{\hat{H}_2}{\gamma}, \tag{3.43}$$

that can be solved by applying the following boundary conditions:

$$\hat{u}_1^{n+1} = \hat{u}_2^{n+1} = 0 \qquad x_3 \pm 1. \tag{3.44}$$

Using the continuity equation, Eq. 3.40, with $k_1 = k_2 = 0$ and the condition $\hat{u}_3^{n+1}(\pm 1) = 0$ one can show that $\hat{u}_3^{n+1} = 0$. To calculate $\hat{p}^{n+1}$ it is necessary to recall the transformed momentum equation, Eq. 2.11, in the x_3 direction for $k^2 = 0$ and $\hat{u}_3^{n+1} = 0$: we have $\hat{p}^{n+1} = -\widehat{(u_3^{n+1}u_3^{n+1})}$.

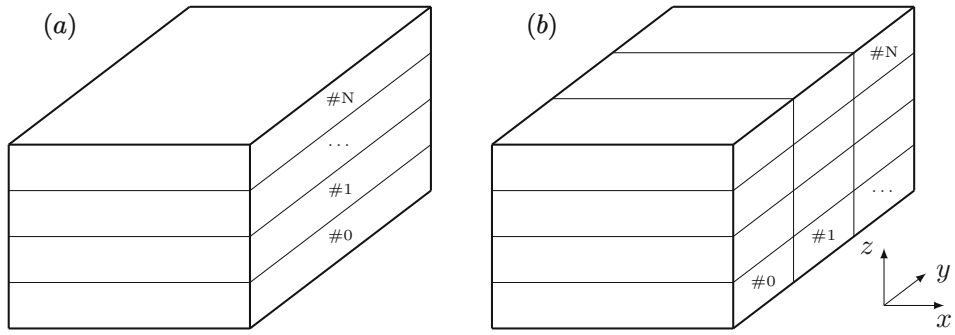

FIGURE 3.2 – Slab, panel (a), and pencil, panel (b), decomposition of the computational domain in physical space. The numbering of the tasks, #0, #1, ..., #N, is reported for reference.

3.4.2 Energy equation

Once the velocity field is given, then the thermal field can be computed solving Eq. 2.12. The convective term S_θ is advanced in the time integration by the second order explicit Adams-Bashfort scheme, while the implicit Crank-Nicolson method is used to advance the diffusion term. The time differenced energy equation Eq. 2.12 is therefore given by:

$$\frac{\hat{\theta}_i^{n+1}-\hat{\theta}_i^n}{\Delta T}=\frac{3}{2}\hat{S}_\theta^n-\frac{1}{2}\hat{S}_\theta^{n-1}+\frac{1}{PrRe_\tau}\frac{\partial^2}{\partial x_j\partial x_j}\left(\frac{\theta_i^{n+1}+\theta_i^n}{2}\right) \tag{3.45}$$

All n and $n-1$ terms are grouped into the historical term

$$\hat{H}_\theta=\left[\gamma_\theta\frac{\partial^2}{\partial z^2}+(1-\gamma_\theta k^2)\right]\hat{\theta}^n+\Delta T\left(\frac{3}{2}\hat{S}_\theta^n-\frac{1}{2}\hat{S}_\theta^{n-1}\right), \tag{3.46}$$

where $k^2=k_1^2+k_2^2$, $\gamma_\theta=\frac{\Delta t}{2Pr\cdot Re_\tau}$. Upon rearrangement the following differential equation for the temperature field can be obtained:

$$\left(\frac{\partial^2}{\partial z^2}-\frac{1+\gamma_T^2}{\gamma_T}\right)\hat{\theta}=-\frac{\hat{H}_\theta}{\gamma_\theta}, \tag{3.47}$$

as an unknown for each Fourier wave number pair (k_1,k_2). Eq. 3.47 can be solved with a Chebishev-Tau method to obtain the new temperature field.

3.5 Code implementation

The presented numerical method has been implemented in a parallel Fortran code. A pure-MPI (Message Passing Interface) approach is adopted to divide the workload among independent MPI tasks; the computational domain is evenly distributed among all the tasks. The main idea lying behind the MPI approach is the division of the workload among several different tasks that work independently one from each other (exception made for the communications among tasks); each tasks has its own

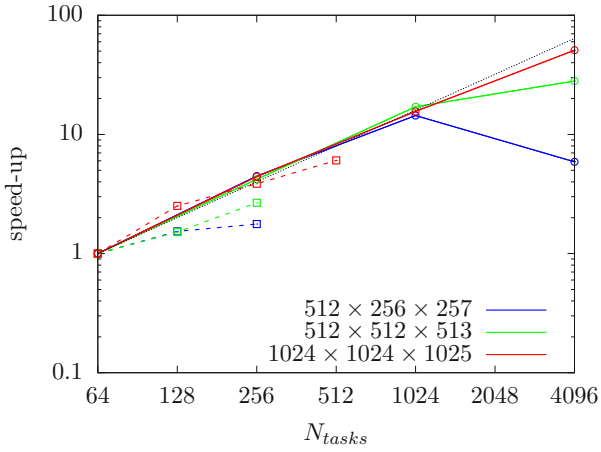

FIGURE 3.3 – Comparison between slab (dashed lines with square markers) and pencil (solid line with circle markers) decomposition for different grid sizes. The speed-up with respect to a reference case on 64 tasks is shown; the ideal scaling is reported with a thin black dotted line. The pencil decomposition achieves better performances than the slab decomposition even at low numbers of tasks. The loss of performances for increasing number of tasks can be appreciated for the coarser grid, $N_x \times N_y \times N_z = 512 \times 256 \times 257$. Performance results were obtained on the Broadwell (BDW) partition of the HPC system Marconi hosted at CINECA (Bologna, Italy).

private variable space, which is not directly accessible to other tasks. With the current implementation, the domain is split using a 2D decomposition (pencil decomposition): the computational domain is partitioned along two out of three dimensions (pencil-like subdomains). This partitioning constitutes an improvement with respect to the 1D decomposition (slab decomposition), in which the computational domain is partitioned along only one direction out of three; a graphical visualization of these domain partitioning approaches is reported in Fig. 3.2. While on one hand the pencil decomposition increases the volume of data communication among the tasks and slightly increases the replication of data across the variable space of different tasks (parameters, constants, ...), on the other hand it greatly increases the maximum number of tasks that can be used to divide the workload. The maximum number of tasks is limited by the number of grid points: for a grid with $\mathcal{O}(N^3)$ points, the maximum number of tasks for the slab decomposition is $\mathcal{O}(N)$, while for the pencil decomposition is $\mathcal{O}(N^2)$. This limitation occurs as the minimum size of a slab is $N \times N \times 1$, while for a pencil it is $N \times 1 \times 1$: each subdomain must include at least one grid point in each direction. The pencil decomposition thus overcomes the limitation of the maximum number of tasks that could be employed; in addition it also shows better performances even at low numbers of tasks, Fig. 3.3. A loss of performances for increasing number of MPI tasks can be observed in Fig. 3.3 for the coarse and intermediate grids: in these cases the number of grid points held by each task becomes too low ($\mathcal{O}(8k)$ points per task for the coarse grid and $\mathcal{O}(33k)$ for the intermediate one). As the number of grid points per task is too low, the time spent in communications among tasks overcomes the time spent in actual calculations, reducing the overall performances of the code.

The distribution of the computational domain is defined with two parameters, $N_{y,CPU}$

TABLE 3.1 – Characteristics of the HPC machines on which performance benchmarks were run

Machine	HPC centre	Node layout	Frequency [GHz]
Marconi BDW	CINECA (IT)	2×18 cores Intel Xeon	2.3
Marconi KNL	CINECA (IT)	1×68 cores Intel Xeon Phi	1.4
Vesta	ANL (USA)	1×16 cores IBM BG/Q	1.6
VSC-3	VSC (AT)	2×8 cores Intel Xeon	2.6

and $N_{z,CPU}$; these parameters determine the partitioning of the domain along the y and z directions. In physical space each task holds all the points in the x direction and a fraction of the points in the y and z directions. This way a Fourier transform can be readily taken in the x direction: to compute a Fourier or Chebyshev transform all points in the transform direction are needed. Once the Fourier transform in the x direction has been taken, the pencils are transposed: data are communicated through MPI communications among the various tasks, so that each task holds all the points in the y direction and only a fraction in the remaining directions. Then, Fourier transforms in the y direction are taken. Again, the pencils are transposed so that each task holds all the points in the z direction and then Chebyshev transforms are taken. In modal space the computational domain is divided along the x and y directions (each task holds all the points in the wall-normal direction). The transform from physical to modal space thus requires: (*i*) one-dimensional Fourier transforms (x direction), (*ii*) pencil transposition, (*iii*) one-dimensional Fourier transforms (y direction), (*iv*) pencil transposition and (*v*) one-dimensional Chebyshev transforms (z direction). The transform from modal to physical space follows the same path backwards. This process is thus constituted of intensive computation phases (Fourier and Chebyshev transforms) interleaved with MPI communications among the various tasks. A MPI Cartesian communicator is adopted to easily define the communication pattern. Fast Fourier and Chebyshev transforms are taken using the functions provided in the library *FFTW* (version 3.3.8) by Frigo and Johnson [25]. This domain partitioning choice gives the best performances: MPI communications occur only during transforms from physical to modal space (and backwards) and, in modal space, each task solves a series of Helmholtz problems (all Helmholtz problems are independent one from each other). Most of the transforms occur during the calculation of non-linear terms: to avoid the costly calculation of convolution integrals, products of variables are computed in physical space, then the result is transformed in modal space (pseudo-spectral method).

Finally, parallel input/output instructions (MPI I/O library) are adopted when reading/writing large data files; this choice improves the overall performances of the code and allows to distribute the workload among high number of tasks with a limited amount of replicated data (low usage of memory for each task).

The performances of the code were measured on several High Performance Computing (HPC) machines: Marconi BDW, Marconi KNL, Vesta and VSC-3. Details on these machines are reported in Tab. 3.1. Performance data will be reported for the Broadwell (BDW) and Knights Landing (KNL) partitions of Marconi and for Vesta; VSC-3 (Ivy Bridge) has similar performances to Marconi Broadwell, thus has not be reported. The strong scaling benchmark for the various HPC machines is reported in Fig. 3.4. In this

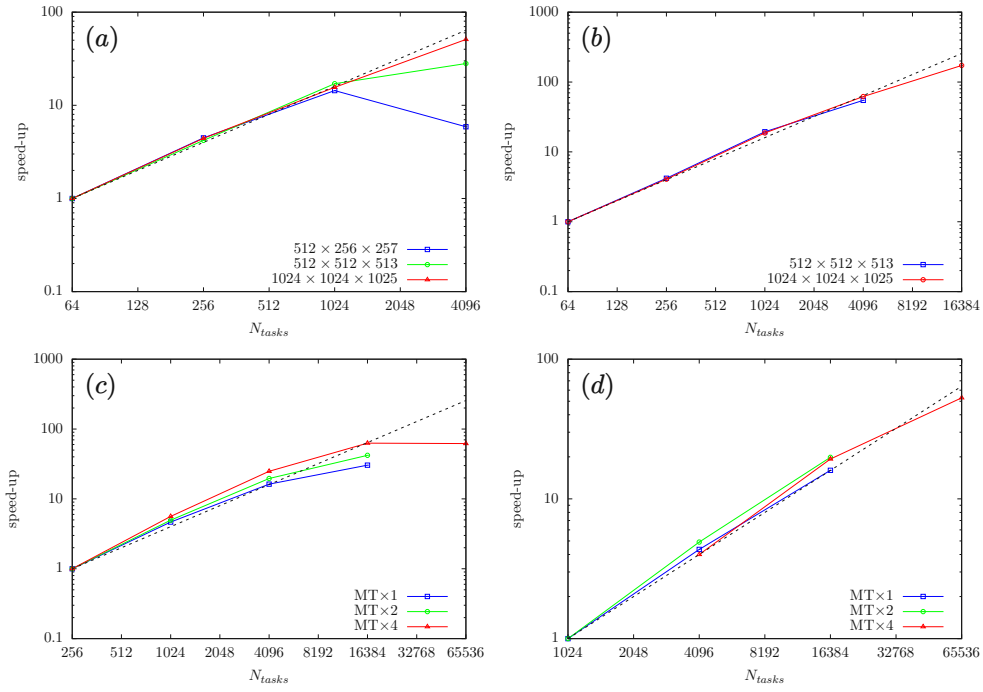

FIGURE 3.4 – Strong scaling for different grid sizes on the various architectures: Marconi BDW, panel (a), Marconi KNL, panel (b), Vesta (grid $512 \times 512 \times 513$ in panel (c) and $1024 \times 1024 \times 1025$ in panel (d)) for different Multi Threading (MT) configurations. A thin black dashed line shows the ideal linear scaling.

benchmark the problem size is kept constant (fixed grid size), while the total number of MPI tasks, N_{tasks}, is increased, thus reducing the load of each task (lower problem size per node). The strong scaling benchmark measures the speed-up with respect to a reference case; here the reference case has been selected as the lower number of tasks that could be run using all physical cores on all the requested nodes. On Marconi BDW and KNL the available RAM per node is higher ($\mathcal{O}(100)$ GB), thus the problem could fit on the memory of two nodes on the BDW partition and one node on the KNL partition. On the other hand, as on Vesta the available RAM per node is 16 GB, the smaller problem size required a minimum of 4 nodes, while the larger problem size required a minimum of 32 nodes. Ideally, the speed-up should grow linearly with the number of tasks employed (thin black dashed line in Fig. 3.4). This benchmark is the most relevant for the cases that will be presented in the following: the total problem size is kept fixed (between $512 \times 256 \times 257$ and $1024 \times 1024 \times 1025$ grid points) and the strong scaling performances of the code are exploited by selecting a total number of tasks that guarantees a reasonable time-to-solution while keeping a high efficiency (speed-up close to the ideal one). As the total number of tasks is increased the parallel overhead also increases: the time spent by the code in communications and synchronizations increases with respect to the time spent in actual computations. This effect is clear for the lower grid sizes (up to $512 \times 512 \times 513$ grid points): as the total

number of MPI tasks is increased, the speed-up strongly reduces and departs from the ideal speed-up. The number of points per task becomes too low for increasing total number of tasks, thus the time spent in calculations reduces, while the communication and synchronization time increases. On the larger problem size ($1024 \times 1024 \times 1025$ grid points) the computational load of each task is high enough to mask the time spent in communications and synchronizations calls, thus this case shows an optimal strong scaling for all the numbers of tasks tested. Considering the problem size adopted for the three-dimensional simulations that will be presented in the following, usually about 1024 MPI tasks are employed, so that a strong scaling close to the ideal is always achieved.

Finally, Multi Threading (MT) was also included in the strong scaling benchmarks performed on Vesta (IBM BG/Q architecture). This machine is characterized by 16 physical cores per node; each of these physical cores can spawn up to four virtual cores (threads). A different MPI task can then be assigned to each thread. In total, three Multi Threading configurations were tested: 1, 2 and 4 threads per core (MT×1, MT×2 and MT×4). Multi Threading is an attractive option, as it allows to increase the total number of tasks while keeping the same usage of computational resources: most HPC systems bill for the amount of time a physical core (or node) is requested, without considering the effective number of tasks actually used. Thus, for the same amount of physical computational resources, up to four times virtual computational resources are available with Multi Threading. However, Multi Threading may not always be convenient: the same CPU-level physical resources (for instance registers and L1 and L2 cache levels) are shared among the various threads. Depending on the specifics of the machine it may or may not be advantageous and thus it should be checked beforehand.

4

Interaction between stable stratification and turbulence

Reproduced in part from:

F. Zonta, P. Hadi Sichani and A. Soldati, *Interaction between thermal stratification and turbulence in channel flow*, J. Fluid Mech., under revision.

To investigate the interaction between stable stratification and turbulence, we consider a stably stratified turbulent flow inside an horizontal channel bounded by two solid walls described in subsection 2.1.3. We run a series of DNSs to solve conservation of mass, momentum and energy under the Oberbeck-Boussinesq (OB) approximation (Eqs. 2.10-2.12). Periodicity along x and y is assumed for both velocity and temperature, while no-slip velocity and imposed-temperature conditions are assumed at the two walls. Present simulations are run at fixed Reynolds and Prandtl number ($Re_\tau = 1000$ and $Pr = 0.71$) but at different values of the Richardson number $Ri_\tau = 50, 100, 200, 300$. A reference simulation at $Ri_\tau = 0$ (neutrally-buoyant) is also performed. From a physical point of view, the simulation set up can represent the flow of air inside a channel of height $2h^* \sim 1.5\ m$ at a reference bulk Reynolds number $Re_b = \rho^* u_b^* h^*/\mu^* = 2 \times 10^4$ and subject to a wall-to-wall temperature difference up to $\approx 10K$. The computational domain has size $L_x^* \times L_y^* \times L_z^* = 4\pi h^* \times 2\pi h^* \times 2h^*$ and is discretized using $1024 \times 1024 \times 1025$ nodes in the streamwise, spanwise and wall-normal direction, respectively. A comprehensive overview of the most important parameters of the simulations is provided in Table 4.1. Note that the size of the computational domain and the spatial resolution, reported in Table 4.1, has been chosen to fulfill the requirements imposed by the DNS. In particular, we explicitly compare the employed grid resolution with the minimum value of the Kolmogorov length scale (occurring at the wall) – computed as $\eta_k^* = \left({\nu^*}^3/\epsilon_k^*\right)^{1/4}$, with ϵ_k^* the turbulent kinetic energy dissipation – with the grid spacing. Also listed in Table 4.1 is the value of the key response parameters in stratified turbulence, the Nusselt number $Nu = 2q_w^* h^*/(\lambda^* \Delta\theta^*)$, with q_w^* the heat flux at the wall. A thorough discussion on the behavior of Nu, and of other important macroscopic parameters, will be given in Sec. 4.4.

TABLE 4.1 – Stably-stratified channel turbulence at $Re_\tau = 1000$ and $Pr = 0.71$: summary of the simulation parameters. For all simulations, the size of the computational domain is $4\pi h^* \times 2\pi h^* \times 2h^*$ along x, y and z, respectively. The grid resolution, Δx, Δy and Δz, is expressed in wall units. While the grid resolution is constant along x and y, it does change in the wall normal direction from a minimum value close to the wall (Δz_w) to a maximum value at the channel center (Δz_c). The value of the Kolmogorov scale at the wall, $\eta_{k,w}$ (expressed in wall units), is also given.

Simulation	Ri_τ	Re_b	Nu_c	Grid points	Δx	Δy	$\Delta z_w - \Delta z_c$	$\eta_{k,w}$
$S0$	0	19960	28.15	$1024 \times 1024 \times 1025$	12.2	6.1	$0.004 - 3.1$	1.4
$S50$	50	22690	9.11	$1024 \times 1024 \times 1025$	12.2	6.1	$0.004 - 3.1$	1.4
$S100$	100	24050	6.79	$1024 \times 1024 \times 1025$	12.2	6.1	$0.004 - 3.1$	1.4
$S200$	200	26320	5.24	$1024 \times 1024 \times 1025$	12.2	6.1	$0.004 - 3.1$	1.4
$S300$	300	28300	4.66	$1024 \times 1024 \times 1025$	12.2	6.1	$0.004 - 3.1$	1.4

4.1 Qualitative behavior of the flow structure

We look first at the qualitative structure of the flow, focusing in particular on the instantaneous temperature distribution θ on a $(y-z)$ cross-section of the channel located at $x = L_x/2$. Results, which are shown in Fig. 4.1 for $Ri_\tau = 0$ (Panel a, neutrally-buoyant case) and for $Ri_\tau = 300$ (Panel b, stably stratified case), will be conveniently discussed by keeping the neutrally-buoyant case ($Ri_\tau = 0$, Fig. 4.1a) as reference. For $Ri_\tau = 0$, temperature is a passive scalar and, as such, it is purely transported by velocity. Vortical structures rising from the boundaries are therefore free to travel over long distances, since they are only bounded by the physical constraint imposed by the walls. Under the action of these vortical structures, a fluid particle with a given temperature is brought to a region with a different temperature, where it thermalizes by diffusion (see Fig. 4.1a). This naturally gives a high degree of mixing. For $Ri_\tau = 300$, the situation is different. While vortical structures are still dominating the near-wall region, their influence away from the boundary appears limited. The reason is that vortical structures are in this case subject to an additional vertical (i.e. in the wall-normal direction) constraint imposed by gravity, which reduces their range of influence to approximately half of the channel height (this is rather clear upon comparison of Fig. 4.1a and Fig. 4.1b). As a consequence, the channel results divided into a top, hot part, and a bottom, cold part (Fig. 4.1b). These two parts behave almost independently each other, and are separated by Internal Gravity Waves (IGW, streaky structure developing at the channel center). The physics of IGWs is simple: because of the background density profile – with density decreasing with height – a fluid particle that is displaced in the wall-normal direction by velocity fluctuations is subject to a restoring buoyancy force that tends to bring it back to its initial position. The fluid particle trespasses its initial equilibrium position and overshoots inertially, giving rise to an oscillation that constitutes the essence of IGWs. We anticipate here, but it will become clear by looking at the fluid statistics (Sec. 4.2), that IGWs appear inside a thermocline – i.e. a region where temperature changes much more than it does above and below it, hence representing a sort of thick interface that hinders the wall-normal transfer of momentum and heat. Due to their importance in the dynamics of stably-stratified flows, IGWs have been analyzed in detail in a number of previous studies (for a comprehensive review on the topic, see [111]).

To appreciate further the different flow structure induced by the stable stratification, we turn now our attention to the distribution of temperature θ and axial velocity u_x on a longitudinal $x-z$ plane located at $y = L_y/2$. Results are shown in Fig. 4.2: panel a and panel b refer to $Ri_\tau = 0$ (temperature and axial velocity, respectively), while panel c and panel d refer to $Ri_\tau = 300$ (temperature and axial velocity, respectively). The flow moves from left to right. As expected, for $Ri_\tau = 0$, temperature (Fig. 4.2a) – which is a passive scalar – is efficiently mixed throughout the entire height of the channel by the dominant vortical structures. The flow (Fig. 4.2b) appears organized into taller vortices which are emitted from the wall and contain ensembles of smaller scale vortices. The wall-normal extension of these taller vortices scales with the channel height $\sim 2h^*$. For $Ri_\tau = 300$, on the other hand, the situation is controlled by the presence of IGWs, which – as clearly visible in both the temperature and velocity maps – dominate the central region of the channel. The presence of these structures

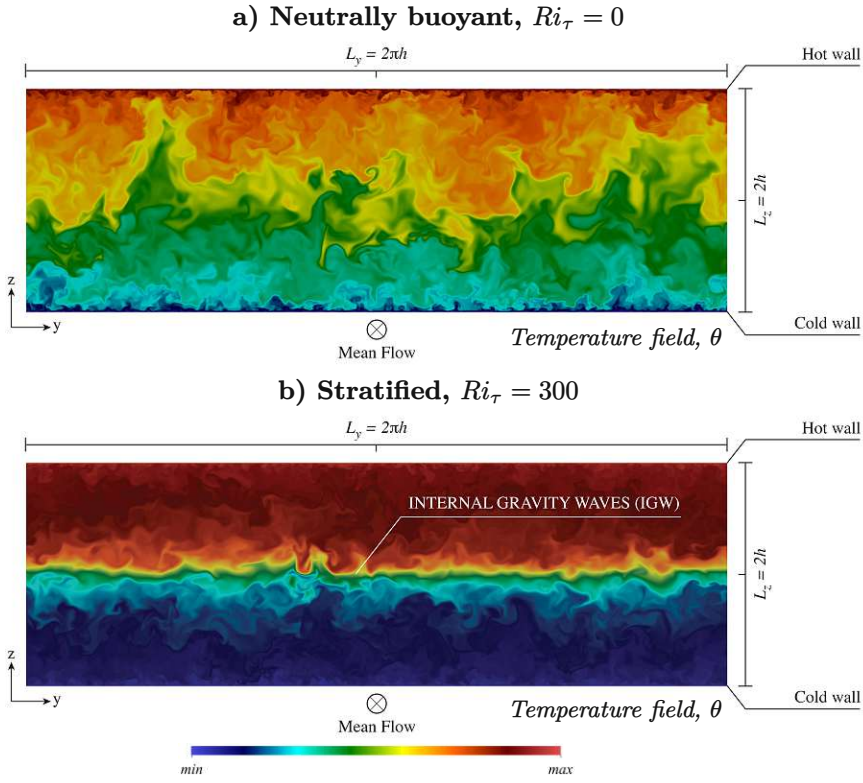

FIGURE 4.1 – Contour maps of temperature, θ, on a $(y-z)$ cross section located at $x = L_x/2$. Panel a) refers to the neutrally-buoyant case, $Ri_\tau = 0$. Panel b) refers to the stably-stratified case at $Ri_\tau = 300$.

naturally modifies the entire dynamics of the flow, inducing an extra confinement to the wall-normal development of vortices, and reducing at the same time their capability of effectively mixing the flow. As a side observation, we note that the temperature field in the proximity of the channel center appears stretched and tilted at an angle with respect to the horizontal direction. This is due to the presence of a strong horizontal shear in that region.

4.2 Velocity and temperature statistics

We now characterize the flow from a statistical viewpoint. Unless differently stated, all results will be presented in wall units, obtained by normalizing velocities by u_τ^*, lengths by $l_\tau^* = \nu^*/u_\tau^*$, times by $t_\tau^* = \nu^*/u_\tau^{*2}$ and temperatures by $\theta_\tau^* = q_w^*/u_\tau^*$. In Fig. 4.3 we show the behavior of the mean streamwise velocity $\langle u_x \rangle$ as a function of the wall-normal coordinate, in linear (Fig. 4.3a) and semilog (Fig 4.3b) scale. Brackets indicate time and space average over the homogeneous directions. Results are rendered according to the following color code: blue (up-triangle) refers to the

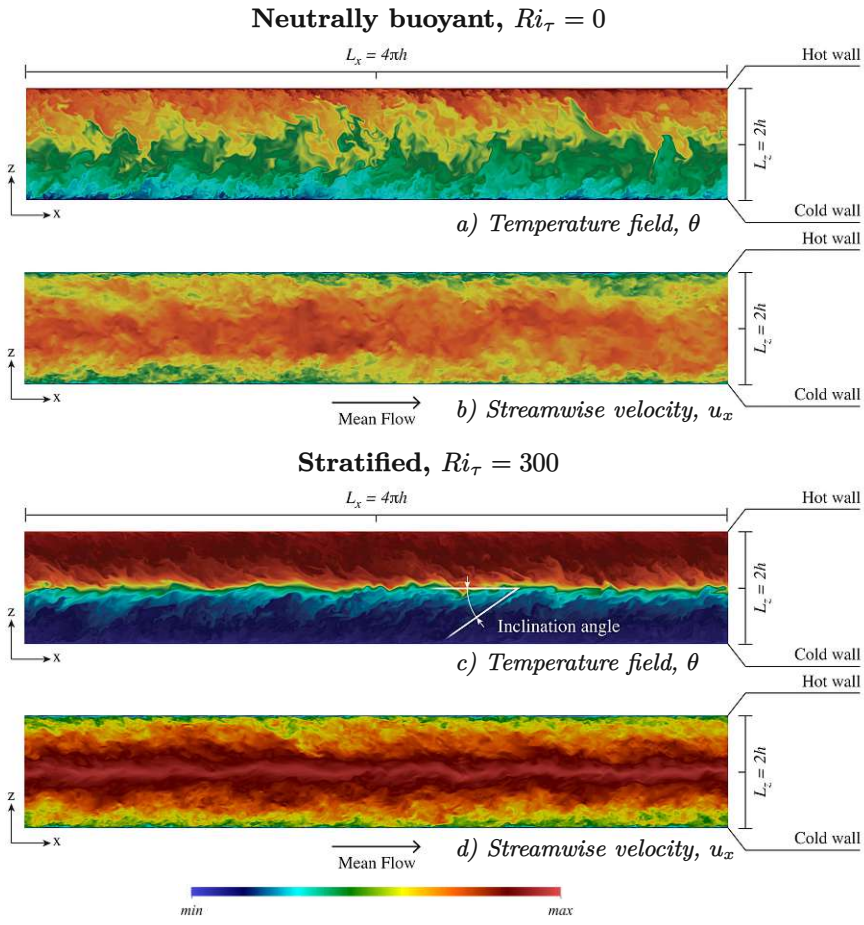

FIGURE 4.2 – Contour maps of temperature θ (panels a and c) and streamwise velocity u_x (panels b and d) on a $(x - z)$ longitudinal section located at $y = L_y/2$. Panel a) and b) refer to the neutrally-buoyant case, $Ri_\tau = 0$. Panel c) and d) refer to the stably-stratified case at $Ri_\tau = 300$. The temperature tilting induced by the horizontal shear at the channel center is also explicitly indicated (panel c).

neutrally-buoyant case ($Ri_\tau = 0$), yellow (down-triangle) refers to $Ri_\tau = 50$, green (square) refers to $Ri_\tau = 100$, purple (diamond) refers to $Ri_\tau = 200$ and red (circle) refers to $Ri_\tau = 300$. The law of the wall, $\langle u_x \rangle = z^+$, and $\langle u_x \rangle = (1/\kappa)\log(z^+) + 5.5$, with κ the Von Kármán constant, is also shown in Fig. 4.3b by a solid line. As expected (see in particular Fig. 4.3b), in the neutrally-buoyant case the mean velocity closely follows the law of the wall – since temperature is a passive scalar that does not influence the velocity field –. In the stably stratified cases, we observe an increase of the mean axial velocity, which is particularly pronounced in the core part of the channel (see both Fig. 4.3a-b), as the shape of the velocity profile deviates significantly from the classical logarithmic behavior and approaches a nearly-laminar, parabolic shape

[28]. This tendency towards a laminarization in the core part of channel is due to the conversion of turbulent kinetic into potential energy, which occurs when a fluid particle moves in the wall-normal direction within the flow. Note also that, since the mean pressure gradient is kept constant among the different simulations, the mean wall stress remains constant, and so does the slope of the velocity at the wall, with all profiles collapsing onto that of the neutrally-buoyant case ($z < 0.1$).

As shown in Fig. 4.4, stratification modifies the behavior of the mean temperature field $\langle\theta\rangle$, which takes a layered structure formed by a near-wall layer ($0 < z < 0.1$), a transition layer ($0.1 < z < 0.8$) and a core layer ($0.8 < z < 1$). Note that temperature in Fig. 4.4a is shown in outer units, i.e. not rescaled in wall units (for an overview of the scaling system, see Appendix A). Compared to the neutrally buoyant case, stratification reduces the mean temperature gradient in the near-wall layer (i.e. it reduces the Nusselt number), while at the same time increasing it in the core layer. This latter observation is of particular importance, since it indicates the tendency for turbulent stratified channel flows to develop a kind of thick interface – the thermocline – inside which the temperature changes more vigorously than it does immediately above and below. The thermocline, which forms right where the mean shear vanishes, constitutes a barrier for wall-normal momentum and heat transport. Reportedly [144, 142, 28, 23], there is a strong connection between the presence of a thermocline, and the presence of IGWs – which, as discussed in Sec. 4.1, occur at the channel center –, in the sense that IGWs develop where a thermocline exists. Interestingly, the temperature gradient in the core region of the channel does not increase monotonically for increasing Ri_τ: it first increases (going from $Ri_\tau = 0$ to $Ri_\tau = 100$), and then reduces (going from $Ri_\tau = 100$ to $Ri_\tau = 300$). We anticipate here, but we will come back to it later, that this non-monotonic trend of the temperature profile at the channel center can be explained by looking at the intertwined behavior of the turbulent (or buoyancy) and diffusive fluxes. In the transition layer, between the near-wall and the core layer, the temperature gradient remains small, as the flow is characterized by an higher degree of mixing. Not surprisingly, when rescaled in wall units, i.e. by keeping the friction temperature $\theta^*_\tau = q^*_w/u^*_\tau$ as reference, the mean temperature profile $\Theta = (\theta^* - \theta^*_w)/\theta^*_\tau$ recovers a monotonic behavior (Fig. 4.4b). This is particularly visible in the inset of Fig. 4.4b, where a close-up view of the mean temperature profile in the core region of the channel is given. Note also that, for the neutrally buoyant case, and similarly to what happens for the streamwise velocity $\langle u_x\rangle$, the behavior of Θ can be parameterized by $\Theta = Pr \cdot z^+$ (boundary layer) and $\Theta = 2.2\log(z^+) + 3.3$ (core region).

To evaluate the influence of stratification on turbulence, we now look at the root mean square of the streamwise $\langle u'_{x,rms}\rangle$, spanwise $\langle u'_{y,rms}\rangle$ and wall-normal $\langle u'_{z,rms}\rangle$ velocity fluctuations, and at the root mean square of temperature fluctuations $\langle\Theta'_{rms}\rangle$. Results, which are presented in Fig. 4.5, clearly show that all velocity and temperature fluctuations are essentially unaffected by stratification in the near-wall region ($z < 0.1$), where they recover the behavior of canonical near-wall turbulence. Farther from the wall, in the region $0.3 < z < 0.8$, $\langle u'_{x,rms}\rangle$ decreases first and increases later compared to the neutrally buoyant case, while the opposite behavior – increasing first and decreasing later – is observed for $\langle u'_{z,rms}\rangle$. Note that the crossover between the profiles of stratified and neutrally-buoyant turbulence occurs around $z \simeq 0.5$, and is somehow influenced by Ri_τ. By contrast, $\langle u'_{y,rms}\rangle$ is characterized by a clear

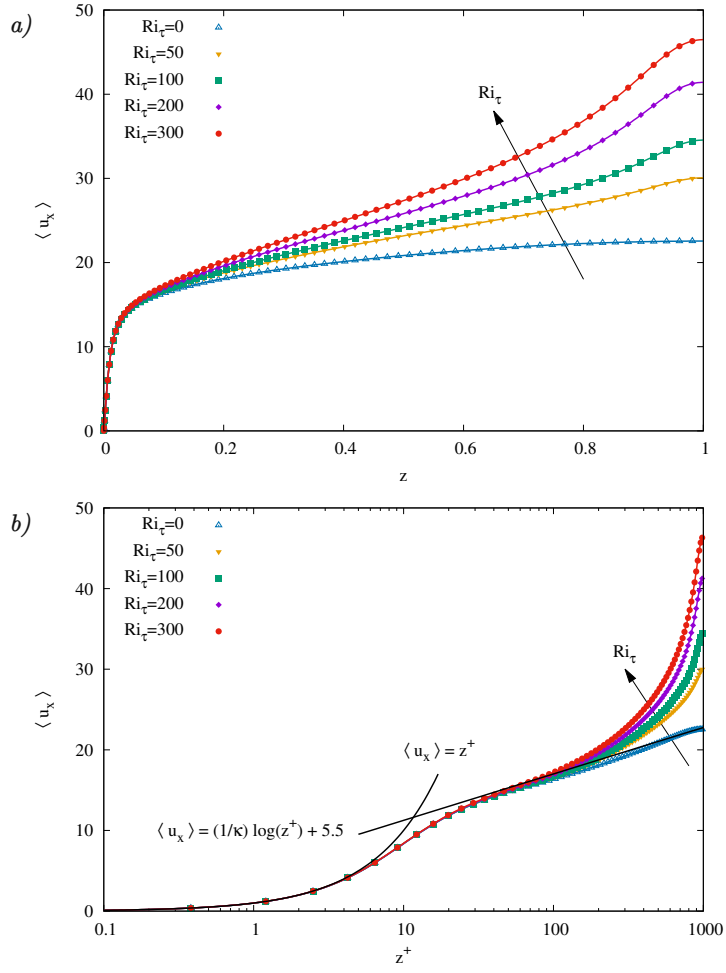

FIGURE 4.3 – Mean fluid streamwise velocity $\langle u_x \rangle$ as a function of the wall-normal direction, z, in linear (panel a) and semiology scale (panel b) for the different cases considered in the present study. Comparison between the reference case of unstratified turbulence ($Ri_\tau = 0$), and the stratified turbulence at $Ri_\tau = 50$, $Ri_\tau = 100$, $Ri_\tau = 200$ and $Ri_\tau = 300$ (filled symbols). The classical law of the wall $\langle u_x \rangle = z^+$ and $\langle u_x \rangle = (1/\kappa)\log(z^+) + 5.5$, with κ the Von Kármán constant, is also shown for comparison in panel b (solid line).

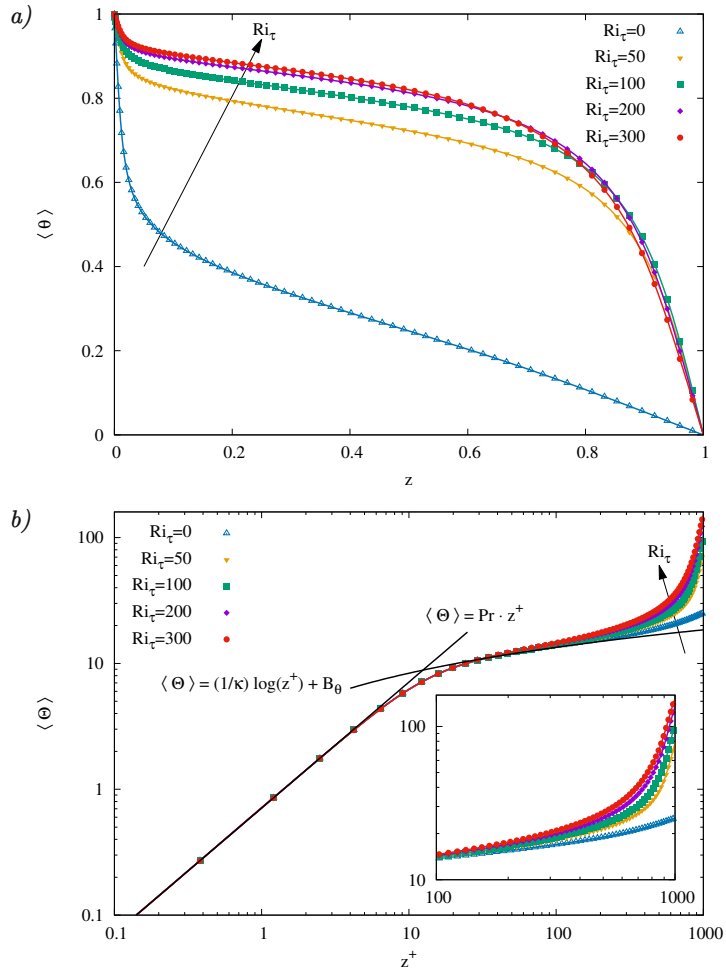

FIGURE 4.4 – Mean fluid temperature $\langle\theta\rangle$ in linear (panel a) and log (panel b) scale as a function of the wall-normal distance expressed in wall units, z^+. Comparison between the reference case of unstratified turbulence ($Ri_\tau = 0$), and the stratified turbulence at $Ri_\tau = 50$, $Ri_\tau = 100$, $Ri_\tau = 200$ and $Ri_\tau = 300$ (filled symbols). A proposed correlation $\langle\Theta\rangle = Pr{\cdot}z^+$ and $\langle\Theta\rangle = (1/\kappa)\log(z^+)+B_\theta$, with $\kappa_\theta = 4.54$ and $B_\theta = 3.3$, is also shown for comparison (solid line, panel b). A close-up view of the mean temperature in the core region of the channel is offered in panel b for clarity.

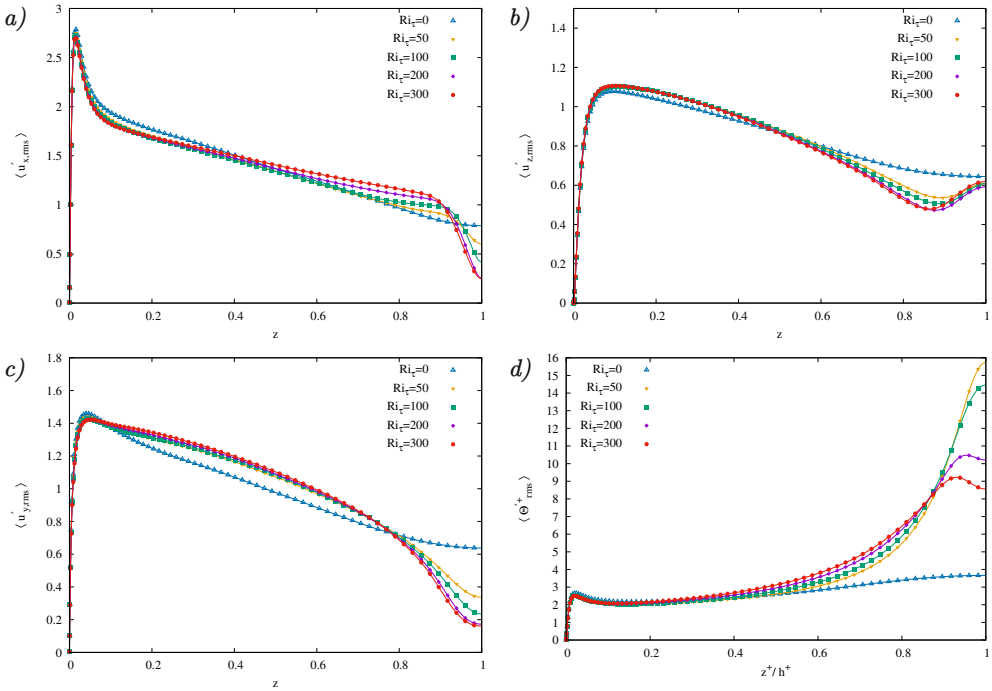

FIGURE 4.5 – Wall-normal behavior of the root mean square of velocity fluctuations in the streamwise direction ($\langle u'_{x,rms}\rangle$, panel a), in the spanwise direction ($\langle u'_{y,rms}\rangle$, panel b) and in the wall-normal direction ($\langle u'_{z,rms}\rangle$, panel c). The wall normal behavior of temperature fluctuations is also shown ($\langle \Theta'_{rms}\rangle$, panel d). Comparison between the reference case of unstratified turbulence ($Ri_\tau = 0$), and the stratified turbulence at $Ri_\tau = 50$, $Ri_\tau = 100$, $Ri_\tau = 200$ and $Ri_\tau = 300$ (filled symbols).

increase that – provided $Ri_\tau > 0$ – seems independent of the value of Ri_τ. This behavior, and in particular the increase of $\langle u'_{x,rms}\rangle$ and $\langle u'_{y,rms}\rangle$, is associated to the increase of velocity gradient (see also Fig. 4.6a and the discussion therein) in that region, while the corresponding decrease of $\langle u'_{z,rms}\rangle$ is due to the conversion of wall-normal momentum into potential energy. In the core region of the channel, $z > 0.8$, $\langle u'_{x,rms}\rangle$ strongly decreases while $\langle u'_{z,rms}\rangle$ develops a peak that is not visible in neutrally buoyant turbulence and is due to the presence of IGWs. Correspondingly, a marked peak at the channel center is also observed for the temperature fluctuations, Fig. 4.5d. Note that, for $\langle \Theta'_{rms}\rangle$, there is a clear crossover between the different cases of stratified turbulence: for increasing Ri_τ, temperature fluctuations tend to increase in the transition layer, $0.1 < z < 0.8$, and decrease in the core layer $0.8 < z < 1$ (though remaining much larger than the neutrally-buoyant case).

4.3 Momentum and heat fluxes

We focus here on the wall-normal behavior of momentum and heat fluxes, two key quantities in turbulent transport phenomena. The momentum flux can be obtained from the Reynolds-averaged streamwise momentum equation as

$$\tau_{tot} = 1 - \frac{2z^+}{Re_\tau} = \underbrace{\frac{\partial \langle u_x \rangle}{\partial z^+}}_{\tau^v_{xz}} + \underbrace{\langle u'_x u'_z \rangle}_{\tau^t_{xz}}, \tag{4.1}$$

where the turbulent $\left(\tau^t_{xy}\right)$ and viscous $\left(\tau^v_{xy}\right)$ counterparts to the overall stress are explicitly indicated. The behavior of τ^t_{xy} and τ^v_{xy} (symbols) is shown in Fg. 4.6a, together with the behavior of τ_{tot} (solid black line). Increasing Ri_τ, we note a general reduction of τ^t_{xy}, in particular in the core region, where $\langle u'_x u'_z \rangle \simeq 0$ for $Ri_\tau \geq 200$. Accordingly, a corresponding increase of τ^v_{xy} – and hence of the velocity gradient $\partial u_x / \partial z$ – is observed, so that the overall linear behavior of the total shear stress is recovered (Eq. 4.1). This is clearly visualized in the inset of Fig. 4.6a, where a close-up view of the behavior of τ^t_{xy} and τ^v_{xy} at the channel center, $0.8 < z < 1$, is given. In view of the present results, it is clear that the velocity increase observed at the channel center (see Fig. 4.3) is due to the reduction of turbulent momentum flux in the wall-normal direction (i.e. reduction of $u'_x u'_z$), and to the corresponding increase of the relative importance of τ^v_{xy} therein [137, 2].
Linked to the previous analysis of the wall-normal momentum flux, we now consider the wall-normal heat flux, whose behavior can be obtained from the Reynolds-averaged energy balance equation as

$$\langle u_z^{*'} \theta^{*'} \rangle - \alpha^* \frac{\partial \langle \theta^* \rangle}{\partial z^*} = \alpha^* \left[\frac{\partial \langle \theta^* \rangle}{\partial z^*} \right]_w = q^*_w, \tag{4.2}$$

where $\alpha^* = \nu^*/Pr$ is the thermal diffusivity. Normalizing Eq. 4.2 by $q^*_w = -\alpha^* \left[\frac{\partial \theta^*}{\partial z^*} \right]_w$, and recalling that $q^*_w = \theta^*_\tau u^*_\tau$, we finally obtain [2, 28]:

$$\frac{\langle u_z^{*'} \theta^{*'} \rangle}{q^*_w} - \frac{\alpha^* \frac{\partial \theta^*}{\partial z^*}}{q^*_w} = \underbrace{\langle u'_z \Theta' \rangle}_{\mathrm{q_t}} - \underbrace{\frac{1}{Pr} \frac{\partial \langle \Theta \rangle}{\partial z^+}}_{\mathrm{q_d}} = 1. \tag{4.3}$$

The two terms q_t and q_d, explicitly indicated in Eq. 4.3, represent the turbulent (usually referred to as buoyancy flux) and the diffusive counterparts to the total heat flux, and their behavior is shown in Fig. 4.6b. By looking at the profile of q_t, it is apparent that, while moving away from the wall – and no matter the value of Ri_τ – q_t increases sharply until it reaches a maximum value of approximately $q_t \simeq 0.95$ around $z \simeq 0.1$. In neutrally buoyant conditions, this peak value is kept almost unaltered throughout the entire channel, clearly corresponding to the constant flux hypothesis customarily assumed in neutral boundary layers [116, 79]. At larger Ri_τ, we observe a significant decrease of q_t in the core region of the channel. This decrease is so important that, for $Ri_\tau > 200$, $q_t \simeq 0$. Interestingly, and in agreement with previous observations [78, 28], we cannot find evidence of the speculated mean counter gradient

flux (or, in other words, negative q_t) at the center of the channel [54, 2]. Nevertheless, we plan to test our findings even at larger Ri_τ. Between the near wall and the core region of the channel there is a region in which q_t remains almost constant and close to unity for all cases considered here, with only a slight decrease for increasing Ri_τ. The diffusive heat flux q_d has a mirror-like behavior compared to q_t, since the total heat flux is constant across the channel, see Eq. 4.3: q_d decreases sharply while moving away from the wall and it subsequently increases – with the only exception of $Ri_\tau = 0$, for which it remains uniform and very low – in the core region of the channel. This trend of q_d is important to explain the non-monotonic behavior of the temperature profile observed in Fig. 4.4 (q_d is, by definition, proportional to the mean temperature gradient). Note indeed that the mean temperature gradient along the wall-normal direction can be conveniently expressed as [2]:

$$\frac{\partial\langle\theta\rangle}{\partial z} = \left[\frac{\partial\langle\theta\rangle}{\partial z}\right]_w \left[1 - \frac{\langle u_z^{*'}\theta^{*'}\rangle}{u_\tau^*\theta_\tau^*}\right], \tag{4.4}$$

where $[\partial\langle\theta\rangle/\partial z]_w$ is the dimensionless mean temperature gradient at the wall, i.e. the Nusselt number. Eq. 4.4, together with the observation that the buoyancy flux $q_t = \langle u_z^{*'}\theta^{*'}\rangle/u_\tau^*\theta_\tau^* = \langle u_z'\Theta'\rangle$ becomes almost zero for $Ri_\tau > 200$ (see Fig. 4.6b), indicates that for large stratification the temperature gradient at the channel center perfectly matches the temperature gradient at the wall. Since the temperature gradient at the wall (i.e. the Nusselt number) decreases for increasing Ri_τ, the same does the temperature gradient at the channel center (but only once Ri_τ is large enough for q_t to be approximately zero). To summarize, the temperature gradient at the channel center initially increases for increasing stratification, until the stratification becomes so strong to completely damp the turbulent heat transfer (buoyancy flux), i.e. $q_t = \langle u_z'\Theta'\rangle \simeq 0$, at the channel center. When it happens, the temperature gradient at the channel center – which becomes equal to the temperature gradient at the wall (Nusselt number) – decreases for increasing Ri_τ.

Despite the large fluctuations of temperature and wall-normal velocity observed around the channel center for increasing Ri_τ (Fig. 6.4c-d), the buoyancy flux $\langle u_z'\Theta'\rangle$ reduces remarkably down to the point at which, for $Ri_\tau \geq 200$, it completely vanishes. To understand the reason behind this behavior, we focus on the distribution of temperature, Θ', and wall-normal velocity fluctuations, u', on a wall-parallel plane $(x-y)$ located at the channel center. This is shown in Fig. 4.7 for $Ri_\tau = 0$ and $Ri_\tau = 300$. While for $Ri_\tau = 0$ (Fig. 4.7a-b), the picture displays the typical features of fully-developed turbulence, with spots of positive and negative temperature and wall-normal velocity randomly distributed over the considered plane, for $Ri_\tau = 300$ (Fig. 4.7c-d) the situation is different, and there seems to be a connection between Θ' and $u_z'^+$, which are both organized into stripes extending along the spanwise direction y. However, stripes of u_z' appear to lag behind those of Θ'^+. The phase lag between u_z' and Θ' distributions can be estimated by looking at the coherency spectrum

$$C_{u_z',\Theta'}(\kappa_w) = \int_{-\infty}^{\infty} R_{u_z',\Theta'}(s)\exp\left(-2\pi j s\kappa_w\right)\mathrm{d}s, \tag{4.5}$$

with $\kappa_w = k^*h^*$ the dimensionless wavenumber and $R_{u_z',\Theta'}$ the correlation coefficient between u_z' and Θ'. In particular, it is intriguing to focus on the phase of $C_{u_z',\Theta'}(\kappa_w)$.

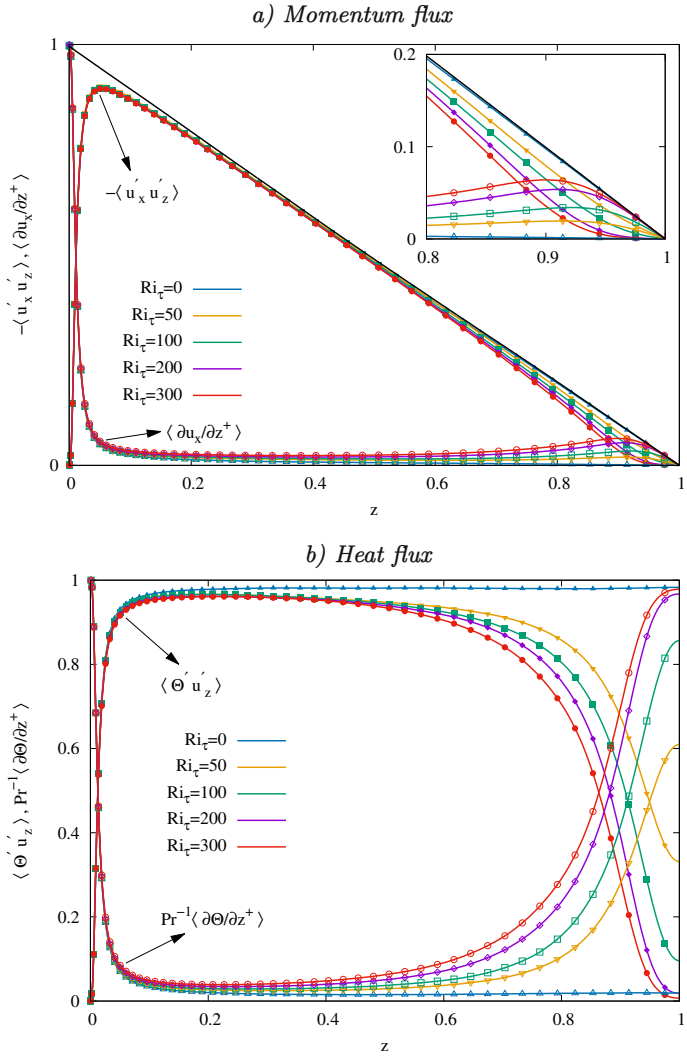

FIGURE 4.6 – Panel a): Wall-normal behavior of the viscous shear stress, $\tau_{xy}^v = \partial\langle u_x \rangle/\partial z^+$ and turbulent shear stress, $\tau_{xy}^t = \langle u_x' u_z' \rangle$. The linear behavior of the total shear stress, $\tau_{tot}^*/(\rho^* u_\tau^{*2})$ is also shown by the black solid line. Comparison between the reference case of unstratified turbulence ($Ri_\tau = 0$), and the cases of stratified turbulence at $Ri_\tau = 50$, $Ri_\tau = 100$, $Ri_\tau = 200$ and $Ri_\tau = 300$ (filled symbols). Panel b): Wall-normal behavior of the diffusive heat flux, $q_d = Pr^{-1}\partial\langle\Theta\rangle/\partial z^+$ and turbulent heat flux (buoyancy flux), $q_t = \langle u_z'\Theta' \rangle$. Comparison between the reference case of unstratified turbulence ($Ri_\tau = 0$), and the cases stratified turbulence at $Ri_\tau = 50$, $Ri_\tau = 100$, $Ri_\tau = 200$ and $Ri_\tau = 300$ (filled symbols).

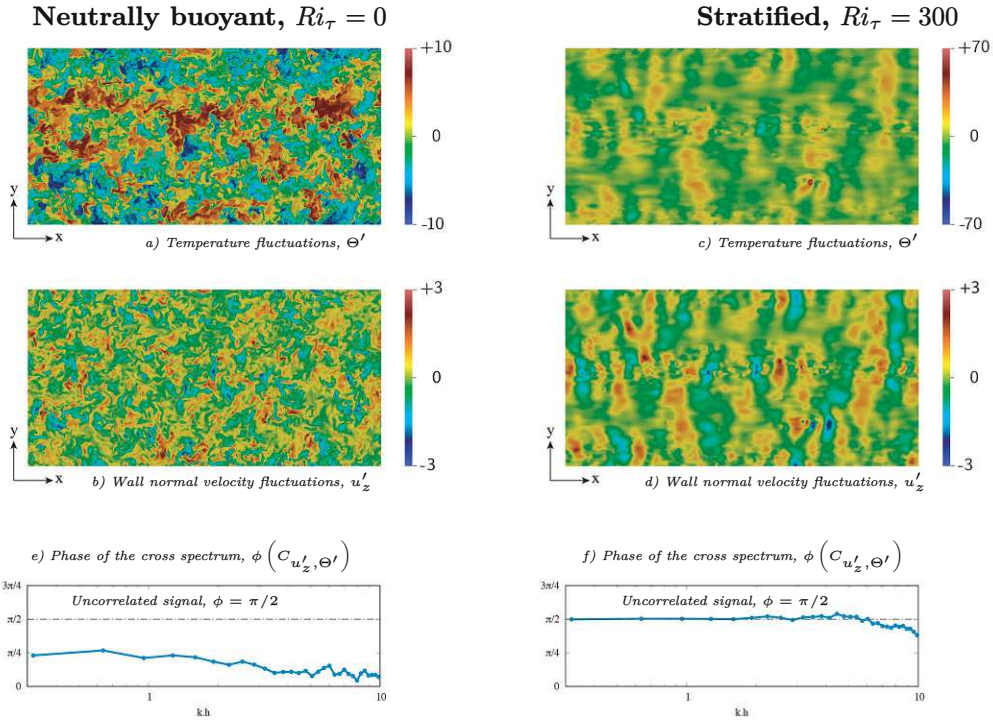

FIGURE 4.7 – Temperature and velocity fluctuations on a wall-parallel $(x-y)$ plane located at the channel center for $Ri_\tau = 0$ (panel a and b) and for $Ri_\tau = 300$ (panel c and d). Phase of the cross spectrum, $\phi\left(C_{u'_z,\Theta'}\right)$, as a function of the wavenumber $\kappa_w = k^* h^*$ for $Ri_\tau = 0$ (panel e) and for $Ri_\tau = 300$ (panel f).

As shown in Fig. 4.7f, we clearly notice that, for $Ri_\tau = 300$, u'_z and Θ' are shifted by $\pi/2$ (see Fig. 4.7f). Such a phase delay is clearly not observed at $Ri_\tau = 0$ (see Fig. 4.7e). This result confirms and extends previous observations obtained at smaller Re_τ (see [46]). It is important to note that the presence of this phase shift explains why, although temperature and wall-normal fluctuations are both very large at the channel center, their correlation – that is, the buoyancy flux $\langle u'_z \Theta' \rangle$ –, is almost zero: where Θ' is maximum in magnitude, $u'_z \simeq 0$ and viceversa, consistently with the presence of a wavy motion (IGW).

Not only the average value of the buoyancy flux q_t is important, but also its distribution in space and time. To understand it, we focus on the two limiting cases $Ri_\tau = 0$ and $Ri_\tau = 300$ and we look at the behavior of q_t, normalized by the corresponding maximum $q_{t,max}$, on a wall-parallel plane $(x-y)$ located at the channel center (Fig. 4.8, panels a-b). Then, we compute the corresponding probability density function $\Pi(q_t/q_{t,max})$ (Fig. 4.8c).

For $Ri_\tau = 0$ (blue line in Fig. 4.8c), $\Pi(q_t/q_{t,max})$ is highly asymmetric, with the most probable value occurring for $q_t/q_{t,max} = 0$ and with larger positive fluctuations compared to negative ones. This suggests that, although the mean temperature difference

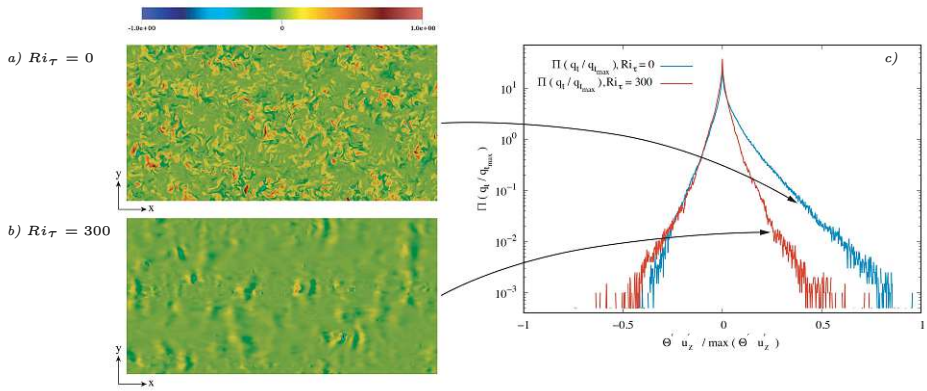

FIGURE 4.8 – Contour map of the turbulent heat flux $q_t = \langle \Theta u_z' \rangle$ on a wall-parallel $(x-y)$ plane located at the channel center for $Ri_\tau = 0$ (panel a), for $Ri_\tau = 300$ (panel b), and corresponding probability density function $\Pi(q_t)$ (panel c).

between the walls induces a net positive wall-normal energy flux (i.e. the mean value $\langle u_z' \Theta' \rangle > 0$), $u_z' \Theta'$ can often be negative, indicating the presence of regions characterized by local counter gradient heat fluxes. The occurrence of localized countergradient heat fluxes is an extremely important phenomenon that has been observed also in other situations [43, 141, 36]. From a physical point of view, small positive and negative values of $\Theta' u_z'$ are due to turbulence, which is characterized by uncorrelated velocity and temperature fluctuations. These small positive and negative values of $\Theta' u_z'$, which are equally likely events, balance each other and do not contribute to the net heat transport [102]. Only large velocity and temperature fluctuations produced by larger coherent structures are correlated and contribute to the net heat flux. And clearly, large positive fluctuations are larger than negative ones, so to produce a positive net heat flux.

The asymmetry of $\Pi(q_t/q_{t,max})$ is almost completely absent at $Ri_\tau = 300$. In particular, while the probability of observing positive fluctuations is globally reduced (i.e. there is a reduction of large correlated velocity and temperature fluctuations), negative fluctuations are rather persistent, so that the average value of $q_t/q_{t,max}$ is close to zero. This is nicely rendered by the contour maps of $q_t/q_{t,max}$ shown in Fig. 4.8b: while most of the plane is characterized by a correlation $q_t/q_{t,max} \approx 0$ (and corresponding to the most probable value of $\Pi(q_t/q_{t,max})$ in Fig. 4.8), small and rare patches of large positive $q_t/q_{t,max}$ coexist with small and rare patches of large negative $q_t/q_{t,max}$.

4.4 Macroscopic characterization of the flow: Ri_b, C_f, Nu

Although the shear Richardson number Ri_τ is customarily used to characterize the flow in numerical simulations of wall-bounded stratified turbulence [142], its use in

experiments/field measurements is much more limited. The reason is the difficult experimental evaluation of the shear velocity, which in turn requires the measurement of the shear stress at the wall. As a consequence, in many experiments the bulk Richardson number $Ri_b = \beta^*(\Delta\theta^*/2)g^*h^*/(2u_b^{*^2})$ is usually preferred, since the bulk velocity u_b^* is an easily accessible quantity. To draw a link between simulations and experiments/field measurements, it is interesting to evaluate the behavior of the bulk Richardson number Ri_b, as a function of the shear Richardson number Ri_τ. This behavior is shown in Fig.4.9. Present results (filled symbols, ●), which are plot together with literature results obtained at lower Re_τ ([28], open symbols), confirm previous indications that $Ri_b \propto Ri_\tau^{2/3}$. In view of its independence on Re_τ – at least over about one decade, from $Re_\tau = 180$ up to $Re_\tau = 1000$ –, the proposed Ri_b scaling seems a general property of the flow that can be used as a robust parametrization tool, as will be shown below.

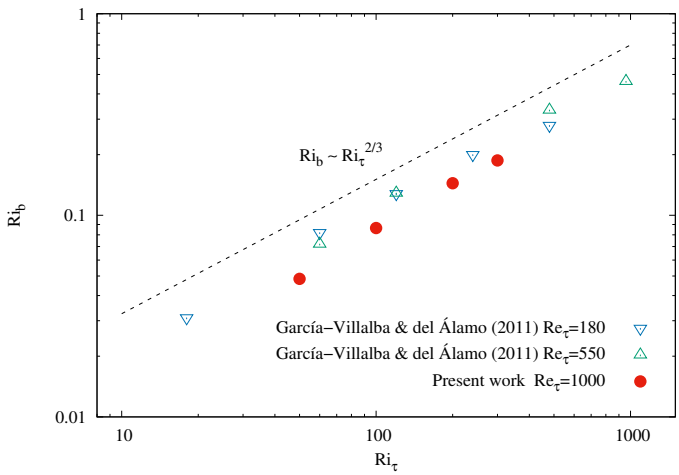

FIGURE 4.9 – Bulk Richardson number, Ri_b, as a function of the shear Richardson number, Ri_τ, for the present simulations at $Re_\tau = 1000$, and for previous simulations at $Re_\tau = 180$ and $Re_\tau = 550$ [28]. The proposed scaling $Re_b \sim Ri_\tau^{2/3}$ is also explicitly indicated.

Perhaps the most important quantities to be monitored in wall-bounded stratified turbulence are the overall momentum and heat transfer rates, which are commonly quantified in terms of the friction factor C_f – shear stress to kinetic energy ratio – and by the the Nusselt number Nu – convective to conductive heat transfer ratio – as:

$$\begin{cases} C_f = \dfrac{2\tau_w^*}{\rho^* u_b^{*^2}}, \\ Nu = \dfrac{2q_w^* h^*}{\lambda^* \Delta\theta^*}. \end{cases} \tag{4.6}$$

Results obtained from the present simulations are shown by filled symbols (●) in Fig. 4.10-4.11, together with the results obtained in previous studies [28, 2, 29, 144, 140].

Focusing on C_f (Fig. 4.10), it is clear that an increase of stratification (increase of Ri_τ) reduces the wall-normal momentum transfer, via the reduction of wall-normal turbulent transport and via the corresponding increase of the volume flowrate (keeping the imposed pressure gradient constant). Interestingly, recalling that $Ri_b \propto Ri_\tau^{2/3}$ (see Fig.4.9), and considering that $C_f/4 = Ri_b/Ri_\tau$, we obtain $C_f \sim Ri_\tau^{-1/3}$ [28]. This scaling law, which is shown in Fig.4.10 together with the reported numerical results, predicts fairly well the behavior of C_f for a broad range of Ri_τ, with some departure observed only at very large stratification levels (when local flow laminarization is likely to start).

The fair collapse observed for C_f is not recovered for the Nusselt Number Nu (not shown in Fig. 4.11). Interestingly, when rescaled by $Re_\tau^{-2/3}$, the collected results collapse nicely (Fig. 4.11)) and scale as $Nu \cdot Re_\tau^{-2/3} \sim Ri_\tau^{-1/3}$ (therefore giving $Nu \cdot Re_\tau^{-2/3} \sim C_f$). The proposed scaling differs from classical analogies widely used in literature – like the Chilton and Colburn one $C_f/2 = Nu \cdot Re^{-1} \cdot Pr^{-1/3}$ [9] – to relate heat, mass and momentum transfer coefficients. It is reasonable to expect that the interaction between buoyancy and momentum modifies the main transport processes in a non-trivial way that is hard to predict by simplified assumptions. An in-depth analysis and a corresponding accurate parametrization of the actual flow field are therefore required to shed some light on the proposed scaling, which however appear rather robust.

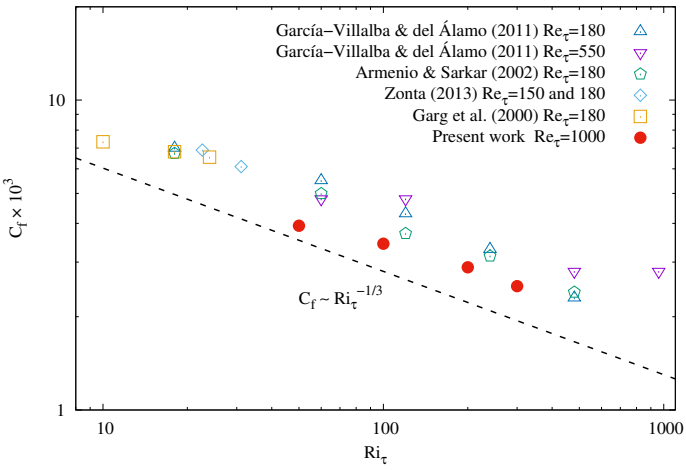

FIGURE 4.10 – Friction factor C_f as a function of the shear Richardson number Ri_τ. Results of present study (filled symbols) are shown together with results obtained in previous studies [29, 2, 28, 144, 140]. The proposed scaling $C_f \sim Ri_\tau^{-1/3}$ is also explicitly indicated.

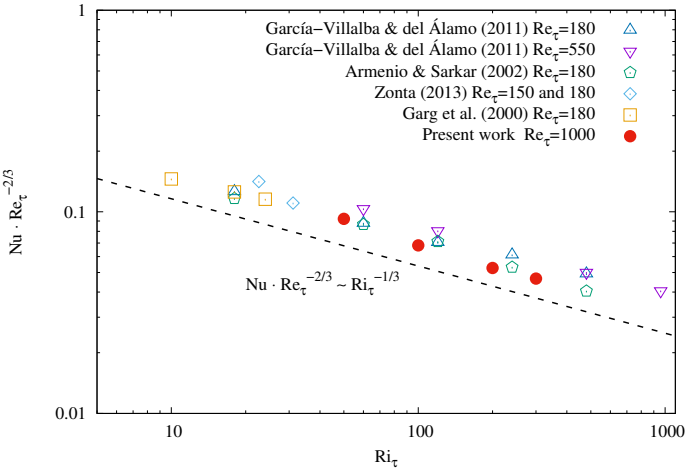

FIGURE 4.11 – Rescaled Nusselt number $Nu \cdot Re_\tau^{-2/3}$ as a function of the shear Richardson number Ri_τ. Results of present study (filled symbols) are shown together with results obtained in previous studies [29, 2, 28, 144, 140]. Note that the values of Nu in [144] and [140], obtained at $Pr = 3$, have been rescaled by $Pr^{1/3}$. The proposed scaling $Nu \cdot Re_\tau^{-2/3} \sim Ri_\tau^{-1/3}$ is also explicitly indicated.

4.5 Internal gravity waves

Internal gravity waves propagate in stably stratified flows [111]. When a fluid particle is displaced in the wall-normal direction, it tends to be restored to its original position; however, it may overshoot inertially and oscillate about this point [144]. To characterize the frequency of oscillation, buoyancy frequency N (or Brunt–Väisälä frequency) is commonly introduced. In dimensional form, it is defined as

$$N^* = \sqrt{-g^*\beta^*\frac{\partial\langle\theta^*\rangle}{\partial z^*}} \tag{4.7}$$

In Fig .4.12, we show the dimensionless buoyancy frequency $N = N^*h^*/u_\tau^*$ as a function of wall-normal distance for different shear Richardson numbers. Except for a narrow region at the channel center, where the action of IGWs is detected [2, 28], N is rather small in the remaining part of the channel. The increase of N at the channel walls is less significant, since it is induced by the confinement effect due to the boundary condition.

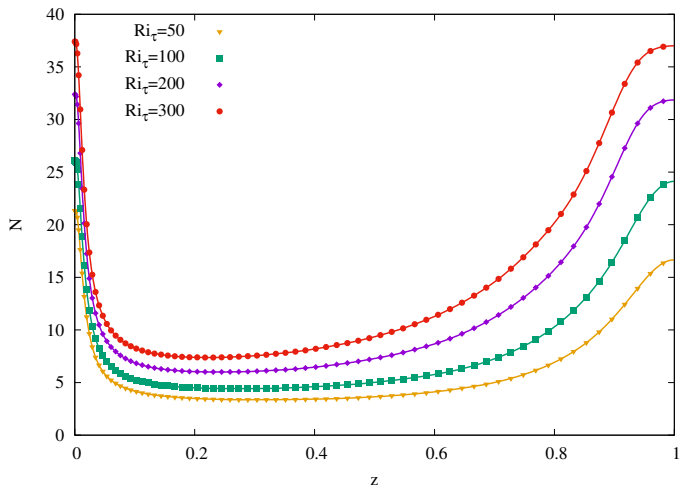

FIGURE 4.12 – Dimensionless buoyancy frequency (Brunt–Väisälä frequency) as a function of wall-normal distance for different shear Richardson numbers.

The peak of N, located at the channel center is linked with the sharpening of the mean temperature profile (Fig. 4.4). In this region, the peak of N increases as stratification increases, indicating that a higher stratification affects the structures of the core region more strongly. Using the buoyancy frequency N, we can calculate the gradient Richardson number as

$$Ri_g = \frac{N^2}{S^2} = \frac{-g^*\beta^*\frac{\partial\langle\theta^*\rangle}{\partial z^*}}{\left(\frac{\partial\langle u_x^*\rangle}{\partial z^*}\right)^2} \tag{4.8}$$

where S is the shear rate. Ri_g has been broadly employed as the key parameter in the studies of homogeneous stratified turbulence because of the spatially constant value of Ri_g [95, 39]. In these studies, $Ri_g \simeq 0.25$ has been identified as a critical value for describing the nature of the flow structure. For $Ri_g \simeq 0.25$, turbulence does not grow or decay. For large Ri_g, turbulence decays, while for small Ri_g it grows.
In particular in linear stability analysis [71], $Ri_g \geq 0.25$ is considered as a sufficient condition to obtains flow laminarization. This has also been confirmed experimentally [85, 95]. A large variation of Ri_g across the channel has been observed in the previous numerical studies of wall-bounded stably-stratified turbulent flows by Armenio and Sarkar [2], Taylor et al. [115], García-Villalba & del Álamo [28] and Zonta *et al.* [144]. Their results showed that Ri_g varies from very small values close to the wall, to very large values close to the center of the channel. In Fig. 4.13, we represent the Ri_g in logarithmic scale as a function of the dimensionless wall-normal distance for different Ri_τ. A good agreement can be found between the results presented in Fig. 4.13 and previous studies [2, 115, 28, 144]. A sharp increase of the slope of Ri_g profiles can be seen at the core region of the channel, where the values of Ri_g are above ≈ 0.2. This large variation of Ri_g along the wall-normal direction is due to the fact that in the core region $\partial\langle u_x\rangle/\partial z \to 0$ and therefore Ri_g is very large, while in the near-wall region $\partial\langle u_x\rangle/\partial z$ is large and Ri_g becomes small. In the center of the channel, due to the symmetry condition, $\partial\langle u_x\rangle/\partial z = 0$ and Ri_g diverges. Another important observation from figure 4.13 is that the regions where Ri_g is bellow ≈ 0.2 are the turbulent regions, while the regions where Ri_g is above ≈ 0.2 are the regions where the turbulence activity is weakened and the internal gravity waves are dominant.

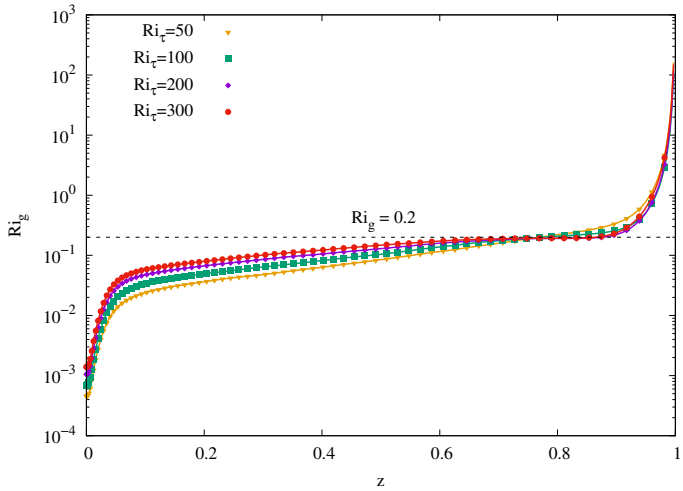

FIGURE 4.13 – Gradient Richardson number as a function of wall-normal distance for different shear Richardson numbers.

To investigate the effect of buoyancy on eddy size, we compute the streamwise energy spectra of wall-normal velocity fluctuations [46, 137, 144]. In Fig. 4.14, we show the premultiplied streamwise energy spectral density of the wall-normal velocity fluctu-

ations at the channel center ($z^+ = 1000$) for different levels of stratification. The footprint of IGWs can be clearly observed from the peak of energy spectral density occurred at the dimensionless wave number $k_x^* h^* \approx 5$ (k_x^* is the wave number in dimensional form), which is not present in the neutrally-buoyant condition. The effect of IGWs is to induce fluctuations of wall-normal velocity at the characteristic frequency of the waves [144]. This correlation is demonstrated by Zonta et al. [144] by assuming that IGWs move with a velocity similar to the fluid velocity at the centerline. Here we focus on the case $Ri_\tau = 300$, where the effect of stratification is stronger. It can be seen from Fig. 4.3 that $\langle u_x \rangle$ reaches a maximum $\simeq 47$ at the channel center. Following the assumption made by Zonta et al. [144], we can assume that $u_{wave} \simeq 47$ and therefore $u^*_{wave} = u_{wave} \times u^*_\tau \simeq 1\, m/s$. The associated frequency is $f^*_{wave} = u^*_{wave} \times k^*_x / 2\pi \simeq 1\, s^{-1}$. The dimensionless buoyancy frequency at the channel center is $N \simeq 38$ (see Fig. 4.12), which in dimensional form is $N^* = N u^*_\tau / h^* \simeq 1\, s^{-1}$. These two calculations are in good agreement with each other.

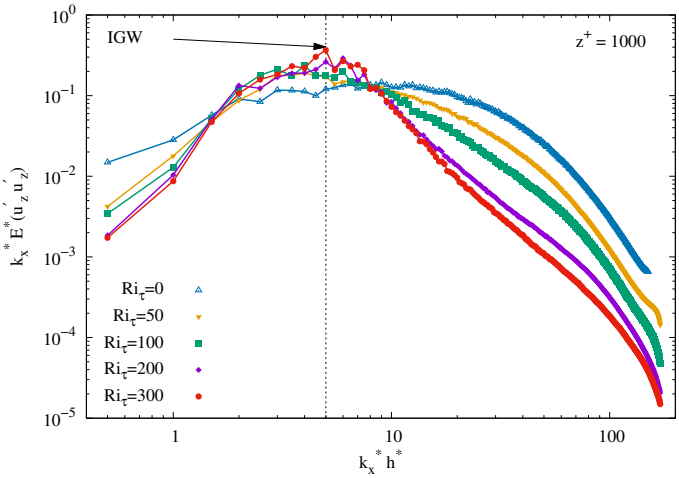

FIGURE 4.14 – Premultiplied streamwise energy spectral density of the wall-normal velocity fluctuations at the channel center ($z^+ = 1000$) for different shear Richardson numbers as a function of wave number.

Note that a physically sound approach to investigate the dynamics of IGWs is to separate large scale, coherent, fluctuations from small scale incoherent ones. To do so, a triple decomposition [44, 108] is usually employed. In the framework of this thesis, we have tried to decompose the fluctuations into coherent and incoherent ones, but we were not able to obtain convincing results, likely because IGWs can lose some coherency in the spanwise direction. Very recently, the dynamical properties of IGWs, and the interaction between IGWs and wall turbulence has successfully studied by Lloyd et al. [65]. This will be the subject of a future investigation.

5

Energetics and mixing in wall-bounded stably-stratified turbulence

Reproduced in part from:

P. Hadi Sichani, F. Zonta and A. Soldati, *Energetics and mixing in wall-bounded stably stratified turbulent flow at* $Re_\tau = 1000$, Phys. Rev. Fluids, in preparation.

This chapter explores the stably-stratified wall-bounded turbulence from the energetics perspective. In section 5.1, we analyze the energy exchange between different energy reservoirs by computing different budget equations. Turbulent kinetic energy (TKE), mean kinetic energy (MKE), fluctuating temperature variance (FTV), mean temperature variance (MTV) and total potential energy (TPE) budget equations are introduced and numerically analyzed. We then analyze the effect of stratification on energy transfer via different mechanisms. We demonstrate that the turbulence activity is almost completely suppressed in a narrow region at the channel center, where buoyancy leaves its most significant footprint on the flow dynamics. In section 5.2, we investigate the vertical turbulent mixing of momentum and heat in wall-bounded stratified turbulence at $Re_\tau = 1000$. Finally, we present a new parameterization for the irreversible flux Richardson number. This new parameterization performs better for our current results compared to the parameterization proposed by Venayagamoorthy & Koseff [127]. We speculate that the better performance of this parameterization is because our simulations include the effect of wall in the irreversible flux Richardson number.

5.1 Energetics in wall-bounded stably-stratified turbulence

5.1.1 Turbulent kinetic energy (TKE) budget

To obtain the TKE $= \frac{1}{2}u'u'$ budget equation, we first decompose the velocity vector into the mean and fluctuating components ($u_i = \langle u_i \rangle + u_i'$). Then we multiply the (Reynolds) decomposed Navier–Stokes equations by the fluctuating velocity field u_i', and we take an ensemble averaging [68, 51]. The TKE budget equation in dimensionless form becomes

$$\frac{D[TKE]}{Dt} = \underbrace{\left[-\frac{\partial \langle u_i' p' \rangle}{\partial x_i}\right]}_{\Pi_k} + \underbrace{\left[-\langle u_i' u_j' \rangle \frac{\partial \langle u_i \rangle}{\partial x_j}\right]}_{P_k} + \underbrace{\left[-\frac{1}{2}\frac{\partial \langle u_i' u_i' u_j' \rangle}{\partial x_j}\right]}_{T_k} + \underbrace{\left[\frac{1}{2Re_\tau}\frac{\partial^2 \langle u_i' u_i' \rangle}{\partial x_j^2}\right]}_{D_k} + \underbrace{\left[-\frac{1}{Re_\tau}\left\langle \frac{\partial u_i'}{\partial x_j}\frac{\partial u_i'}{\partial x_j}\right\rangle\right]}_{\epsilon_k} + \underbrace{[Ri_\tau \langle u_z' \theta' \rangle]}_{\Phi_z} \tag{5.1}$$

The terms on the right-hand side represent the pressure diffusion, Π_k, the production of TKE, P_k, the turbulent diffusion, T_k, the viscous diffusion of TKE, D_k, the turbulent viscous dissipation, ϵ_k ,and the buoyancy flux, Φ_z. The material derivative of TKE (The term on the left-hand side of Eq. 5.1) is zero because the flow is statistically steady. The TKE production term, P_k, accounts for the generation of velocity fluctuations via mean shear. This term represents a source in the TKE budget equation. The energy injected via P_k is entirely balanced by the dissipation of TKE, ϵ_k, and buoyancy flux, Φ_z, which are the sink terms in Eq. 5.1. The pressure diffusion, Π_k, the turbulent diffusion, T_k, and the viscous diffusion, D_k, are redistribution terms with no net contribution. The buoyancy flux , Φ_z, which is the only term directly influenced by buoyancy, is also the only term that is responsible for the exchange between the kinetic and potential energy [83]. The other terms in TKE budget are affected by stratification indirectly since the temperature field influences the velocity field by acting as an active scalar. In Fig. 5.1, we show different terms of TKE budget equation (Eq. 5.1) for the neutrally-buoyant case ($Ri_\tau = 0$) and $Ri_\tau = 300$ normalized by $u_\tau^{*^4}/\nu^*$. Profiles for $Ri_\tau = 50$, 100 and 200 are not included in Fig. 5.1 since they exhibit an intermediate behavior and therefore, do not add to the discussion. The buoyancy flux term, Φ_z, is also not shown in Fig. 5.1 because it is rather small compared to the other right-hand side terms of Eq. 5.1.

In Fig. 5.1, filled symbols are used to plot the TKE budget terms for the neutrally-buoyant case ($Ri_\tau = 0$), whereas open symbols refer to the $Ri_\tau = 300$ case. The largest effect of stratification is on the TKE production and viscous dissipation in the core region of the domain, where buoyancy plays a dominant role. In the near-wall region, all terms are important. By contrast, moving towards the channel center, the two leading terms are P_k and ϵ_k, which nicely balance each other. The inset of Fig. 5.1 shows ϵ_k close to the channel center ($900 < z^+ < 1000$). Please note that, unlike the main panel, the x-axis of the inset is linear.

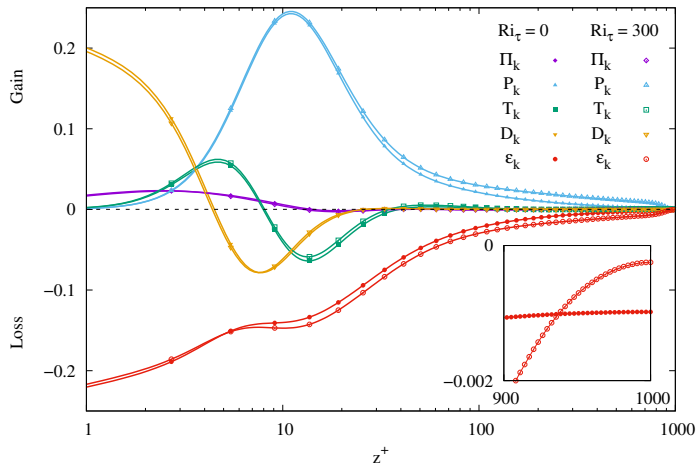

FIGURE 5.1 – TKE budget for neutrally-buoyant case (filled symbols) and $Ri_\tau = 300$ case (open symbols). The inset represents the turbulent viscous dissipation close to the channel center for both unstratified and stratified cases.

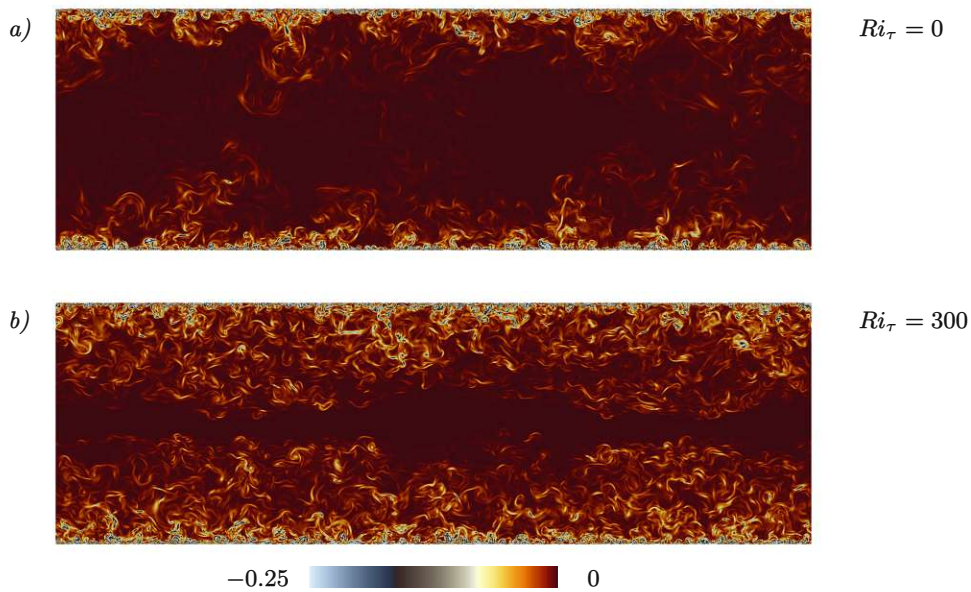

FIGURE 5.2 – Contour maps of TKE viscous dissipation, ϵ_k, on a $(y-z)$ cross section located at $x = Lx/2$. Panel a) refers to the neutrally-buoyant case, $Ri_\tau = 0$. Panel b) refers to the stably-stratified case at $Ri_\tau = 300$.

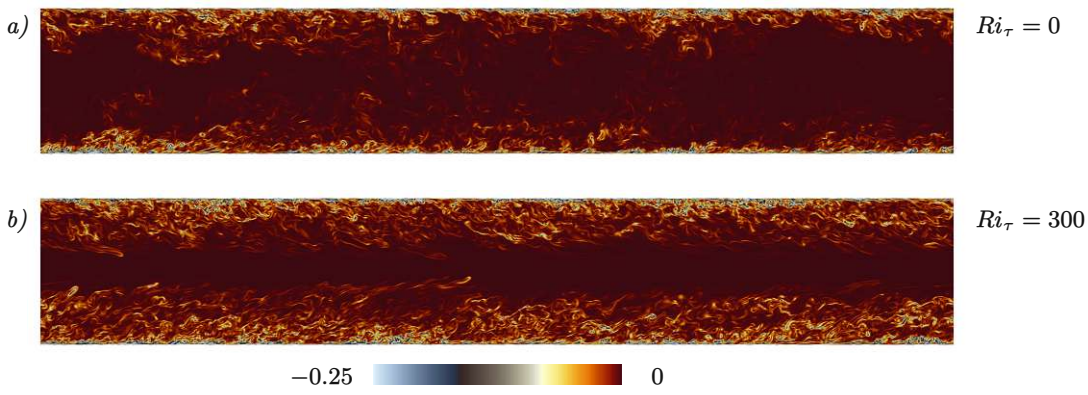

FIGURE 5.3 – Contour maps of TKE viscous dissipation, ϵ_k, on a $(x - z)$ longitudinal section located at $y = Ly/2$. Panel a) refers to the neutrally-buoyant case, $Ri_\tau = 0$. Panel b) refers to the stably-stratified case at $Ri_\tau = 300$.

It can be seen from the inset of Fig. 5.1 that there is a cross-over between ϵ_k for $Ri_\tau = 300$ and ϵ_k for $Ri_\tau = 0$ at $z^+ \approx 950$. ϵ_k for $Ri_\tau = 300$ tends to almost zero at the channel center. This narrow region at the core of the channel, where buoyancy leaves its most significant footprint on the flow field, represents a strong barrier to the wall-normal heat and momentum transport. This behavior can also be observed quantitatively in Figs. 5.2 and 5.3. The contour maps of ϵ_k can be seen on a cross section located at $x = L_x/2$ in Fig. 5.2 and on a longitudinal section located at $y = L_y/2$ in Fig. 5.3 for $Ri_\tau = 0$ and $Ri_\tau = 300$. Note that the range of the values shown in Figs. 5.2 and 5.3 are between zero and the mean value evaluated at the wall (-0.25). The largest variability of ϵ_k occurs in wall-normal direction. ϵ_k reaches its maximum in magnitude at the walls, where turbulence is the only mechanism controlling the flow dynamics. For the neutrally-buoyant case, ϵ_k reaches the value ≈ -23, and for the $Ri_\tau = 300$ case this value is ≈ -32. However the mean value of ϵ_k at the wall for both cases remain very close to each other (the average ϵ_k at the wall for both unstratified and stratified case is -0.25). At the channel center ϵ_k reaches a mean value equal to zero. It can be seen that regardless of stratification effects, the largest variation of ϵ_k is in the near-wall region. In panel b) of Figs. 5.2 and 5.3, it is observable that in a narrow region at the channel center ϵ_k is almost zero, however for the unstratified case some variation of ϵ_k can still be seen in this region. This narrow region refers to the region, shown in the inset of Fig. 5.1 $(950 < z^+ < 1050)$, where buoyancy is able to kill turbulence.

To examine the variation of ϵ_k quantitatively in this region, we compute the probability density function (PDF) of ϵ_k inside two subdomains. The two subdomains have a volume of $L_x \times L_y \times z_\epsilon$, where z_ϵ in inner units is $950 < z_\epsilon^+ < 1050$ for the first subdomain, and $900 < z_\epsilon^+ < 1100$ for the second subdomain. In Fig. 5.4, we show the PDF of ϵ_k normalized by the mean value of ϵ_k at each subdomain for each dataset. It can be seen that the most probable events are the values of ϵ_k very close to zero. The tails of the PDF are not shown down to the smallest values, since it does not

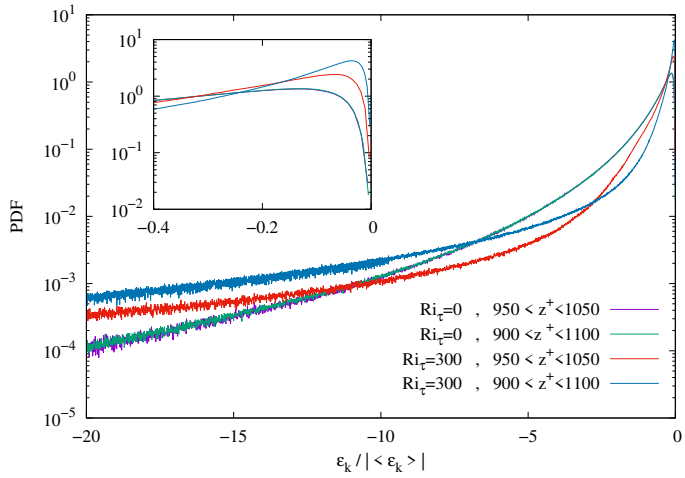

FIGURE 5.4 – PDF of $\epsilon_k / \mid \langle \epsilon_k \rangle \mid$ for neutrally-buoyant case and $Ri_\tau = 300$ case inside two different subdomains.

add to the discussion. It can be seen from Fig. 5.4 that for the unstratified case the PDF of $\epsilon_k / \mid \langle \epsilon_k \rangle \mid$ collapse on top of each other, meaning that the ϵ_k does not change significantly between the two subdomains. For the stratified case, the probability of having values of ϵ_k very close to zero is higher in $950 < z^+ < 1050$ compared to $900 < z^+ < 1100$. This confirms the observation we had from the inset of Fig. 5.1. It suggests that in a narrow region of $950 < z^+ < 1050$ buoyancy is able to kill the activity of turbulent viscous dissipation almost completely.

5.1.2 Mean kinetic energy (MKE) budget

To derive the MKE $= \frac{1}{2}\langle u_i \rangle \langle u_i \rangle$ budget equation, the Reynolds-decomposed Navier–Stokes equations is multiplied by the mean velocity field $\langle u_i \rangle$, and an ensemble averaging is taken. The MKE transport equation in dimensionless form is

$$\frac{D[MKE]}{Dt} = \underbrace{\left[-\langle u_i \rangle \frac{\partial \langle p \rangle}{\partial x_i}\right]}_{\widetilde{\Pi_k}} + \underbrace{\left[\langle u_i' u_j' \rangle \frac{\partial \langle u_i \rangle}{\partial x_j}\right]}_{\widetilde{P_k}} + \underbrace{\left[-\frac{\partial \left(\langle u_i' u_j' \rangle \langle u_i \rangle\right)}{\partial x_j}\right]}_{\widetilde{T_k}} + \underbrace{\left[\frac{1}{2Re_\tau}\frac{\partial^2 \langle u_i \rangle^2}{\partial x_j^2}\right]}_{\widetilde{D_k}} + \underbrace{\left[-\frac{1}{Re_\tau}\left\langle \frac{\partial \langle u_i \rangle}{\partial x_j}\frac{\partial \langle u_i \rangle}{\partial x_j}\right\rangle\right]}_{\widetilde{\epsilon_k}} \tag{5.2}$$

The left-hand side of Eq. 5.2 represents the material rate of change of MKE, and it is equal to zero as the flow is in a statistically steady condition. The different terms on the right-hand side of Eq. 5.2 represent the power injected in the system via the mean

pressure gradient, $\widetilde{\Pi_k}$, the production of TKE, $\widetilde{P_k}$, the work done by the Reynolds stresses, $\widetilde{T_k}$, the viscous diffusion of MKE, $\widetilde{D_k}$, and the mean flow viscous dissipation, $\widetilde{\epsilon_k}$. It should be noted that $\widetilde{P_k}$, which is a source term in TKE acts as a sink term in the MKE budget equation ($\widetilde{P_k} = -P_k$).

The energy input, $\widetilde{\Pi_k}$, is acting as a source term and it represents the energy injected into the system through the mean pressure gradient. This energy is then partially dissipated by the mean flow viscous dissipation, $\widetilde{\epsilon_k}$, and partially used to generate turbulent fluctuations via the production term, $\widetilde{P_k}$. Therefore, $\widetilde{\epsilon_k}$ and $\widetilde{\Pi_k}$ represent a sink of energy in the MKE balance equation. The two remaining terms, the energy transport by the Reynolds stress, $\widetilde{T_k}$, and the viscous diffusion, $\widetilde{D_k}$, redistribute the energy across the channel and thus act only as internal transport mechanisms that do not bear a net contribution. In other words, they are neither sinks nor sources [94].

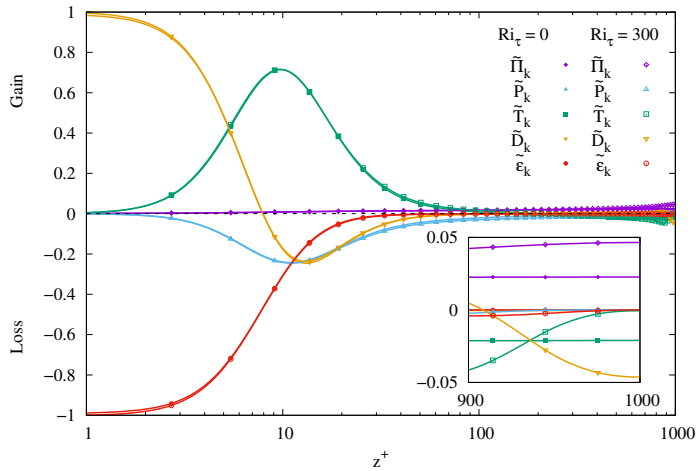

FIGURE 5.5 – Budget of MKE for neutrally-buoyant case (filled symbols) and $Ri_\tau = 300$ case (open symbols).

In Fig. 5.5, the different terms of MKE budget equation (Eq. 5.2) normalized by u_τ^{*4}/ν^* are shown for the neutrally-buoyant case ($Ri_\tau = 0$) with filled symbols and stratified case ($Ri_\tau = 300$) with open symbols. In the near-wall region (up to $z^+ \approx 5$), the mean flow viscous dissipation, $\widetilde{\epsilon_k}$ is balanced by the viscous diffusion, $\widetilde{D_k}$. In the buffer region ($5 < z^+ < 30$), all terms play an important role [67]. In this region, $\widetilde{T_k}$ and $\widetilde{\Pi_k}$ balance the energy losses from $\widetilde{\epsilon_k}$, $\widetilde{D_k}$ and $\widetilde{P_k}$. In these two regions, the stratification is not affecting the transport of MKE. However, MKE transport is modulated by buoyancy in the core region of the channel, where the energy injected into the system $\widetilde{\Pi_k}$ is balanced by $\widetilde{T_k}$ (mean flow energy is converted to turbulence). The stratification becomes very important for $z^+ > 950$. In this narrow region, or the stratified case ($Ri_\tau = 300$), the energy injected into the system via the mean pressure gradient is not anymore balanced by the energy transported by Reynolds stress, as for the neutrally-buoyant case, but it is balanced by viscous diffusion, $\widetilde{D_k}$. A

similar behavior was also reported for ϵ_k in Sec. 5.1.1, and it confirms that the region $950 < z^+ < 1000$ represents (because of the buoyancy effect) a strong barrier to the transport of heat and momentum.

5.1.3 Fluctuating temperature variance (FTV) budget

The budget equation of FTV $= \frac{1}{2}\theta'\theta'$ is obtained by multiplication of the fluctuating temperature field θ' by Reynolds-decomposed energy equation. The ensemble averaged FTV budget equation in dimensionless form is given as

$$\frac{D[FTV]}{Dt} = \underbrace{\left[-\langle u_j'\theta'\rangle \frac{\partial\langle\theta\rangle}{\partial x_j}\right]}_{P_\theta} + \underbrace{\left[-\frac{1}{2}\frac{\partial\langle u_j'\theta'\theta'\rangle}{\partial x_j}\right]}_{T_\theta} + \underbrace{\left[\frac{1}{2Re_\tau Pr}\frac{\partial^2\langle\theta'\theta'\rangle}{\partial x_j^2}\right]}_{D_\theta} + \underbrace{\left[-\frac{1}{Re_\tau Pr}\left\langle\frac{\partial\theta'}{\partial x_j}\frac{\partial\theta'}{\partial x_j}\right\rangle\right]}_{\epsilon_\theta} \tag{5.3}$$

The left-hand side of Eq. 5.3 represents the material derivative of FTV. The terms on the right-hand side of Eq. 5.3 represent the production of turbulent fluctuating temperature, P_θ, the turbulent diffusion of temperature fluctuations, T_θ, the molecular diffusion of temperature fluctuations, D_θ, and the dissipation of temperature fluctuations, ϵ_θ. In Fig. 5.6, all the contributing terms to the FTV budget, normalized by ${u_\tau^*}^2{\theta_\tau^*}^2/\nu^*$, are shown for the neutrally-buoyant case (open symbols) and for all of the stratified cases (filled symbols).

As it can be observed from, production and dissipation of temperature fluctuations (P_θ and ϵ_θ, respectively) are the most significant terms of FTV budget over the domain for the neutrally-buoyant case. In neutrally buoyant condition, the turbulent and molecular diffusion of temperature fluctuations only redistribute temperature fluctuations in the near-wall region. In this case, the temperature fluctuations are in equilibrium outside the near-wall region, because production and dissipation are locally in balance [67]. Similar behavior of FTV is also observed by Alcántara-Ávila et al. [1], Kasagi et al. [51], Lyons et al. [67] and Krishnamoorthy & Antonia [56]. In stably stratified conditions, a notable increase in production and dissipation is observed throughout the entire domain. The increase in the mean temperature gradient (by increasing the strength of stratification) reflects in to a increase of production, which still balances the dissipation [46]. The peak location of temperature fluctuations (channel center) production refers to the region where buoyancy dominates. In general, the turbulent diffusion term transfers the temperature fluctuations from the core region of the channel to the near-wall region. On the other hand, molecular diffusion shows an interesting behavior very close to the channel center. In this narrow region, molecular diffusion shows a negative mean value for a weak stratification ($Ri_\tau = 50$ and 100), but a positive mean value for the moderate stratified cases ($Ri_\tau = 200$ and 300). The peak amplitude in the turbulent diffusion shows that the two weaker stratified cases transfer more energy in the form of turbulent diffusion compared to the other two more strongly stratified cases (where turbulence is almost completely suppressed) at the channel center.

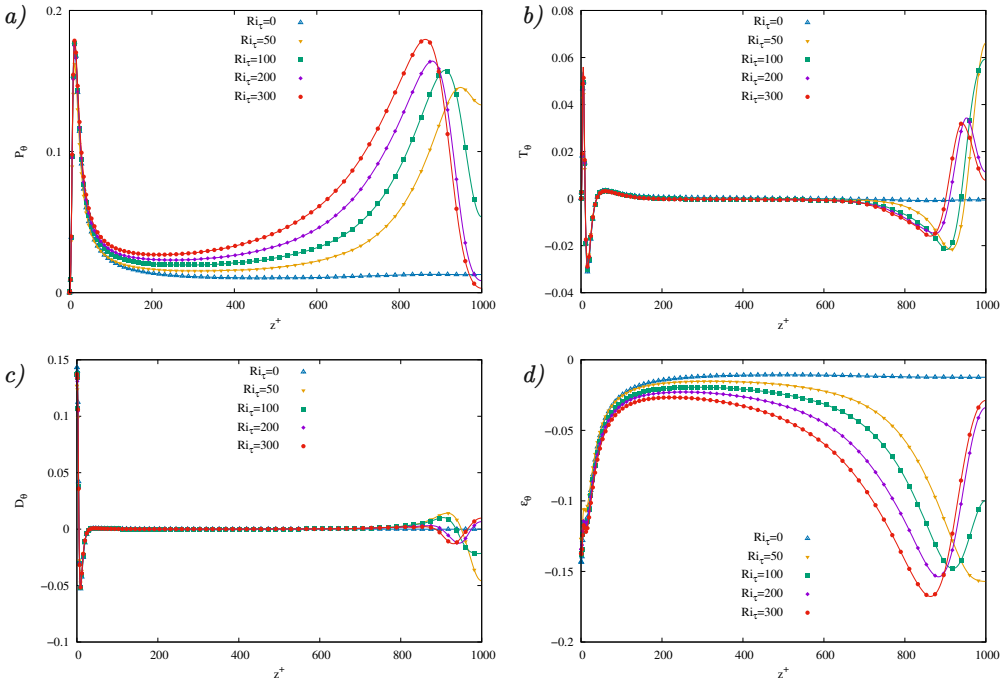

FIGURE 5.6 – FTV budget terms for $Ri_\tau = 0, 50, 100, 200$ and 300, panel a) Production of turbulent fluctuating temperature, panel b) Turbulent diffusion of temperature fluctuations, panel c) Molecular diffusion of temperature fluctuations d) Dissipation of temperature fluctuations.

5.1.4 Mean temperature variance (MTV) budget

To obtain the MTV $= \frac{1}{2}\langle\theta\rangle\langle\theta\rangle$ budget equation, the Reynolds-decomposed energy equations is multiplied by the mean temperature field $\langle\theta\rangle$, and an ensemble averaging is taken. The MTV budget equation in dimensionless form is given as

$$\frac{D[MTV]}{Dt} = \underbrace{\left[\langle u_j'\theta'\rangle\frac{\partial\langle\theta\rangle}{\partial x_j}\right]}_{\widetilde{P_\theta}} + \underbrace{\left[-\frac{\partial\left(\langle u_j'\theta'\rangle\langle\theta\rangle\right)}{\partial x_j}\right]}_{\widetilde{T_\theta}} + \underbrace{\left[\frac{1}{2Re_\tau Pr}\frac{\partial^2\langle\theta\rangle^2}{\partial x_j^2}\right]}_{\widetilde{D_\theta}} + \underbrace{\left[-\frac{1}{Re_\tau Pr}\left\langle\frac{\partial\langle\theta\rangle}{\partial x_j}\frac{\partial\langle\theta\rangle}{\partial x_j}\right\rangle\right]}_{\widetilde{\epsilon_\theta}} \tag{5.4}$$

The first term on the right-hand side of Eq. 5.4 represents the production of mean temperature variance, $\widetilde{P_\theta}$. This term acts as a sink term in MTV budget, whereas it is a source term in FTV ($P_\theta = -\widetilde{P_\theta}$). The second term is turbulent diffusion of the mean temperature variance, $\widetilde{T_\theta}$. Third and fourth terms are the molecular diffusion of mean temperature variance, $\widetilde{D_\theta}$ and dissipation of mean temperature variance, $\widetilde{\epsilon_\theta}$,

respectively. In Fig. 5.7, all the right-hand side terms of Eq. 5.4, normalized by $u_\tau^{*2}\theta_\tau^{*2}/\nu$, are shown for neutrally-buoyant case (open symbols) and all the stratified cases (filled symbols).

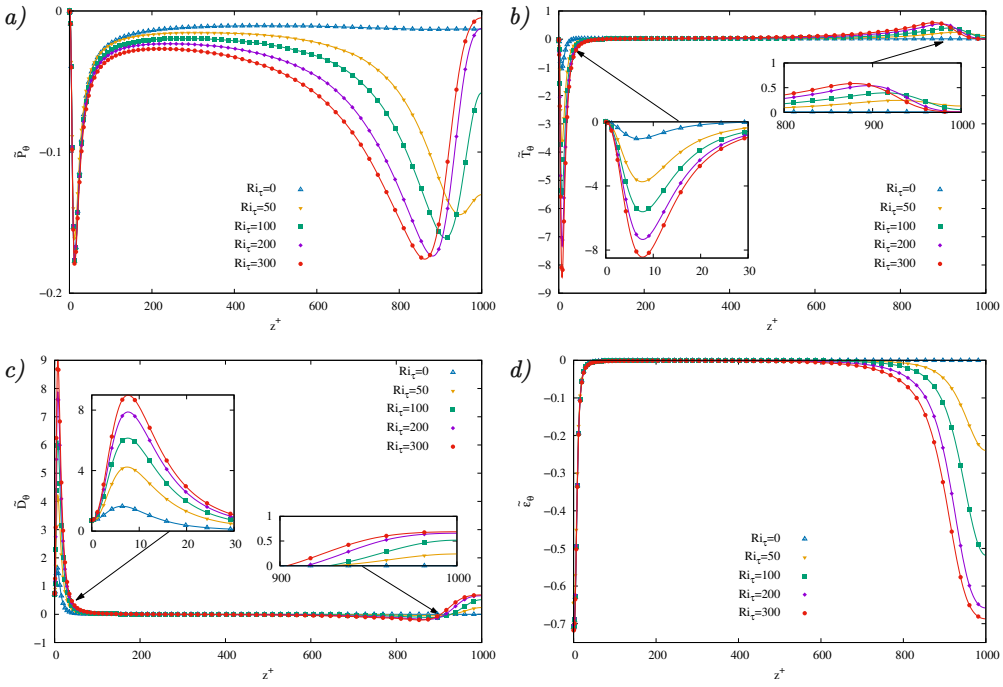

FIGURE 5.7 – MTV budget terms for $Ri_\tau = 0, 50, 100, 200$ and 300, panel a) Production of mean temperature variance, panel b) Turbulent diffusion of mean temperature variance, panel c) Molecular diffusion of mean temperature variance d) Dissipation of mean temperature variance.

The only source of MTV in the near-wall region is the molecular diffusion of MTV. As shown in Fig. 5.7, the molecular diffusion is primarily affected by stratification in the viscous wall region. The larger the stratification strength, the stronger the molecular diffusion in the near-wall region. Both molecular and turbulent diffusion are the most important mechanisms in transferring MTV in the near-wall region. By departing from the wall toward the channel center, the stratification shows its largest influence at the core region of the channel, where both molecular and turbulent diffusion of MTV are source terms and the production and the dissipation of MTV act as sinks. It is worth to mention, that the turbulent diffusion of MTV becomes a source term at the core region of the channel under the stratification effect, whereas this term acts as the main sink in the near-wall region.

5.1.5 Total potential energy (TPE) budget

As discussed in Sec. 5.1.1, the buoyancy flux , Φ_z, in TKE budget is the only term, which exchanges mechanical energy between the kinetic and potential energy. To

derive the budget equation of the TPE of the system, we use the classical definition of the TPE (see Winters et al. [131]). The specific gravitational potential energy of the system with volume V is defined as

$$TPE = \left(\frac{g^*}{\rho_0^* V^*}\right) \int_{V^*} \rho^* z^* dV^* = \left(\frac{g^*}{\rho_0^*}\right) \langle \rho^* z^* \rangle_V \tag{5.5}$$

where $\langle . \rangle_V$ indicates the volume average quantity. Recalling the linear equation of state for an incompressible and Boussinesq fluid (see subsection 2.1.4) and given the fact that there is no net potential energy associated with the fluctuating component of the density [41], the evolution equation of TPE can be written as

$$TPE = g^* \beta^* \left\langle \langle \theta^* \rangle z^* \right\rangle_V \tag{5.6}$$

To obtain the TPE budget equation, the Reynolds-decomposed energy equation is substituted into Eq. 5.6 to give (in dimensionless form)

$$\frac{D[TPE]}{Dt} = \underbrace{[Ri_\tau \langle u_z' \theta' \rangle_V]}_{\overline{\Phi}_z} + \underbrace{\left[-\frac{Ri_\tau}{Re_\tau Pr} \left\langle \frac{\partial \langle \theta \rangle}{\partial z} \right\rangle_V\right]}_{\overline{\Phi}_i} + \underbrace{\left[\frac{Ri_\tau}{Re_\tau Pr} \frac{\partial \langle \theta \rangle}{\partial z} \Big|_w\right]}_{\overline{\Phi}_b} \tag{5.7}$$

In Eq. 5.7, the first term on the left-hand side, $\overline{\Phi}_z$ is the buoyancy flux. This term is a sink term in TKE budget, whereas it is a source of energy in TPE. The second term, $\overline{\Phi}_i$, represents the rate at which total potential energy increases due to vertical redistribution resulting from molecular diffusion (conversion rate from internal energy, IE, to potential energy) [122]. The term ,$\overline{\Phi}_i$, can be seen as the rate at which the center of mass of the volume would be raised or lowered as a result of molecular diffusion of the stratifying scalar if there was no fluid motion [42]. The third term, $\overline{\Phi}_b$ is the rate of diffusive buoyancy flux across the surface. A clear description of the different processes, namely "mixing" and "stirring", by which the potential energy of the system can be increased via fluid motions is presented by Peltier & Caulfield [83]. The key point is to separate the increase of potential energy of the system via $\overline{\Phi}_i$ from mixing. In general, it is very difficult to ascertain that the averaging procedure produces an estimate free from contamination by adiabatic processes in stratified turbulent flows with IGWs. in consequence, an spatial and long-time averaging is required [131]. Therefore, the instantaneous values of the $\overline{\Phi}_z$ can be very misleading for measuring the mixing. The average quantities in Eq. 5.7, in combination with the volume integral of TKE and MKE can provide an accurate description of the mechanical energy transfer in the stably-stratified turbulent channel flow. The energy exchange between different energy reservoirs has been broadly investigated in archival literature. The mechanical energy exchange between MKE, TKE and TPE is studied for the global ocean circulation [41], horizontal convection [30] and Rayleigh-Bénard convection [31], extensively. A similar framework has been also employed to study the mechanical energy budget and mixing efficiency of the ice-covered freshwater basins heated by solar radiation by Ulloa et al. [122]. Howland et al. [40], presented the energy pathways in a triply periodic domain with external forcing on the velocity and density fields. Scotti and White [101] studied the energy transfer between MKE, TKE and TPE for stratified rotating

flows. The mechanical energy pathways has benn also studied by Kirkpatrick et al. [53] for a stratified open turbulent channel flow after removal of a volumetric heat source. A physically sound approach to investigate the irreversible mixing in stratified turbulence is to separate the available potential energy from the background potential energy. Although, this will be the subject of a future investigation, we measure the irreversible mixing using a simplified approach for stably-stratified turbulent flows in the following section.

5.2 Mixing in thermally stratified turbulence

Evaluation of irreversible vertical turbulent mixing of momentum and density when turbulence interacts with buoyancy forces that do depend on local density gradients is very complex and challenging. Precise quantification of irreversible mixing of momentum and density/temperature is crucial for many practical applications such as air quality prediction in the atmospheric boundary layer and prediction of heat fluxes and circulation in oceanic flows [127]. To evaluate vertical mixing in turbulent stratified flows, it is common practice to relay on the concept of turbulent eddy viscosity and diffusivity [88]. Based on the gradient-transport hypothesis [88], the turbulent eddy viscosity K_m and diffusivity K_ρ in a unidirectional shear flow are given as

$$K_m = -\frac{\langle u_x' u_z' \rangle}{\frac{\partial \langle u_x \rangle}{\partial z}}, \qquad K_\rho = -\frac{\langle \theta' u_z' \rangle}{\frac{\partial \langle \theta \rangle}{\partial z}} \tag{5.8}$$

In general K_m and K_ρ can be estimated either directly or indirectly. For a direct estimation of these two quantities, it is crucial to calculate the turbulent fluxes and mean gradients from measurements [66]. The concept of mixing-length was introduced by Taylor [113] for the first time and Prandtl [89] used this concept to define K_ρ, as it is defined in Eq. 5.8 (Prandtl mixing length model). The ratio between K_m and K_ρ is usually referred to as turbulent Prandtl number [58], and can be written in dimensionless form as

$$Pr_T = \frac{\langle u_x' u_z' \rangle \frac{\partial \langle \theta \rangle}{\partial z}}{\langle u_z' \theta' \rangle \frac{\langle u_x \rangle}{\partial z}} \tag{5.9}$$

Quantification of Pr_T as a function of stratification strength (here Ri_τ) is a crucial subject in the field of turbulence modeling [126, 33]. Pr_T is shown in Fig. 5.8 as a function of dimensionless wall-normal direction (panel a) and Ri_g (panel b). It can be seen from Fig. 5.8-a that in the near-wall region, Pr_T remains unaffected by stratification and in the region below $z \approx 0.7$, the turbulent Prandtl number varies only slightly. As also pointed out by García-Villalba & del Álamo [28], above this region, Pr_T shows a significant variation and a Ri_τ dependence of Pr_T can not be observed clearly. In Fig. 5.8-b, the turbulent Prandtl number is represented as a function of Ri_g for different shear Richardson numbers. It seems that the assumption of $Pr_T \approx 1$, customarily taken in turbulence modeling, is reasonable for $Ri_g \leq 0.2$ only, however for $Ri_g \geq 0.2$, where the stratification starts to leave its footprint on the flow dynamic, such an assumption is not correct.

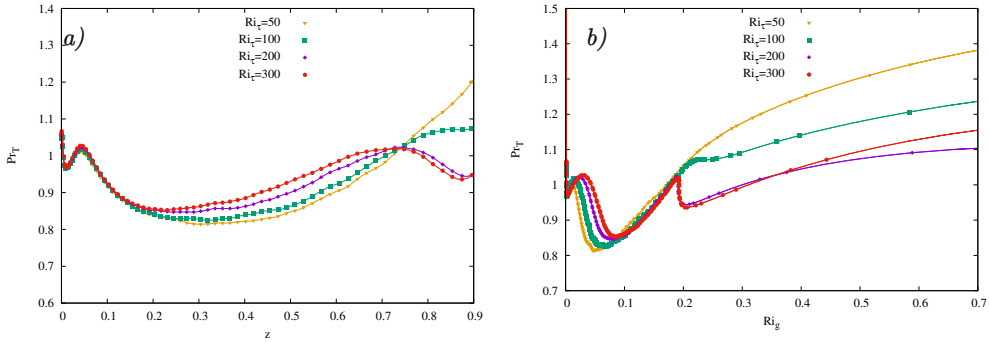

FIGURE 5.8 – Turbulent Prandtl number as a function of, a) dimensionless wall-normal direction and panel b) gradient Richardson number.

The definition of K_m and K_ρ as in Eq. 5.8 is the the simplest approach, but it hides some issues. Due to the coexistence of turbulence and IGWs, direct estimation of heat and momentum fluxes is challenging even if the flow field is highly resolved. The issue arises because IGWs have almost no contribution to irreversible mixing and the separation of flux contribution from IGWs and turbulence is still problematic. Therefore, a number of indirect methods for estimation of fluxes has been proposed. A common assumption of these methods is that the turbulent flow is statistically stationary in time and homogeneous in space. Osborn & Cox [81] based their model on a simplified FTV budget equation, which is then used to give an approximate expression for buoyancy flux, Φ_z. For temperature stratified flows, as the flow configuration studied throughout this thesis, it is usually assumed that $K_\theta = K_\rho$ [96]. Osborn & Cox model [81] results into the definition of K_θ in dimensionless form [35]

$$K_\theta = \frac{\langle \overline{|\nabla\theta'|^2} \rangle}{\left\langle \left[\frac{d\langle\theta\rangle}{dz} \right]^2 \right\rangle} . \tag{5.10}$$

The expression on the right-hand side of Eq. 5.10 is usually called Cox number. Osborn [80] employed a different approach to estimate K_ρ. By simplifying the TKE balance equation, a three-way balance between production of TKE, buoyancy flux and turbulent viscous dissipation can be obtained. Osborn model [80] estimates the vertical eddy diffusivity of density in dimensionless form as

$$K_\rho = \left(\frac{Ri_f}{1 - Ri_f} \right) \frac{\epsilon_k}{N^2} , \tag{5.11}$$

where Ri_f is the flux Richardson number, and can be defined as

$$Ri_f = \frac{\Phi_z}{P_k}. \tag{5.12}$$

Ri_f represents the ratio of buoyant destruction to shear production in the turbulent kinetic energy equation [28]. The definition of Pr_T, presented in Eq. 5.9 can be

rewritten as $Pr_T = Ri_g/Ri_f$. In Fig. 5.9, the flux Richardson number is shown as a function of gradient Richardson number. For $Ri_g < 0.2$, the profiles collapse on the solid black line $Ri_g = Ri_f$, meaning that when Ri_g is below its critical value, Pr_T does not vary significantly with Ri_g. A similar behavior was also found by García-Villalba & del Álamo [28]. This collapse is lost for higher values of Ri_g.

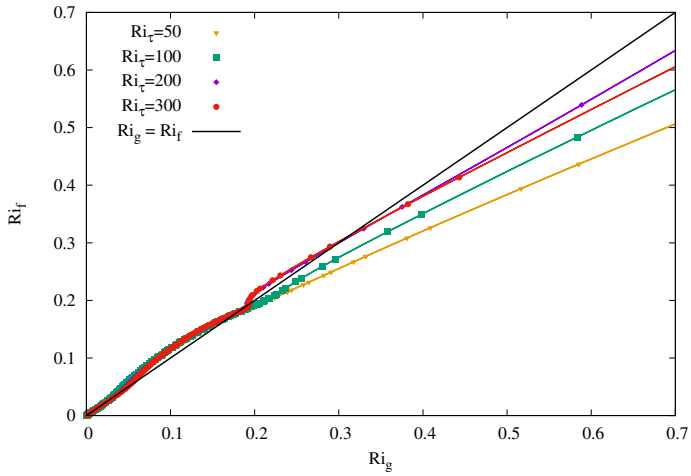

FIGURE 5.9 – Ri_f as a function of gradient Richardson number for different Ri_τ.

Reportedly, Ri_f has been used in literature to introduce $\Gamma = Ri_f/(1 - Ri_f)$, which is sometimes referred to as the mixing efficiency. Based on theoretical analysis of Ellison [20] and the experiments of Britter [13], Osborn [80] assumed a constant value of $Ri_f = 0.17$, which ultimately lead to $\Gamma = 0.2$. To evaluate the sensitivity of the assumption made by Osborn [80], a series of studies has been performed [35, 95, 22, 48, 47, 83, 49, 103].

More recently, Ivey & Imberger [48] tried to overcome the limitation associated to the assumption that the flow is steady in time and homologous in space by taking the inhomogeneous and unsteady transport terms in the TKE balance equation into account, and proposed an alternative definition of flux Richardson number as

$$Ri_f^{II} = \frac{\Phi_z}{\Phi_z + \epsilon_k} \tag{5.13}$$

Although the Ri_f^{II} definition of Ivey & Imberger [48] does not require the assumption of homogeneity and steadiness of the turbulent flow, it is still influenced by the effect of countergradient fluxes that are common in more strongly stratified flows [127].

To solve this issue, Peltier & Caulfield [83] gave a proper definition of the mixing in stably-stratified turbulence by taking only the irreversible conversions of energy locally into account. Hence, following the approach demonstrated by Venayagamoorthy & Stretch [126], a third definition of flux Richardson number can be defined as

$$Ri_f^* = \frac{\epsilon_{PE}}{\epsilon_{PE} + \epsilon_k} \tag{5.14}$$

Where ϵ_{PE} is the dissipation rate of turbulent (available) potential energy and is defined as

$$\epsilon_{PE} = N^2 \epsilon_\theta \left(\frac{d\langle\rho\rangle}{dz} \right)^{-2} \tag{5.15}$$

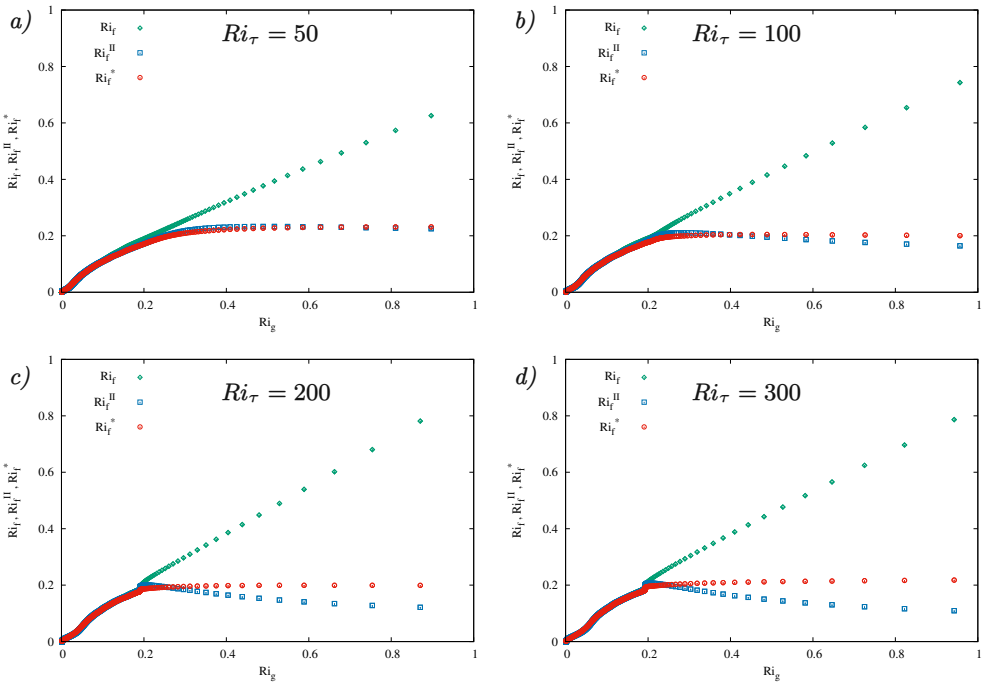

FIGURE 5.10 – Comparison of Ri_f, Ri_f^{II} and Ri_f^* as a function of Ri_g for different shear Richardson numbers.

Note that in case of stationary andhomogeneous flows all the three difinitions of flux Richardson are equal ($Ri_f = Ri_f^{II} = Ri_f^*$). Recently, Venayagamoorthy & Koseff [127] carried out an extensive study of the differences and similarities between the three definitions of the flux Richardson number defined in Eqs. 5.12, 5.13 and 5.14. They used the dataset from the DNS study of homogeneous shear flows by Shih et al. [103] and the stably stratified turbulent channel flow DNS dataset of García-Villalba & del Álamo [28], which is up to $Re_\tau = 550$ to examine the behavior of Ri_f, Ri_f^{II} and Ri_f^*. However, the validity of these results at higher Reynolds numbers is still an open question [127]. Here we examine the sensitivity of the proposed results by Venayagamoorthy & Koseff [127] for $Re_\tau = 1000$. In Fig .5.10, we show Ri_f, Ri_f^{II} and Ri_f^* as a function of Ri_g for all of the stratified cases. In the region, where Ri_g

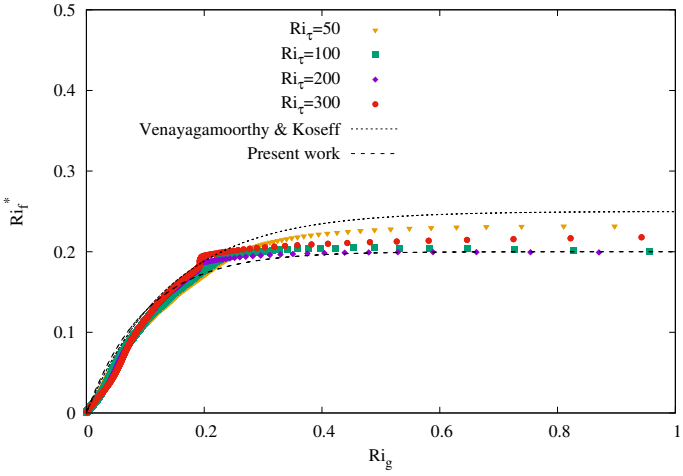

FIGURE 5.11 – The irreversible flux Richardson number Ri_f^* as a function of Ri_g for different Ri_τ. Both dashed lines show the fit given by Eq. 5.16 with different choice of $Ri_{f\infty}^*$ and γ.

is below ≈ 0.2, all the three definition collapse on top of each other, and the flux Richardson number is a linear function of Ri_g, no matter which definition of the flux Richardson number is taken. This suggests that, here shear is playing a dominant role, any of the three definitions of flux Richardson number can be employed for evaluating the irreversible mixing in stably-stratified turbulent flows. Although Ri_f, Ri_f^{II} and Ri_f^* have a good agreement for $Ri_g < 0.2$, they do not follow a similar trend at higher Ri_g. It can be seen that for all of the stratification levels ($Ri_\tau = 50$, 100, 200 and 300) that we have simulated, Ri_f and Ri_f^{II} show a clear variability for $Ri_g > 0.2$, whereas Ri_f^* exhibit approximately a negligible variability in this regime. The physical mechanism behind the variability of Ri_f and Ri_f^{II} is different. The variability of Ri_f for $Ri_g > 0.2$, is due to the fact that both fluxes (heat and momentum) vary in time and space. However, the variation of Ri_f^{II} for $Ri_g > 0.2$ is only caused by the variation of of buoyancy flux. In addition, since the production of TKE becomes small at the core region of the channel (the mean shear rate decreases), the standard definition of Ri_f given in Eq. 5.12 loses its significance. Unlike Ri_f, Ri_f^{II} appears to decrease for $Ri_g > 0.2$. However, the definition of Ri_f^{II} is also weak at higher Ri_g values when strong enough countergradient buoyancy fluxes become important. We can speculate that, where the footprint of reversible effects caused by IGWs are apparent (core region of the channel), the buoyancy flux is contaminated and therefore it can not be considered as a good measure for the mixing. By contrast, the irreversible flux Richardson Ri_f^* is not influenced by the same limitations, since it extracts the impacts of reversible contributions by definition and tends to an approximate constant at higher Ri_g.

Interestingly, Karimpour & Venayagamoorthy [50], building on top of the work by Mellor & Yamada [69], found that the behavior of Ri_f^* as a function of Ri_g can be

modeled as an exponential function:

$$Ri_f^* = Ri_{f\infty}^* \left[1 - e^{(-\gamma Ri_f)}\right] \tag{5.16}$$

where $Ri_{f\infty}^*$ and γ are constants. Venayagamoorthy & Koseff [127] examined this exponential fit against the DNS data of Shih et al. [103] by setting $Ri_{f\infty}^* = 0.25$ and $\gamma = 7$, and found a good agreement between the proposed fit and the DNS data of Shih et al. [103]. However, the proposed fit was not tested for a fully-developed wall bounded flow. We found that, by choosing different $Ri_{f\infty}^*$ and γ, the fit shows a better agreement with our dataset for a fully-developed wall-bounded turbulent flow at $Re_\tau = 1000$. By setting $Ri_{f\infty}^* = 0.2$ and $\gamma = 10$, we are able to capture the asymptotic behavior of Ri_f^* at higher Ri_g very well (see Fig. 5.11).
The better performance of the new parameterization could be due to the effect of wall on the irreversible flux Richardson number Ri_f^*, which is not taken into account in the parameterization proposed by Venayagamoorthy & Koseff [127].

6

Shear effects on double diffusive convection

The content of this chapter was recently published in:

P. Hadi Sichani, C. Marchioli, F. Zonta, and A. Soldati, *Shear effects on scalar transport in double diffusive convection*, ASME J. Fluids Eng. 142:121105, 2020. [36]

In the chapter, we investigate the problem of DDC under the effect of shear, which introduces a symmetry breaking effect into the flow. We also quantify the scalar fluxes and the relative importance of their diffusive and convective parts. To this aim, we perform fully-resolved three-dimensional simulations of double diffusive convection within a fluid layer bounded by a solid (no-slip) wall at the bottom and a slip surface at the top by solving the dimensionless set of conservation equations (Eqs. 2.22-2.25), introduced in subsection 2.2.1. The application of a shear is realized by imposing a mean horizontal velocity u_m^* at the top boundary, and a no-slip condition at the bottom boundary. More specifically, at the top boundary, we impose that both mean and fluctuating components of the wall-normal fluid velocity are zero (no penetration through the upper slip surface), but we allow fluctuations of the streamwise and spanwise velocities, thus ensuring mass conservation. Note that, for the horizontal velocity components, only the mean value is imposed (equal to the applied shear velocity in the streamwise direction and to zero in the spanwise direction). Periodicity is applied for all variables along the homogeneous directions x and y. Present simulations are run at $Ra_s = 10^7$, $\Lambda = 1$, $Pr_\theta = 7$, $Pr_s = 700$, which yield $Le = 100$ and from Eq. 2.38, $\Gamma_d \simeq 23.5\Gamma$. Three different values of the dimensionless shear velocity are chosen: $\Gamma = 0$, $\Gamma = 0.02$ and $\Gamma = 0.1$, corresponding to $\Gamma_d = 0$, $\Gamma_d \simeq 0.47$ and $\Gamma_d \simeq 2.35$ respectively. The domain, whose dimensions are $4\pi h^* \times 2\pi h^* \times 2h^*$, is longer in the streamwise direction to cope with the applied shear. The spatial grid is composed by $1024 \times 512 \times 513$ nodes along x,y and z, respectively, and has been chosen to capture the thin salinity boundary layers. Validation of the grid resolution is provided in Appendix C. All the simulations start from a zero-velocity (hydrostatic) initial condition. At the beginning of the simulation, salinity has a uniform distribution equal to $(s_t + s_b)/2$, while temperature is distributed linearly across the fluid layer (between

the values θ_t and θ_b). The same initial conditions were chosen by Yang et al. [135], which are in turn similar to those considered in the experiments by Hage & Tilgner [37] and by Kellner & Tilgner [52] for the zero-shear case. Note that small random perturbations of both the salinity and the temperature fields have been applied to accelerate the flow development over time.
In the following section, the results of the numerical simulations are presented and discussed. The structure of the flow is first analyzed from a qualitative viewpoint in section 6.1 and then from a quantitative viewpoint described by statistical moments in section 6.2 and transport fluxes in section 6.3. Although statistics have been computed for all three values of Γ, the effects of shear we wish to discuss are magnified for the case with $\Gamma = 0.1$. For this reason, in the following we will show results at $\Gamma = 0.02$ only when they add to the discussion.

6.1 Phenomenology of DDC fingering

We start our analysis by looking at the instantaneous flow structure. A three dimensional rendering of salinity isosurfaces, and the associated two dimensional maps of salinity contours are shown in Fig. 6.1 for $\Gamma = 0$ (left column: panels a-b-c-d) and for $\Gamma = 0.1$ (right column: panels e-f-g-h). The flow structure for $\Gamma = 0.02$ (not shown in the figure) exhibits an intermediate behavior between those shown. Salinity contours are measured on horizontal slices located at $z \equiv z^*/h^* = -0.95$, $z = 0$ and $z = 0.95$, respectively. We look first on the zero-shear case, and we focus on panel a). Thin salt fingers of heavy and light fluid are emitted from the top and bottom boundary, travel over the entire vertical extension of the fluid layer and reach the opposite boundary. The shape and the distribution pattern of these fingers is such that heavy and light fingers come one after the other and define the boundaries of adjacent and vertically-elongated convection cells. The qualitative structure of the flow is similar to that observed in the classical configuration with two no-slip boundaries [132, 135] although the different boundary conditions prescribed here (slip conditions at the top, and no-slip conditions at the bottom) induce a slight asymmetry, with fingers emerging from the top boundary being a bit stronger than those emerging from the bottom boundary. The main reason for this asymmetry is that all components of the fluid velocity must go to zero at the bottom boundary, while horizontal motions are possible at the top boundary where only vertical motions are forbidden (vertical geometrical constraint). As a consequence, the flow recirculation close to the upper portion of the fluid layer is stronger compared to that occurring in the lower portion of the layer [134]. To analyze the organized flow structure of salt fingers more closely, we focus now on the two-dimensional contour maps of salinity in Figs. 6.1b-c-d. Near the top and bottom boundaries (Fig.6.1b-d) we observe the presence of thin branches (sheet-like structures) characterized by different orientations and connected in such a way that they form a regular network of polygonal-shape cells. At the bottom boundary (Fig. 6.1b), these thin branches are characterized by low salinity (rendered as blue isocontours). Intense blue spots appear at the intersection between neighbouring branches, and represent the root of light fingers that move vertically upwards. At the same time, dense fingers (rendered as red regions of salty fluid in Fig. 6.1) move close to the bottom boundary to replace the fluid transported away by upward-moving fingers

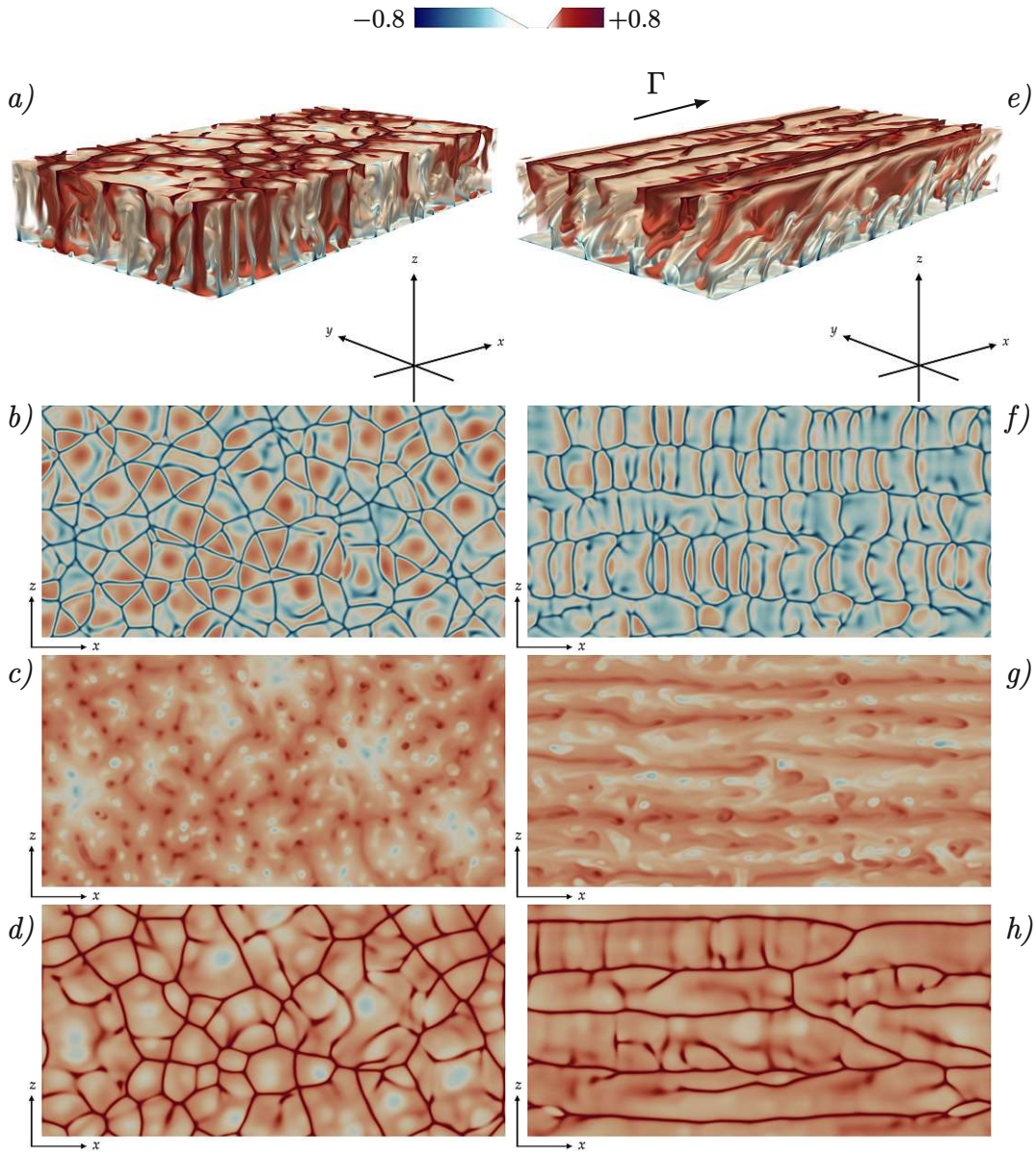

FIGURE 6.1 – Three-dimensional volume rendering, and associated two-dimensional maps, of salinity distribution for $\Gamma = 0$ (panels a,b,c,d) and $\Gamma = 0.1$ (panels e,f,g,h). Two dimensional maps are measured at $z = -0.95$ (i.e. close to the bottom boundary, panels b and f), $z = 0$ (i.e. at the cell center, panels c and g) and $z = 0.95$ (i.e. close to the top boundary, panels d and h). For all panels, the same colormap but different opacity settings are used, with red indicating high-salinity (dense) fluid, and blue indicating low-salinity (light) fluid. An opacity filter is used for the volume rendering, whereas a standard sequential colormap is used for the two-dimensional maps.

(fluid eruptions). Since temperature diffusion mechanisms are almost three orders of magnitude faster than salinity diffusion mechanisms, temperature horizontal gradients are quickly equalized while fingers travel upward, and the flow field can be considered in thermal equilibrium over horizontal planes. It is therefore solely the salinity difference that produces the buoyancy forces driving the fingers upward. But, since salt convection is in this instance stronger than salt diffusion, such buoyancy forces maintain fingers coherency and drive them across the fluid layer, up to the top boundary. Here the fluid becomes progressively denser and accumulates (red branches connected by red spots) until there is a thick enough layer of dense fluid for a new finger to form. Each finger travels the entire fluid layer and generates a stable *jet* of fluid close to the opposite boundary. Upon impingement with such boundary, fingers are deflected in the horizontal direction and lose their coherence. The deflection of fingers generates a strong divergence of the horizontal velocity field near the boundary, which collects fluid into specific regions (thin branches converging towards spots) from which fingers with opposite buoyancy are emitted. From a $vis - a - vis$ comparison of Fig. 6.1b with Fig. 6.1d we note that the pattern of branches at the bottom boundary is more organized than the one at the top boundary, due to the different boundary condition. Also, the extremely organized pattern of structures observed near the boundaries is replicated at the center of the fluid layer (Fig. 6.1c) in the form of a sequence of alternating fingers (round-shaped structures) of heavy and light fluid, rendered in red and blue respectively.

When the mean shear $\Gamma = 0.1$ is applied at the top wall, the situation changes remarkably. This is visualized in the right column of Fig. 6.1 (panels e-f-g-h). By looking at the 3D maps of salinity (Fig. 6.1e), it is apparent that salt fingers are inclined by the mean shear and lose the strong vertical coherence observed for $\Gamma = 0$ in Fig. 6.1a. This is even more visible by looking at the 2D contour maps of salinity measured at the three different vertical locations (panels f-g-h in Fig. 6.1). Close to the bottom boundary (Fig. 6.1f), we still observe the presence of thin, sheet-like branches, which however form long chains aligned with the direction of the imposed shear. Shorter braids, orthogonal to the direction of shear, connect the different horizontal chains. A similar pattern, though less organized and coherent, is observed close to the top boundary (Fig. 6.1h), and is somehow maintained also at the center of the fluid layer (Fig. 6.1g). This dramatic change of the flow structure will reflect on the corresponding statistics, as discussed in the next section.

6.2 Statistical moments of velocity, temperature and salinity

The profiles of dimensionless salinity, $\langle s(z) \rangle$, temperature, $\langle \theta(z) \rangle$ and axial velocity $\langle u_x(z) \rangle$ are shown in Fig. 6.2 as a function of the distance from the bottom boundary, z, for $\Gamma = 0$ and $\Gamma = 0.1$. Angular brackets indicate averaging in time and over the horizontal $x - y$ plane. Profiles for $\Gamma = 0.02$ are not included since they always fall in between those shown and, therefore, do not add to the discussion. Note that, the axial velocity, shown in Fig. 6.2, is made dimensionless with the free-fall velocity of the fingers ($u = u^*/\sqrt{g^* \beta_s^* h^* (\Delta s^*/2)}$). The time-averaging window, in dimensionless form,

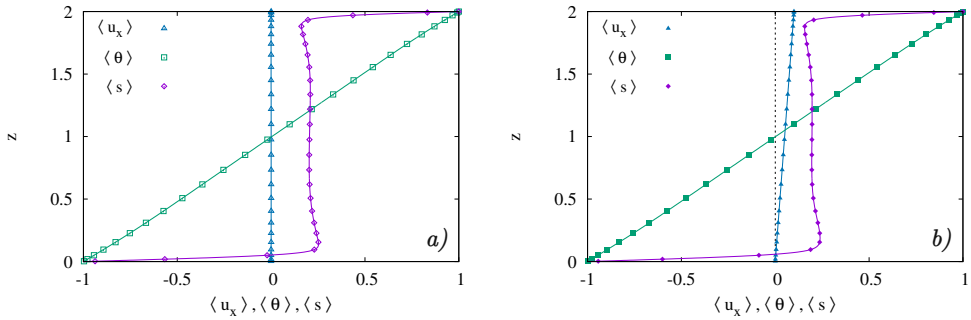

FIGURE 6.2 – Profile of the mean salinity, $\langle s \rangle$, mean temperature, $\langle \theta \rangle$, and mean horizontal velocity, $\langle u_x \rangle$, as a function of the vertical distance from the bottom boundary, z, for $\Gamma = 0$ (panel a) and $\Gamma = 0.1$ (panel b). The vertical dotted line in panel b (zero line) is added for clarity.

is defined as $T_{avg} = T^*_{avg}/(h^*/U^*)$, where T^*_{avg} is the time window in physical units and h^*/U^* is the time scale associated with the free-fall velocity U^*. According to this definition, T_{avg} measures the averaging time window as multiple of the characteristic time taken by the salt fingers to cross the entire fluid layer by free fall. Time averaging of the statistics was performed over statistically-steady flow fields, and therefore, all observables examined in this thesis refer to statistically-steady flow conditions. The convergence toward the steady state condition was monitored by examining the time evolution of several macroscopic observables, such as the Reynolds number and the Nusselt number. An example of such time evolution is shown in Fig. 6.3.

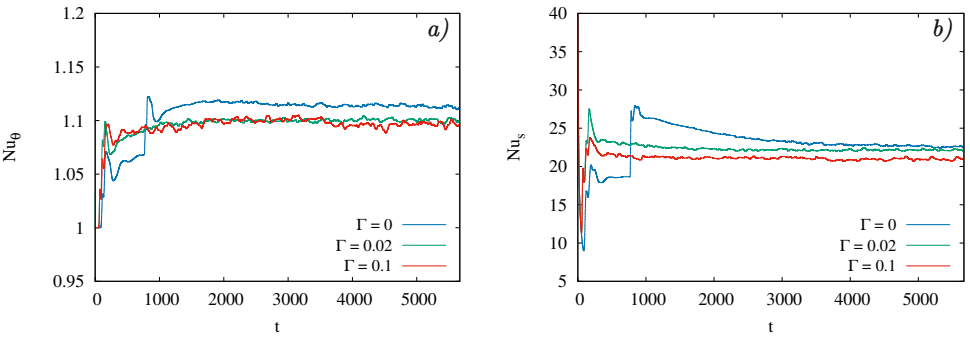

FIGURE 6.3 – Time evolution of heat flux (panel a) and salinity flux (panel b). Note that, time is dimensionless and normalised with respect to h^*/U^*.

The values of T_{avg} considered in each simulation are 2200, 2700 and 3000 for $\Gamma = 0$, $\Gamma = 0.02$ and $\Gamma = 0.1$, respectively. We consider first the case $\Gamma = 0$ (Fig. 6.2a). As expected, we find that $\langle u_x(z) \rangle = 0$. Also expected is the linear profile of the mean temperature, $\langle \theta(z) \rangle$, which is typical of a diffusion-dominated process: This is clearly the case of temperature, which has a large diffusion coefficient and diffuses very efficiently. What is non-trivial is the behavior of the mean salinity $\langle s(z) \rangle$. First,

$\langle s(z) \rangle$ is not symmetric, due to the asymmetric velocity boundary conditions. We also notice that the mean salinity changes very rapidly close to the boundaries. This marks the presence of two thin boundary layers, which however seem to differ in thickness: Due to the different boundary conditions, the bottom boundary layer seems thicker than the top one. A more quantitative evaluation of the boundary layer thickness will be given below, based on the behavior of the salinity fluctuations. In the core region of the fluid layer, for $0.5 < z < 1.5$, the mean salinity is almost constant and equal to $\langle s \rangle \simeq 0.15$. Interestingly, the profile of the mean salinity is non-monotonic and develops a local minimum in the region $1.5 < z < 2$ as well as a local maximum in the region $0 < z < 0.5$. This non-monotonic behavior has important consequences for the global heat and salinity transfer rates, which will be discussed in Sec. 6.3. Considering the $\Gamma = 0.1$ case, the global picture does not change much compared to the $\Gamma = 0$ case (in particular for $\langle s \rangle$ and $\langle \theta \rangle$), the only obvious difference being the profile of the mean horizontal velocity, which exhibits a linear behavior between the values $\langle u_x \rangle = 0$ at the bottom wall and $\langle u_x \rangle = 0.1$ at the top wall.

To understand further the different salinity and temperature distributions induced by shear, we look at the behavior of the root mean square of their fluctuations, $\langle \theta_{rms} \rangle$ and $\langle s_{rms} \rangle$. Results are presented in Fig. 6.4. Open symbols refer to the case $\Gamma = 0$, while filled symbols refer to the case $\Gamma = 0.1$. Again, curves for $\Gamma = 0.02$ are not included as they would fall in between those shown in the figure. Differences in the horizontal and vertical components of the velocity field are also not shown because they are rather small and hence negligible. Fluctuations of temperature (Fig. 6.4a) are relatively small and reach their maximum value ($\simeq 9\%$ of the temperature at the boundary) at the center of the fluid layer. The action of a mean shear does not modify qualitatively the shape of the profile, but induces a general attenuation of the fluctuations ($\simeq 6\%$ of the temperature at the boundary). Focusing on the salinity fluctuations (Fig. 6.4b), we note that, regardless of the value of Γ, they are much larger than temperature fluctuations, and reach a maximum very close to the boundary ($\simeq 25\%$ of the salinity at the boundary). It is interesting to note that there is a slight asymmetry in the profile of $\langle s_{rms} \rangle$ for both values of Γ, with salinity fluctuations being larger close to the bottom boundary. The action of a mean shear induces a general reduction of

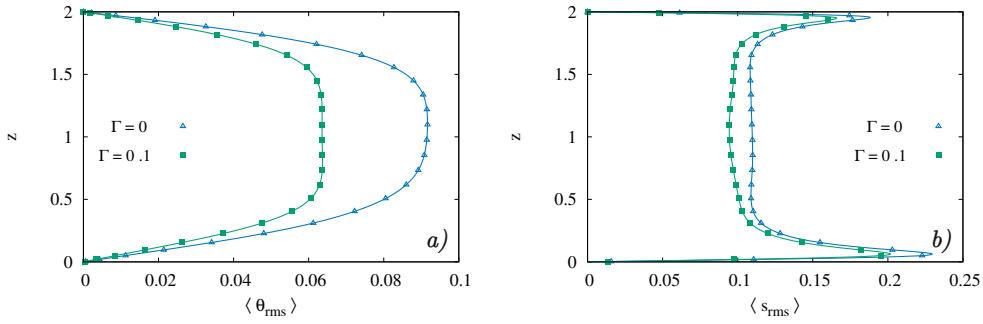

FIGURE 6.4 – Profile of the root mean square of temperature fluctuations, $\langle \theta_{rms} \rangle$ (panel a), and of salinity fluctuations, $\langle s_{rms} \rangle$ (panel b), as a function of the vertical distance from the bottom boundary, z, for $\Gamma = 0$ and $\Gamma = 0.1$, respectively.

solute fluctuations, but does not change qualitatively the shape of the profile. The location at which fluctuations peak is used to estimate the thickness $\lambda \equiv \lambda^*/h^*$ of the boundary layer. For $\Gamma = 0$, $\lambda = 3.133 \times 10^{-2}$ at the bottom wall and $\lambda = 2.243 \times 10^{-2}$ at the top wall, while for $\Gamma = 0.1$ we have again $\lambda = 3.133 \times 10^{-2}$ at the bottom wall but $\lambda = 2.523 \times 10^{-2}$ at the top wall. The slight increase of the boundary layer thickness at the top wall resulting from the application of the mean shear indicates a weaker vertical salinity transport, as will be discussed below.

6.3 Heat and salinity flux

The different flow behavior induced by shear at the top boundary is expected to influence also the transport rates of heat and salinity. The total heat and salinity fluxes are:

$$q_\theta = \left(\frac{1}{16}\frac{Ra_s Pr_\theta}{Le}\right)^{\frac{1}{2}} \langle u_z \theta \rangle - \frac{\partial \langle \theta \rangle}{\partial z}, \quad q_s = \left(\frac{1}{16} Ra_s Pr_s\right)^{\frac{1}{2}} \langle u_z s \rangle - \frac{\partial \langle s \rangle}{\partial z}, \tag{6.1}$$

and are the sum of a convective contribution (proportional to $\langle u_z \theta \rangle$ and $\langle u_z s \rangle$, respectively) and a diffusive contribution (proportional to $\partial\langle\theta\rangle/\partial z$ and $\partial\langle s\rangle/\partial z$, respectively). The behavior of q_θ and q_s as a function of the vertical coordinate z is shown in Fig. 6.5 and in Fig. 6.6, respectively. We focus first on q_θ (Fig. 6.5), for the case $\Gamma = 0$. The diffusive and convective components of the total flux are shown using different symbols. In addition, to visualize better their behavior, only a portion of the x-axis is shown. It is apparent that the diffusive heat flux is slightly larger than unity close to the boundaries, $\partial\langle\theta\rangle/\partial z \simeq 1.1$, and slightly smaller than unity at the center of the fluid layer, $\partial\langle\theta\rangle/\partial z \simeq 0.97$. Overall, the departure from a purely diffusive profile, which would correspond to $\partial\langle\theta\rangle/\partial z = 1$, is mild. To counterbalance this temperature anomaly, and to give the expected uniform and constant value of q_θ (vertical dashed line $q_\theta \simeq 1.11$), the convective heat flux is maximum, and approximately constant at the center of the fluid layer, $\left(\frac{1}{16}\frac{Ra_s Pr_\theta}{Le}\right)^{\frac{1}{2}} \langle u_z \theta \rangle \simeq 0.15$. The application of the mean shear at the top boundary induces only negligible changes of both $\langle u_z \theta \rangle$ and $\partial\langle\theta\rangle/\partial z$, and gives an overall heat flux that is only 1% lower than that measured for $\Gamma = 0$ for both $\Gamma = 0.02$ and $\Gamma = 0.1$. We turn now to the behavior of the salinity flux q_s (Fig. 6.6), and on its diffusive and convective parts, starting from the case $\Gamma = 0$. The diffusive part $\partial\langle s\rangle/\partial z$, which measures the steepness of the salinity gradient in the vertical direction, is very large close to the boundaries, but drops down abruptly (it is already close to zero at a distance of $\Delta z \simeq 0.1$ from the boundaries. Interestingly, salinity gradients become negative, as shown in the two left-hand insets of Fig. 6.6. A negative diffusive flux indicates the existence of regions of the flow where the local mean salinity gradient is opposite to the imposed one (counter-gradient regions). This may be ascribed to the low diffusivity of salinity, and to the fact that vertical fingers carry their salinity almost unchanged throughout the entire height of the fluid layer. As a consequence, there are regions close to the bottom boundary in which the salinity is that characteristic of the top boundary, and viceversa, thereby inducing the local salinity inversion. The behavior of the convective part of the total flux is complementary to the diffusive one: large values of $\langle u_z s \rangle$ are observed throughout the entire fluid

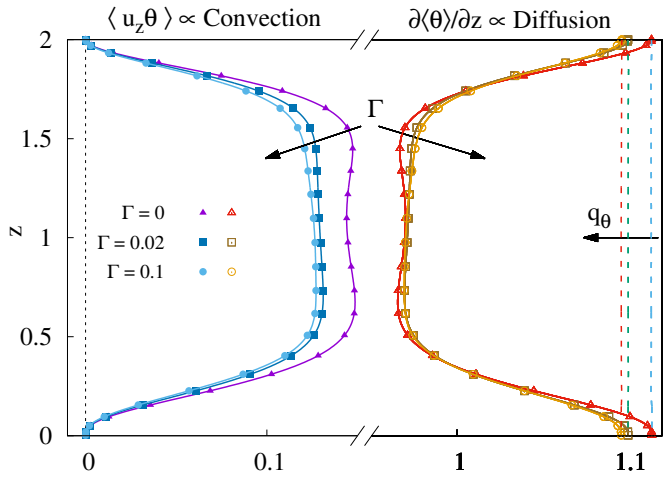

FIGURE 6.5 – Vertical behavior of temperature fluxes as a function of the distance from the bottom boundary, z, for $\Gamma = 0$ (triangles), $\Gamma = 0.02$ (squares) and $\Gamma = 0.1$ (circles). Both the convective part ($\langle u_z\theta\rangle$, lines and filled symbols in blue scale) and the diffusive part ($\partial\langle\theta\rangle/\partial z$, lines and open symbols in red scale) to the total heat flux (q_θ, corresponding to the dashed lines on the right-hand side of the plot) are shown. Note that only a portion of the x-axis is shown to emphasize the shear-induced modifications of the fluxes.

layer but in the region near the boundaries, where the convective part drops to zero. When summed up together, the diffusive and the convective parts give a total salinity flux that is uniform and constant (see vertical dashed line $q_s \simeq 23$). Considering the $\Gamma = 0.02$ and $\Gamma = 0.1$ cases, we immediately observe that, while the diffusive part is almost unaffected by the imposed shear, the convective part is remarkably reduced (although its shape is qualitatively similar). This behavior has of course an influence on the total salinity flux, which becomes smaller (vertical dashed line at $q_s \simeq 22$ for $\Gamma = 0.02$ and $q_s \simeq 21$ for $\Gamma = 0.1$). In dimensionless form, and integrated over the entire domain, the heat and salinity fluxes yield the temperature and salinity Nusselt numbers

$$Nu_\theta = \frac{1}{2}\int_0^2 q_\theta dz\,, \qquad Nu_s = \frac{1}{2}\int_0^2 q_s dz\,, \tag{6.2}$$

which are the most important output parameters (i.e. global responses) of the considered physical systems. In Fig. 6.7 we show the behavior of Nu_s, normalized by its reference value $Nu_{s,0}$ computed at zero shear, as a function of the applied shear rate, indicated as Γ in the bottom horizontal axis and as Γ_d in the top horizontal axis. The values of Nu_s are also explicitly given in the table inside Fig. 6.7, together with the values of Nu_θ, which undergo a negligible change (within 1%) and hence are not directly plotted. We observe that the salinity flux $Nu_s/Nu_{s,0}$ decreases for increasing Γ. For the smallest value of the imposed shear rate, $\Gamma = 0.02$, we measure a decrease of about 3% in the vertical salinity flux. The decrease of Nu_s becomes larger (approximately 10%) in the $\Gamma = 0.1$ case. These important modifications in

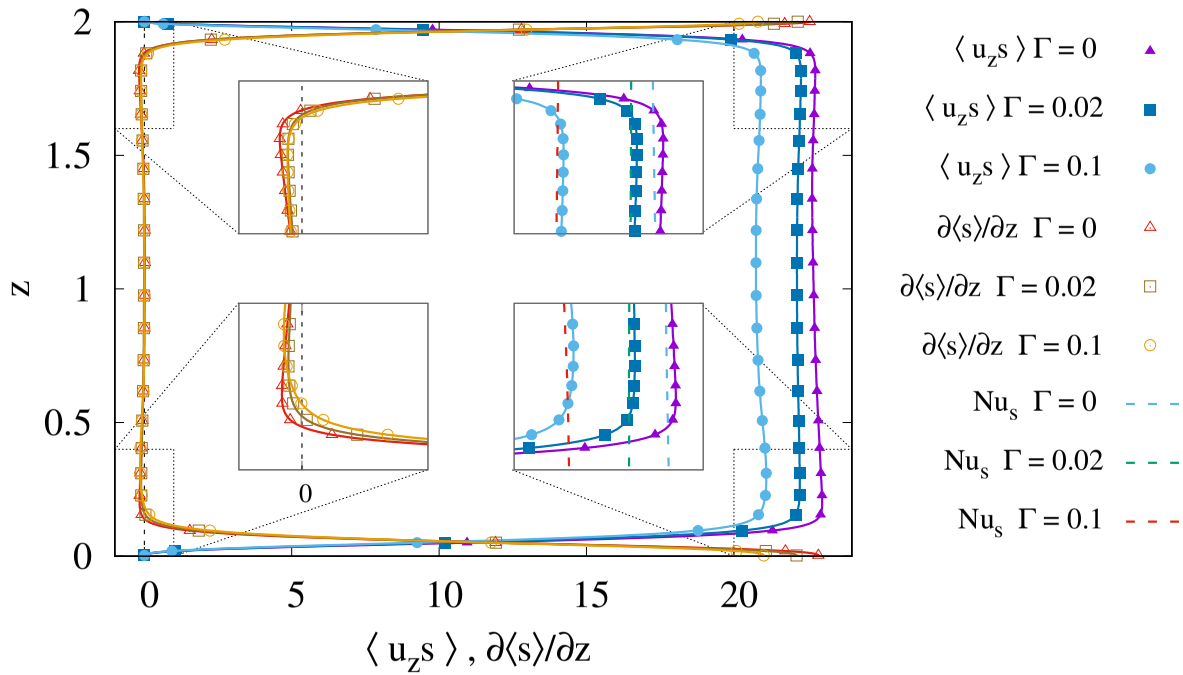

FIGURE 6.6 – Vertical behavior of salinity fluxes as a function of the vertical distance from the bottom boundary (z) for $\Gamma = 0$ (triangles), $\Gamma = 0.02$ (squares) and $\Gamma = 0.1$ (circles). Both the convective part ($\langle u_z s \rangle$, lines and filled symbols in blue scale) and the diffusive part ($\partial \langle s \rangle / \partial z$, lines and open symbols in red scale) to the total heat flux (q_s, corresponding to the dashed lines on the right-hand side insets of the plot) are shown. A vertical dotted line (zero line) is also added for clarity. The four insets provide a close-up view of the effect of shear on the salinity fluxes close to the boundaries: The two left-hand insets zoom into the region where the salinity diffusive flux becomes negative and highlight the slight reduction produced by shear; the two right-hand insets zoom in the region where the salinity convective flux flattens and highlight the reduction produced by shear.

the salinity flux can be discussed also considering the diffusive scaling introduced in Sec. 2.1. The comparison between corresponding values of Γ (which are significantly smaller than unity) and Γ_d (which are of order unity) leads us to hypothesize that indeed diffusive scales are more relevant than the convective scales as far as salinity transport is concerned.

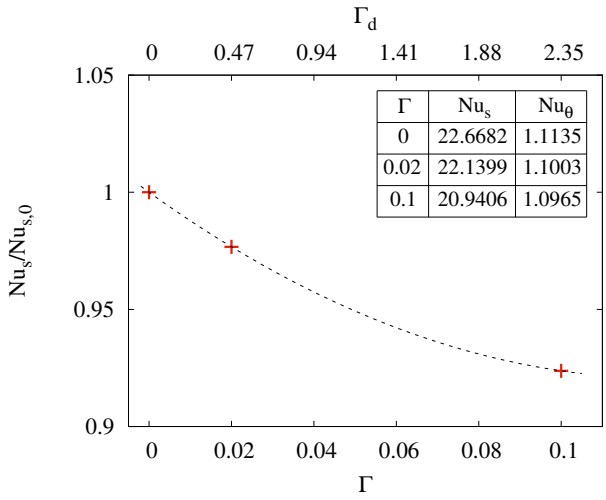

Γ	Nu_s	Nu_θ
0	22.6682	1.1135
0.02	22.1399	1.1003
0.1	20.9406	1.0965

FIGURE 6.7 – Salinity Nusselt number Nu_s normalized by Nu_s at $\Gamma = 0$ ($Nu_{s,0}$) as a function of the applied shear rate, indicated as Γ on the bottom horizontal axis and as Γ_d on the top horizontal axis. The table summarizes the values of Nu_s together with the values of the temperature Nusselt number, Nu_θ (not plotted).

The other important output parameters are the induced flows velocities, customarily measured by the horizontal and vertical Reynolds numbers:

$$\begin{aligned} Re_x &= \left(\frac{1}{4}\frac{Ra_s}{Pr_s}\right)^{\frac{1}{2}} \left(\frac{1}{V}\int {u_x}^2 dV\right)^{1/2}, \\ Re_y &= \left(\frac{1}{4}\frac{Ra_s}{Pr_s}\right)^{\frac{1}{2}} \left(\frac{1}{V}\int {u_y}^2 dV\right)^{1/2}, \\ Re_z &= \left(\frac{1}{4}\frac{Ra_s}{Pr_s}\right)^{\frac{1}{2}} \left(\frac{1}{V}\int {u_z}^2 dV\right)^{1/2}, \end{aligned} \tag{6.3}$$

or, simply, by the overall Reynolds number $Re = \sqrt{{Re_x}^2 + {Re_y}^2 + {Re_z}^2}$ [52, 133]. The value of the horizontal and vertical Reynolds numbers are summarized in Table 6.1. As expected, and also anticipated by the discussion of Fig. 6.5, we observe a significant increase of Re_x with Γ, accompanied by a slight increase of Re_y. No monotonic trend is observed for Re_z. However, considering the ratio $Re_z/Re_x = u_{z,rms}/u_{x,rms}$, we find $Re_z/Re_x \simeq 2$ when $\Gamma = 0$ but $Re_z/Re_x \simeq 0.15$ when $\Gamma = 0.1$. The decrease of Re_z/Re_x reflects a reduction of the vertical convective salinity flux and reveals that the structure of the fingers and their vertical velocity become weaker as the applied shear increases. It is indeed the reduced vertical velocity that weakens the vertical salinity

flux, which is the flux influenced by the velocity field: Temperature is essentially dominated by diffusion and remains almost unaltered upon application of the shear.

TABLE 6.1 – Horizontal and vertical Reynolds numbers as a function of the applied shear rate, Γ.

Γ	Re_x	Re_y	Re_z
0	0.28781	0.29117	0.57703
0.02	0.75536	0.32231	0.59546
0.1	3.66565	0.35609	0.56290

7

Concluding remarks and future developments

7.1 Conclusion

In this thesis, we first investigated the interaction between stable thermal stratification and turbulence in a confined configuration. We assessed the current physical description and parametrizations of stratified wall-bounded turbulence at high Reynolds number by running a series of DNS of stably-stratified channel flow at fixed Reynolds and Prandtl number ($Re_\tau = 1000$ and $Pr = 0.71$, respectively) and at different values of the shear Richardson number, up to $Ri_\tau = 300$. From a physical viewpoint, the simulation set up can be assimilated to the flow of air inside a channel of height $2h \sim 1.5\ m$ at a reference bulk Reynolds number (based on h) $Re_b = 2 \times 10^4$ and subject to a wall-to-wall temperature difference up to $\approx 10K$. For the considered range of Ri_τ, active turbulence is sustained close to the walls, where the strong mean shear generates small-scale vorticity that is not affected by the imposed stratification. Farther from the wall, where vortices and flow structures are larger, stratification has an important influence. Even for low-to-moderate levels of stratification, buoyancy effects dominate in this region, as the mean shear is small (the channel center is a symmetry plane). Interestingly, although temperature and wall-normal velocity fluctuations are very large at the channel center, their correlation – which represents the buoyancy flux – decreases so much that – for $Ri_\tau \geq 200$ – it becomes nearly zero. We show that this behavior is due to the presence of a $\approx \pi/2$ phase shift between the temperature fluctuations and the wall-normal velocity fluctuations that causes no correlation between the two signals. These findings are consistent with the presence of Internal Gravity Waves at the channel center. It is noteworthy to observe that, although hypothesized in previous works [54, 2], we did not find evidence of any mean countergradient heat flux, even at the largest stratification considered here. These results, however, can supply further motivation to examine this flow at even higher stratification levels. We also focused on the behavior of the overall momentum and heat transfer rates, represented by the friction factor, C_f, and the Nusselt number, Nu, respectively. We showed that the friction factor scales as $C_f \sim Ri_\tau^{-1/3}$, while the Nusselt number scales as $Nu \cdot Re_\tau^{-2/3} \sim Ri_\tau^{-1/3}$. We remark here that the current large-scale dataset of

stably-stratified channel turbulence at $Re_\tau = 1000$ are expected to help LES (Large Eddy Simulation) and RANS (Reynolds averaged Navier-Stokes) to build efficient and reliable subgrid scale and closure models for wall-bounded buoyancy-influenced turbulence [59]. Finally, by calculating different budget equations, we examined the effect of stratification on energetics. The most significant stratification influence occurs at the channel center, where the turbulence activity is completely suppressed. The turbulent viscous dissipation vanishes under the buoyancy effect in this narrow region. The influence of stratification on the near-wall region was only observed in the turbulent and molecular diffusion terms of the mean temperature variance budget. Such an effect in the near-wall region can be observed only in MTV budget, because the imposed stratification applied via a mean temperature difference on the walls. We also evaluated the mixing in wall-bounded stably-stratified turbulence by computing flux Richardson number based on three different definitions. Finally, we proposed a new parameterization for the irreversible flux Richardson number as a function of gradient Richardson number, which seems to perform better compared to the parameterization proposed by Venayagamoorthy & Koseff [127]. We speculate that the better performance of this parameterization is because our simulations include the effect of wall in the irreversible flux Richardson number.

Finally, we investigated the interaction of thermal and solutal stratification with shear, where the fluid layer experiences a solutal unstable stratification (slowly diffusing scalar) and a stable thermal stratification (rapidly-diffusing scalar) simultaneously. We performed fully-resolved three dimensional simulations of double diffusive convection in a confined fluid layer in the fingering regime to examine the influence of shear on heat and salinity transport fluxes: In particular, we focused on the modifications produced by shear on the diffusive and convective contributions to the total flux, which are investigated for the first time. In the present problem, temperature is the rapidly-diffusing scalar characterized by a stabilizing distribution across the fluid layer (the top boundary being set at a larger temperature compared to the bottom one), whereas salinity is the slowly-diffusing scalar characterized by a destabilizing distribution across the layer (the top boundary being set at a larger salinity compared to the bottom one). To simulate this flow configuration, we considered mixed slip/no-slip boundary conditions: Even in the absence of shear, these produce an asymmetric distribution of the diffusing scalars in the vertical direction that mimics the presence of a non-homogeneous convection layer. Simulations are run with fixed values of the salinity Rayleigh number $Ra_s = 10^7$, salinity Prandtl number $Pr_s = 700$, Lewis number $Le = 100$, and density ratio $\Lambda = 1$, whereas three different values of shear are considered: $\Gamma = 0$ (corresponding to zero shear), $\Gamma = 0.02$ and $\Gamma = 0.1$ (corresponding to a shearing velocity equal to one fiftieth and one tenth of the convective free-fall velocity of the fingers, respectively). In the reference case with zero shear, the flow is dominated by vertical elongated fingers that span the entire height of the fluid layer and transfer efficiently their salt concentration. The application of the shear at the top surface modifies both the size and the structure of the fingers, which appear weaker and aligned with the direction of shear. These flow modifications are found to have an influence on the global heat, salt and momentum transport. In particular, we document a global decrease of about 10% of the salinity Nusselt number (i.e. the dimensionless salinity transport coefficient) for the $\Gamma = 0.1$ case. Our analysis show

that such decrease may be due to the weakening of vertical convective flux observed for increasing Γ. The accurate methodology used in this thesis to investigate the problem of DDC under shear effect proved to be a powerful tool to analyze the complex interplay between diffusive and convective transport mechanisms in DDC and identify the key physical parameters of the problem.

7.2 Future development

There are various topics of interest that could be tackled in future as a follow-up of this thesis.

- **Wall-bounded stably-stratified turbulence**

  In terms of future works, some proposals could be suggested, such as applying a decomposition of the flow field, which can separate the turbulent fluctuations from the IGWs. Separating the large scale, coherent fluctuations from small scale incoherent ones would allow full characterization of the different contributions separately. A further investigation is also required for splitting the total potential energy into available and background potential energy. To this aim, long enough time averaging is required to close the available and background potential energy budget precisely. By separating the available potential energy from total energy, a direct measure of mixing can be evaluated. Investigating the flow field under the Non-Oberbeck-Boussinesq condition, arising when large temperature gradients are present or when the typical size of the involved flow scales is large, could also help for a more realistic understanding of stably-stratified wall-bounded turbulence. An additional improvement that would be interesting in the future is investigating the dispersion of heavy and light particles in wall-bounded stably-stratified turbulence. In the archival literature, the dispersion of heavy and light particles has been investigated extensively in the homogeneous stratified turbulence [125, 123, 124]. Recently, Zhang et al. [139] examined the dynamic of semi- and neutrally-buoyant particles in wall-bounded stably stratified turbulence.

- **Double diffusive and convection under shear effect**

  Further investigations are required to explore the impact of local counter-gradient diffusion mechanisms on the global flow parameters over a broader range of values of Γ and, in turn, to derive accurate scaling laws for the scalar transport fluxes. The follow-up of this thesis is running simulations of DDC with imposed shear at higher Ra_s numbers to investigate the interaction between fingering double diffusive convection turbulence with weak/moderate shear. Such simulations will require an increased number of computational grid points, which might be doable with employing an adaptive mesh refinement scheme to increase the resolution for the salinity field only. An adaptive mesh refinement strategy, however, contrasts with the pseudo-spectral discretization. Therefore, a different spatial discretization scheme should be adopted. In addition, an adaptive mesh refinement scheme would complicate the load balance at the simulation run time.

A

Variables scaling system

In the problem of stably-stratified turbulence, we have two different scaling systems. Since we deal with turbulence in this problem, all the valuables can be expressed in either inner (wall) or outer units. The outer scaling system is as follows:

$$x_i = \frac{x_i^*}{h^*}, \quad u_i = \frac{u_i^*}{u_\tau^*}, \quad t = \frac{t^* u_\tau^*}{h^*}, \quad \theta = \frac{\theta^* - \theta_0^*}{\Delta\theta^*/2}. \tag{A.1}$$

The variables in inner units are defined as:

$$x_i^+ = \frac{x_i^* u_\tau^*}{\nu^*}, \quad u_i = \frac{u_i^*}{u_\tau^*}, \quad t^+ = \frac{t^* {u_\tau^*}^2}{\nu^*}, \quad \Theta = \frac{\theta^* - \theta_w^*}{\theta_\tau^*}. \tag{A.2}$$

Throughout this thesis, the variables expressed in outer units are represented without superscripts. Superscripts have also been dropped for the velocity, as they have the same definition in both outer and wall units, and for temperature, since the dimensionless temperature is defined with different letters (small/capital letter) in the inner (θ) and outer (Θ) units. Time and position vector in wall units are presented with $^+$ superscript. For the problem of DDC, since we do not deal with turbulence, no inner and outer units are defined. All the variables are made dimensionless as follows:

$$\theta = \frac{\theta^* - \theta_0^*}{\frac{\Delta\theta^*}{2}}, \quad s = \frac{s^* - s_0^*}{\frac{\Delta s^*}{2}}, \quad u_i = \frac{u_i^*}{\sqrt{g^* \beta_s^* h^* (\Delta s^*/2)}}, \quad t = \frac{t^*}{\frac{h^*}{\sqrt{g^* \beta_s^* h^* (\Delta s^*/2)}}} \tag{A.3}$$

The only variable with two different scaling is the imposed shear. The two different scaling of the imposed shear is describes in detail in subsection 2.2.2.

B

Schematic representation of the numerical algorithm

Here we schematically represent the numerical algorithm employed to solve the problem of stratified turbulence and DDC. Since the solution procedure shares many similarities between the two problems, we introduced the numerical solution procedure only for the case of stratified turbulence in section 3.2. The main differences among the solver used for the problem of stratified turbulence and DDC are *i*) S-terms introduced in subsection 2.1.3 and subsection 2.2.1 are different. *ii*) An additional transport equation is solved for the salinity. A schematic representation of the numerical algorithm is shown in Fig. B.1. Note that symbols $\wedge$ and $\vee$ refer to logical "*and*" and "*or*".

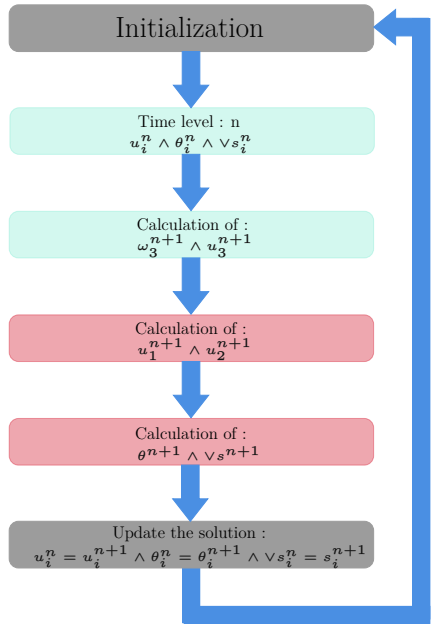

FIGURE B.1 – Schematic representation of the numerical solver.

C

Double diffusive convection validation

Validation refers to the case of DDC in a no-slip/no-slip box at $Ra_s = 10^7$, $Pr_s = 700$, $\Lambda = 2$ and $Le = 100$, which replicates one of the cases examined by Yang et al. [135]. In Fig. C.1, we show the three-dimensional volume rendering of the instantaneous flow structure (panel a) and the associated two-dimensional maps of the salinity distribution, taken at three different locations: Near the top boundary ($z = +0.95$, panel b); at the center ($z = 0$, panel c) and near the bottom boundary ($z = -0.95$, panel d). Table C.1 shows a comparison between the domain size and grid resolution of the two simulations, and table C.2 represent the global response parameters of the flow: salinity Nusselt number, Nu_s, temperature Nusselt number, Nu_θ, Reynolds number, Re, and salinity boundary layer thickness, $\lambda_s^*/2h^*$.

TABLE C.1 – Comparison of domain size and grid resolution.

	Present Simulation	Yang et al. [135]
Domain size	$\pi h^* \times \pi h^* \times 2h^*$	$4h^* \times 4h^* \times 2h^*$
Grid Resolution	$512 \times 512 \times 257$	$432 \times 432 \times 240$
Grid spacings	$\Delta x = \Delta y = 3.06 \cdot 10^{-3}$	$\Delta x = \Delta y = 4.63 \cdot 10^{-3}$
	$\Delta z_{min} = 7.53 \cdot 10^{-5}$	$\Delta z_{min} = 8.64 \cdot 10^{-5}$
	$\Delta z_{max} = 1.22 \cdot 10^{-2}$	$\Delta z_{max} = 1.31 \cdot 10^{-2}$

TABLE C.2 – Comparison of global response parameters.

	Present Simulation	Yang et al. [135]
Nu_s	18.26	18.33
Nu_θ	1.047	1.045
Re	0.5276	0.5770
$(\lambda_s^*/2h^*) \times 10^{-2}$	3.305	3.244

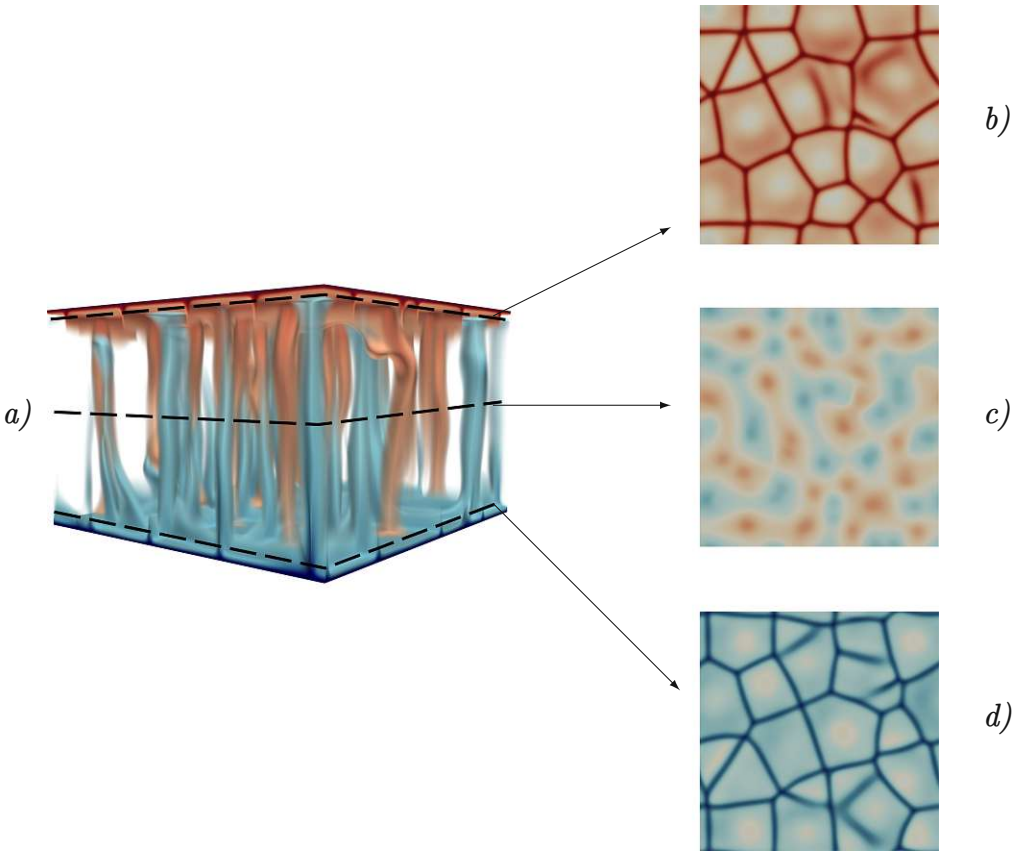

FIGURE C.1 – Three dimensional volume rendering of salinity field (panel a) and the associated two dimensional maps of salinity distribution, taken at three different locations: Near the top boundary ($z = +0.95$, panel b); at the center ($z = 0$, panel c) and near the bottom boundary ($z = -0.95$, panel d).

D

Publications, courses and projects

D.1 Refereed journals

J1 **P. Hadi Sichani**, F. Zonta and A. Soldati. Energetics and mixing in wall-bounded stably stratified turbulent flow at $Re_\tau = 1000$, *Phys. Rev. Fluids*, in preparation.

J2 F. Zonta, **P. Hadi Sichani** and A. Soldati. Interaction between thermal stratification and turbulence in channel flow. *J. Fluid Mech.*, under revision.

J3 **P. Hadi Sichani**, C. Marchioli, F. Zonta A. Soldati. Shear Effects on Scalar Transport in Double Diffusive Convection. *ASM J. Fluids Eng.*, 142:121105, 2020.

D.2 Conferences

C1 **P. Hadi Sichani**, F. Zonta, and A. Soldati, Increasing stratification in turbulent channel flow at $Re_\tau = 1000$, *APS-DFD Annual Meeting*, Phoenix (USA), November 21–23, 2021.

C2 **P. Hadi Sichani**, F. Zonta, C. Marchioli and A. Soldati, Ice melting in stratified shear turbulence, *APS-DFD Annual Meeting (Virtual)*, Chicago (USA), November 22–24, 2020.

C3 **P. Hadi Sichani**, C. Marchioli, F. Zonta and A. Soldati, Influence of shear on fingering dynamics in double diffusive convection, *APS-DFD Annual Meeting*, Seattle (USA), November 23–26, 2019.

C4 F. Zonta, **P. Hadi Sichani** and A. Soldati, Wall-bounded stably-stratified turbulence at high Reynolds number, *APS-DFD Annual Meeting*, Seattle (USA), November 23–26, 2019.

C5 F. Zonta, A. Soldati and **P. Hadi Sichani** Wall-bounded stably stratified turbulence at large Reynolds number, *ETC 2019 : 17th European Turbulence Conference*, Torino (Italy), September 3–6, 2019.

C6 F. Zonta, A. Soldati and **P. Hadi Sichani** Wall-bounded stably stratified turbulence at large Reynolds number, *WITGAF 2019 : Waves, Instabilities and Turbulence in Geophysical and Astrophysical Flows*, Cargèse (France), July 8–19, 2019.

C7 F. Zonta, **P. Hadi Sichani** and A. Soldati, Wall-bounded stably stratified turbulence at large Reynolds number, *AHPC 2019 : Austrian HPC Meeting*, Grundlsee (Austria), February 25–27, 2019.

C8 **P. Hadi Sichani**, F. Zonta, A. Obabko and A. Soldati, Stably-stratified wall-bounded turbulence, *APS-DFD Annual Meeting*, Denver (USA), November 19–21, 2017.

D.3 HPC projects

P1 **Double diffusive convection in shear-driven flow (DODICOS)** (PRACE grant), 10 millions CPU hours on TGCC Joliot Curie at CEA, Chemin du Ru, Bruyères-le-Châtel, (France), 2020.

P2 **Shear effects on double diffusive convection (SEDODFIC)** (ISCRA grant), project ID: HP10BLYZ3C, ∼1 million CPU hours on Marconi100 hosted at CINECA, Casalecchio di Reno (Italy), 2019.

D.4 Advanced courses

A1 **CISM- Physics of Granular Suspensions: Micro-Mechanics of Geophysical Flows**, International Center for Mechanical Sciences (CISM), Udine (Italy), June 14–18, 2021. Coordinated by M. Mazzuoli & L. Lacaze.

A2 **CISM- Advanced Numerical Approaches for Simulation of Turbulent Multiphase Flows**, International Center for Mechanical Sciences (CISM), Udine (Italy), September 7–11, 2020. Coordinated by C. Marchioli & F. Zonta.

A3 **CISM- Advances in Dispersed Multi-Phase Flows: from Measuring to Modeling"**, International Center for Mechanical Sciences (CISM), Udine (Italy), July 15–19, 2019. Coordinated by F. Coletti & R. Zamansky.

A4 **CISM-AIMETA Advanced School on "Anisotropic Particles in Viscous and Turbulent Flows"**, International Center for Mechanical Sciences (CISM), Udine (Italy), July 1–5, 2019. Coordinated by C. Marcchioli & G. Verhille.

A5 **CISM-ECCOMAS International Summer School on "Coherent Structures in Unsteady Flows: Mathematical and Computational Methods"**, International Center for Mechanical Sciences (CISM), Udine (Italy), June 3–7, 2019. Coordinated by G. Haller.

A6 **CISM-JMBC Course on Complex Flows and Complex Fluids**, International Center for Mechanical Sciences (CISM), Udine (Italy), May 13–17, 2019. Coordinated by F. Toschi.

A7 **Advanced school on parallel computing**, CINECA, Bologna (Italy), February 11–15, 2019.

A8 **VSC Training Course: Parallelization with MPI**, Vienna Scientific Cluster (VSC), Vienna (Austria), November 7–9, 2018.

A9 **VSC Training Course: Shared memory parallelization with OpenMP**, Vienna Scientific Cluster (VSC), Vienna (Austria), November 5–6, 2018.

Acknowledgements

Foremost, I would like to thank my Ph.D. supervisors, Prof. Alfredo Soldati and Prof. Cristian Marchioli, who made this work possible and gave me the opportunity to work on such a fascinating topic under their supervision. I also would like to thank my co-supervisor, Dr. Francesco Zonta, for his patient guidance, encouragement, and advice throughout this work. I was fortunate to have a co-supervisor who cared so much about my work and promptly responded to my questions and queries. I learned a lot from him, from a scientific viewpoint, and about different life aspects during the past six years we have known each other. A special thank goes to the committee members and reviewers, who spent time reviewing my Ph.D. thesis carefully. Their insightful observations, suggestions and feedback have been greatly appreciated. I would also like to thank Alessio and Giovanni for their helpful suggestions on my work. Among the people who accompanied me during this experience, I would like to thank Mobin and Arash. I would also like to extend my gratitude to my friend, Sadegh. A final thank goes to those who did not support me during this work. They have also been a source of motivation for me during past years in some special ways.

Bibliography

[1] F. Alcántara-Ávila, S. Hoyas, and M. Jezabel Pérez-Quiles. Direct numerical simulation of thermal channel flow for $re_\tau = 5000$ and $pr = 0.71$. *J. Fluid Mech.*, 916:A29, 2021.

[2] V. Armenio and S. Sarkar. An investigation of stably stratified turbulent channel flow using large-eddy simulation. *J. Fluid Mech.*, 459:1–42, 2002.

[3] S. P. S. Arya. Buoyancy effects in an horizontal flat-plane boundary layer. *J. Fluid Mech.*, 68:321–343, 1975.

[4] V.E. Badalassi, H.D. Ceniceros, and S. Banerjee. Computation of multiphase systems with phase field models. *J. Comput. Phys*, 190(2):371–397, 2003.

[5] J. H. Bae, J. Y. Yoo, and Choi H. Direct numerical simulation of turbulent supercritical flows with heat transfer. *Phys. Fluids*, 17:105104, 2005.

[6] N. J. Balmforth, S. A. Ghadge, A. Kettapun, and S. D. Mandre. Bounds on double-diffusive convection. *J. Fluid Mech.*, 569:29–50, 2006.

[7] G.K. Batchelor. *An introduction to fluid dynamics*. Cambridge University Press, 1967.

[8] A. Bejan. *Convection Heat Transfer*. Wiley, 1984.

[9] R. B. Bird, W. E. Stewart, and E. N. Lightfoot. *Transport phenomena*. John Wiley and Sons, 2007.

[10] R. Bolgiano. Turbulent spectra in a stable stratified atmosphere. *J. Geophys. Res.*, 64:2226–2229, 1959.

[11] J. Boussinesq. *Theorie analytique de la chaleur*. Gauthier-Villars, 1903.

[12] G. Brethouwer, Y. Duguet, and P. Schlatter. Turbulent-laminar coexistence in wall flows with coriolis, buoyancy or lorentz forces. *J. Fluid Mech.*, 704:137–172, 2012.

[13] R.E. Britter. *An experiment on turbulence in a density stratified fluid*. PhD thesis, 1974.

[14] C. Canuto, M.Y. Hussaini, A.M. Quarteroni, and T.A. Zang. *Spectral Methods in Fluid Dynamics*. Springer-Verlag, 1988.

[15] C. P. Caulfield. Layering, instabilities, and mixing in turbulent stratified flows. *Annu. Rev. Fluid Mech.*, 53:113–145, 2021.

[16] A.B. Cortesi, G. Yadigaroglu, and S. Banerjee. Numerical investigation of the formation of three-dimensional structures in stably-stratified mixing layers. *Phys. Fluids*, 10(6):1449–1473, 1998.

[17] E. Deusebio, C. P. Caulfield, and J. R. Taylor. The intermittency boundary in stratified plane couette flow. *J. Fluid Mech.*, 781:298–329, 2015.

[18] J. M. M. Donda, I. G. S. van Hooijdonk, A. F. Moene, H. J. J. Jonker, G. J. F. van Heijst, H. J. H. Clercx, and B. J. H. van de Wiel. Collapse of turbulence in stably stratified channel flow: a transient phenomenon. *Q. J. R. Meteorol. Soc.*, 141:2137–2147.

[19] V. Dostal, P. Hejzlar, and M.J. Driscoll. The supercritical carbon dioxide power cycle: comparison to other advanced power cycles. *Nucl. Technol.*, 154:283–301, 2006.

[20] T. H. Ellison. Turbulent transport of heat and momentum from an infinite rough plane. *J. Fluid Mech.*, 2:456–466, 1957.

[21] A. M. Fernandes and R. Krishnamurti. Salt finger fluxes in a laminar shear flow. *J. Fluid Mech.*, 658:148–165, 2010.

[22] H. J. S. Fernando. Turbulent mixing in stratified fluids. *Annu. Rev. Fluid Mech.*, 23:455–493, 1991.

[23] J. H. Ferziger, J. R. Koseff, and S. G. Monismith. Numerical simulation of geophysical turbulence. *Comput. Fluids*, 31:557–568, 2002.

[24] L. Fox and I. B. Parker. *Chebyshev Polynomials in Numerical Analysis.* Oxford University Press, 1968.

[25] M. Frigo and S.G. Johnson. The design and implementation of FFTW3. *Proceedings of the IEEE*, 93(2):216–231, 2005. Special issue on "Program Generation, Optimization, and Platform Adaptation".

[26] K. S. Gage and W. H. Reid. The stability of thermally stratified plane poiseuille flow. *J. Fluid Mech.*, 33:21–32, 1968.

[27] P. Garaud. Double-diffusive convection at low prandtl number. *Annual Review of Fluid Mechanics*, 50(1):275–298, 2018.

[28] M. García-Villalba and J. C. del Álamo. Turbulence modification by stable stratification in channel flow. *Phys. Fluids*, 23(045104), 2011.

[29] R. P. Garg, J. H. Ferziger, S. G. Monismith, and J. R. Koseff. Stably stratified turbulent channel flows. i. stratification regimes and turbulence suppression mechanism. *Phys. Fluids*, 12, 2000.

[30] B. Gayen, R.W. Griffiths, G.O. Hughes, and J.A. Saenz. Energetics of horizontal convection. *J. Fluid Mech.*, 716:R10, 2013.

[31] B. Gayen, G.O. Hughes, and R.W. Griffiths. Completing the mechanical energy pathways in turbulent rayleigh-bénard convection. *Phys. Rev. Lett.*, 111:124301, 2013.

[32] B. Gebhart, Y. Jaluria, R. L. Mahajan, and B. Sammakia. *Buoyancy-induced flows and transport.* Hemisphere Publishing Corporation, 1988.

[33] A. A. Grachev, E. L. Andreas, C. W. Fairall, P. S. Guest, and P. O. G. Persson. On the turbulent prandtl number in the stable atmospheric boundary layer. *Boundary-Layer Meteorology*, 125(2):329–341, 2007.

[34] D.D. Gray and A. Giorgini. The validity of the boussinesq approximation for liquids and gases. *Int. J. Heat Mass Transfer*, 19:545–551, 1976.

[35] M. C. Gregg. Diapycnal mixing in the thermocline. *A review. J. Geophys. Res.*, 92:5249–5286, 1987.

[36] P. Hadi Sichani, C. Marchioli, F. Zonta, and A. Soldati. Shear effects on scalar transport in double diffusive convection. *ASME J. Fluids Eng.*, 142:121105, 2020.

[37] E. Hage and A. Tilgner. High rayleigh number convection with double diffusive fingers. *Phys. of Fluids*, 22(7):076603, 2010.

[38] P. He. A high order finite difference solver for massively parallel simulations of stably stratified turbulent channel flows. *Comput. Fluids*, 127:161–173, 2016.

[39] S.E. Holt, J.R. Koseff, and J.H. Ferziger. A numerical study of the evolution and structure of homogeneous stably stratified sheared turbulence. *J. Fluid Mech.*, 237:499–539, 1992.

[40] C. J. Howland, J. R. Taylor, and C. P. Caulfield. Mixing in forced stratified turbulence and its dependence on large-scale forcing. *J. Fluid Mech.*, 898:A7, 2020.

[41] G.O. Hughes, A. Mc C. Hogg, and R.W. Griffiths. Available potential energy and irreversible mixing in the meridional overturning circulation. *J. Phys. Oceanogr.*, 39:3130 – 3146, 2009.

[42] G.O. Hughes, B. Gayen, and R.W. Griffiths. Available potential energy in rayleigh–bénard convection. *J. Fluid Mech.*, 729:R3, 2013.

[43] S. G. Huisman, D. P. M. van Gils, S. Grossmann, C. Sun, and D. Lohse. Ultimate turbulent taylor-couette flow. *Phys. Rev. Lett.*, 108(024501), 2012.

[44] A. K. M. F. Hussain and W. C. Reynolds. The mechanics of an organized wave in turbulent shear flow. *J. Fluid Mech.*, 41:241–258, 1970.

[45] M.Y. Hussaini and T.A. Zang. Spectral methods in fluid dynamics. *Annu. Rev. Fluid Mech.*, 19(1):339–367, 1987.

[46] O. Iida, N. Kasagi, and Y. Nagano. Direct numerical simulation of turbulent channel flow under stable density stratification. *Intl. J. Heat Mass Transfer*, 45, 2002.

[47] E. C. Itsweire, J. R. Koseff, D. A. Briggs, and J. H. Ferziger. Turbulence in stratified shear flows: Implications for interpreting shear-induced mixing in the ocean. *J. Phys. Oceanogr.*, 23:1508 – 1522, 1993.

[48] G. N. Ivey and Imberger J. On the nature of turbulence in a stratified fluid. part i: The energetics of mixing. *J. Phys. Oceanogr.*, 21:650 – 658, 1991.

[49] G.N. Ivey, K.B. Winters, and J.R. Koseff. Density stratification, turbulence, but how much mixing? *Annu. Rev. Fluid Mech.*, 40:169–184, 2008.

[50] F. Karimpour and S. K. Venayagamoorthy. A simple turbulence model for stably stratified wall-bounded flows. *J. Geophys. Res.*, 119:870–880, 2014.

[51] N. Kasagi, Y. Tomita, and A. Kuroda. Direct numerical simulation of passive scalar field in a turbulent channel flow. *J. Heat Transf.*, 114:598–606, 1992.

[52] M. Kellner and A. Tilgner. Transition to finger convection in double-diffusive convection. *Phys. of Fluids*, 26(9):094103, 2014.

[53] M.P. Kirkpatrick, N. Williamson, S. W. Armfield, and V. Zecevic. Evolution of thermally stratified turbulent open channel flow after removal of the heat source. *J. Fluid Mech.*, 876:356–412, 2019.

[54] S. Komori, H. Ueda, F. Ogino, and T. Mizushina. Turbulence structure in stably stratified open-channel flow. *J. Fluid Mech.*, 130:13–26, 1983.

[55] N. Konopliv, L. Lesshafft, and E. Meiburg. The influence of shear on double-diffusive and settling-driven instabilities. *J. Fluid Mech.*, 849:902–926, 2018.

[56] L. V. Krishnamoorthy and R. A. Antonia. Temperature-dissipation measurements in a turbulent boundary layer. *J. Fluid Mech.*, 176:265–281, 1987.

[57] P. K. Kundu, I. M. Cohen, and D. R. Dowling. *Fluid Mechanics 5th Edition.* Academic Press, 2011.

[58] B.E. Launder and D.B. Spalding. *Mathematical Models of Turbulence.* Academic Press, 1972.

[59] W. M. J. Lazeroms, G. Brethouwer, S. Wallin, and A. V. Johansson. An explicit algebraic reynolds-stress and scalar-flux model for stably stratified flows. *J. Fluid Mech.*, 723:91–125, 2013.

[60] C. Lee, K. Chang, J. H. Lee, and K. J. Richards. Vertical mixing due to double diffusion in the tropical western pacific. *Geophysical Research Letters*, 41(22): 7964–7970, 2014.

[61] D. K. Lilly. Stratified turbulence and the mesoscale variability of the atmosphere. *J. Atmos. Sci.*, 40(3):749 – 761, 1983.

[62] E. Lindborg. The energy cascade in a strongly stratified fluid. *J. Fluid Mech.*, 550:207–242, 2006.

[63] P. F. Linden. Salt fingers in a steady shear flow. *Geophysical Fluid Dynamics*, 6(1):1–27, 1974.

[64] P. F. Linden. The formation of banded salt finger structure. *J. Geophys. Res.*, 83(C6):2902–2912, 1978.

[65] C.J. Lloyd, R.M. Dorrell, and C.P. Caulfield. The coupled dynamics of internal waves and hairpin vortices in stratified plane poiseuille flow. *J. Fluid Mech.*, 934:A10, 2022.

[66] I. D. Lozovatsky and H. J. S. Fernando. Mixing efficiency in natural flows. *Phil. Trans. R. Soc.*, 371, 2013.

[67] S. L. Lyons, T. J. Hanratty, and J. B. McLaughlin. Direct numerical simulation of passive heat transfer in a turbulent channel flow. *Intl. J. Heat Mass Transfer*, 34:1149–1161, 1991.

[68] N. N. Mansour, J. Kim, and P. Moin. Reynolds-stress and dissipation-rate budgets in a turbulent channel flow. *J. Fluid Mech.*, 194:15–44, 1988.

[69] George L. Mellor and Tetsuji Yamada. Development of a turbulence closure model for geophysical fluid problems. *Rev. Geophys.*, 20:851–875, 1982.

[70] J. M. Mihaljan. A rigorous exposition of the boussinesq approximations applicable to a thin layer of fluid. *Astrophys J.*, 136:1126–1133, 1962.

[71] John W. Miles. On the stability of heterogeneous shear flows. *J. Fluid Mech.*, 10:496–508, 1961.

[72] R. Moestam and L. Davidson. Numerical simulations of thermocline in a pressure-driven flow between two infinite horizontal plates. *Phys. Fluids*, 17 (075109), 2005.

[73] A. S. Monin and A. M. Obukhov. Basic laws of turbulent mixing in the surface layer of the atmosphere. *Contrib. Geophys. Inst. Acad. Sci. USSR*, 151(163–187), 1954.

[74] H. Nemati, Patel A., B. J. Boersma, and Pecnik R. Mean statistics of a heated turbulent pipe flow at supercritical pressure. *Intl. J. Heat Mass Transfer*, 83: 741–752, 2015.

[75] J. J. Niemela. High rayleigh number thermal convection. *J. Low Temp. Phys.*, 134:447–456, 2004.

[76] J. J. Niemela and K. Sreenivasan. The use of cryogenic helium for classical turbulence: promises and hurdles. *J. Low Temp. Phys.*, 143:163–212, 2006.

[77] A. Oberbeck. Über die wärmeleitung der flüssigkeiten bei berücksichtigung der strömungen infolge von temperaturdifferenzen. *Ann. Phys. Chem.*, 243:271–292, 1879.

[78] Y. Ohya, D. Neff, and R. Meroney. Turbulence structure in a stratified boundary layer under stable conditions. *Bound.-Layer Meteorol.*, 83(139–161), 1997.

[79] D. G. Ortiz-Suslow, J. Kalogiros, R. Yamaguchi, and Q. Wang. An evaluation of the constant flux layer in the atmospheric flow above the wavy air-sea interface. *J. Geophys. Res.-Atmos.*, 126:e2020JD032834, 2021.

[80] T. R. Osborn. Estimates of the local rate of vertical diffusion from dissipation measurements. *J. Phys. Oceanogr.*, 10:83–89, 1980.

[81] T. R. Osborn and C. S. Cox. Oceanic fine structure. *Geophys. Astrophys. Fluid Dyn.*, 3:321–345, 1972.

[82] F. Paparella and J. Von Hardenberg. Clustering of salt fingers in double-diffusive convection leads to staircase like stratification. *Phys. Rev. Lett.*, 109(1):014502, 2012.

[83] W. R. Peltier and C. P. Caulfield. Mixing efficiency in stratified shear flows. *Annu. Rev. Fluid Mech.*, 35:135–167, 2003.

[84] R. Peyret. *Spectral Methods for Incompressible Viscous Flow*, volume 148. Springer Science+Business Media, 2002.

[85] P. Piccirillo and C. W. Van Atta. The evolution of a uniformly sheared thermally stratified turbulent flow. *J. Fluid Mech.*, 334:61–86, 1997.

[86] S. S. Pitla, D. M. Robinson, E. A. Groll, and S. Ramadhyani. Heat transfer from supercritical carbon dioxide in tube flow: a critical review. *Hvac&R Res.*, 4:281–301, 2006.

[87] M. Pons and P. Le Quéré. Modeling natural convection with the work of pressure-forces: a thermodynamic necessity. *Int. J. Numer. Meth. Fluids*, 13:322–332, 2007.

[88] S.B. Pope. *Turbulent Flows*. Cambridge University Press, 2000.

[89] L. Prandtl. 7. bericht über untersuchungen zur ausgebildeten turbulenz. *ZAMM - Journal of Applied Mathematics and Mechanics / Zeitschrift für Angewandte Mathematik und Mechanik*, 5(2):136–139, 1925.

[90] T. Radko. *Double-Diffusive Convection*. Cambridge University Press, United States of America, New York, 2013.

[91] T. Radko and M.E. Stern. Finite-amplitude salt fingers in a vertically bounded layer. *J. Fluid Mech.*, 425:133–160, 2000.

[92] T. Radko, J. Ball, J. Colosi, and J. Flanagan. Double-diffusive convection in a stochastic shear. *J. Phys. Oceanogr.*, 45(12):3155–3167, 2015.

[93] J.J. Riley and M.-P. Lelong. Fluid motions in the presence of strong stable stratification. *Annu. Rev. Fluid Mech.*, 32(1):613–657, 2000.

[94] A. Roccon, F. Zonta, and A. Soldati. Energy balance in lubricated drag-reduced turbulent channel flow. *J. Fluid Mech.*, 911:A37, 2021.

[95] J. J. Rohr, E. C. Itsweire, K. N. Helland, and C. W. Van Atta. Growth and decay of turbulence in a stably stratified shear flow. *J. Fluid Mech.*, 195:77–111, 1988.

[96] H. Salehipour and W. R. Peltier. Diapycnal diffusivity, turbulent prandtl number and mixing efficiency in boussinesq stratified turbulence. *J. Fluid Mech.*, 775: 464–500, 2015.

[97] J. A. Salmond and I. G. McKendry. A review of turbulence in the very stable nocturnal boundary layer and its implications for air quality. *Prog. Physical. Geog.*, 29(171–188), 2005.

[98] A. Sameen, Verzicco R., and Sreenivasan K. R. Specific role of fluid properties in non-boussinesq thermal convection at the rayleigh number of 2×10^8. *Europhys. Lett.*, 86:14006, 2009.

[99] I. Sandu, A. Beljaars, P. Bechtold, T. Mauritsen, and G. Balsamo. Why is it so difficult to represent stably stratified conditions in numerical weather prediction (nwp) models? *J. Adv. Model. Earth Syst.*, 5(117–133), 2013.

[100] R. W. Schmitt. Finger puzzles. *J. Fluid Mech.*, 692:1–4, 2012.

[101] A. Scotti and B. White. Diagnosing mixing in stratified turbulent flows with a locally defined available potential energy. *J. Fluid Mech.*, 740:114–135, 2014.

[102] X.-D. Shang, P. Tong, and K.-Q. Xia. Test of steady-state fluctuation theorem in turbulent rayleigh-bénard convection. *Phys. Rev. E*, 72(1):015301, 2005.

[103] L. H. Shih, J. R. Koseff, G. N. Ivey, and J. H. Ferziger. Parameterization of turbulent fluxes and scales using homogeneous sheared stably stratified turbulence simulations. *J. Fluid Mech.*, 525:193–214, 2005.

[104] W. D. Smyth and S. Kimura. Instability and diapycnal momentum transport in a double-diffusive, stratified shear layer. *J. Phys. Oceanogr.*, 37:1551–1565, 2007.

[105] W. D. Smyth and S. Kimura. Mixing in a moderately sheared salt-fingering layer. *J. Phys. Oceanogr.*, 41(7):1364–1384, 2011.

[106] W.D. Smyth and J.N. Moum. Length scales of turbulence in stably stratified mixing layers. *Phys. Fluids*, 12(6):1327–1342, 2000.

[107] W.D. Smyth and J.N. Moum. Anisotropy of turbulence in stably stratified mixing layers. *Phys. Fluids*, 12(6):1343–1362, 2000.

[108] A. Soldati and S. Banerjee. Turbulence modification by large-scale organized electrohydrodynamic flows. *Phys. Fluids*, 10:1742–1756, 1998.

[109] T. Sommer, J. R. Carpenter, and A. Wüest. "Double-diffusive" interfaces in lake kivu reproduced by direct numerical simulations. *Geophysical Research Letters*, 41(14):5114–5121, 2014.

[110] E. A. Spiegel and Veronis G. On the boussinesq approximation for a compressible fluid. *Astrophys J.*, 131:442–447, 1960.

[111] C. Staquet and J. Sommeria. Internal gravity waves: From instabilities to turbulence. *Annu. Rev. Fluid Mech.*, 34:559–593, 2002.

[112] M. E. Stern. The "salt-fountain" and thermohaline convection. *Tellus*, 12(2): 172–175, 1960.

[113] G. I. Taylor. I. eddy motion in the atmosphere. *Phil. Trans. R. Soc. Series A*, 215:1–26, 1915.

[114] J. Taylor and P. Bucens. Laboratory experiments on the structure of salt fingers. *Deep-Sea Res.*, 36(11):1675–1704, 1989.

[115] J.R. Taylor, S. Sarkar, and V. Armenio. Large eddy simulation of stably stratified open channel flow. *Phys. Fluids*, 17:116602, 2005.

[116] H. Tennekes and J. Lumley. *A first course in turbulence.* Cambridge, MA: MIT Press, 1972.

[117] S. Thangam, Z. Abdelfattah, and C. F. Chen. Salt-finger convection in shear flow. *Physics of Fluids*, 27:804–811, 1984.

[118] D. J. Tritton. *Physical fluid dynamics.* Oxford University Press, 1988.

[119] David J Tritton. *Physical fluid dynamics.* Springer Science & Business Media, 2012.

[120] J. S. Turner. Salt fingers across a density interface. *Deep-Sea Res.*, 14(5):599–611, 1967.

[121] J. S. Turner. *Buoyancy Effects in Fluids.* Cambrodge University Press, 1973.

[122] Hugo N. Ulloa, Alfred Wüest, and Damien Bouffard. Mechanical energy budget and mixing efficiency for a radiatively heated ice-covered waterbody. *J. Fluid Mech.*, 852:R1, 2018.

[123] M. van Aartrijk and H. J. H. Clercx. Dispersion of heavy particles in stably stratified turbulence. *Phys. Fluids*, 21:033304, 2009.

[124] M. van Aartrijk and H. J. H. Clercx. Vertical dispersion of light inertial particles in stably stratified turbulence: The influence of the basset force. *Phys. Fluids*, 22:013301, 2010.

[125] M. van Aartrijk, H. J. H. Clercx, and K. B. Winters. Single-particle, particle-pair, and multiparticle dispersion of fluid particles in forced stably stratified turbulence. *Phys. Fluids*, 20(2), 2008.

[126] S. K. Venayagamoorthy and D. D. Stretch. On the turbulent prandtl number in homogeneous stably stratified turbulence. *J. Fluid Mech.*, 644:359–369, 2010.

[127] S.K. Venayagamoorthy and J.R. Koseff. On the flux richardson number in stably stratified turbulence. *J. Fluid Mech.*, 798:R1, 2016.

[128] M. G. Wells, R. G. Griffiths, and J. S. Turner. Generation of density fine structure by salt fingers in a spatially periodic shear. *J. Geophys. Res.*, 106:7027–7037, 2001.

[129] O. Williams, T. Hohman, T. Van Buren, E. Bou-Zeid, and A. J. Smits. The effect of stable thermal stratification on turbulent boundary layer statistics. *J. Fluid Mech.*, 812:1039–1075, 2017.

[130] N. Williamson, S. W. Armfield, M. P. Kirkpatrick, and S. E. Norris. Transition to stably stratified states in open channel flow with radiative surface heating. *J. Fluid Mech.*, 766:528–555, 2015.

[131] K.B. Winters, P.N. Lombard, J.J. Riley, and E.A. D'Asaro. Available potential energy and mixing in density-stratified fluids. *J. Fluid Mech.*, 289:115–128, 1995.

[132] Y. Yang, E. P. Van Der Poel, R. Ostilla-Mónico, C. Sun, R. Verzicco, S. Grossmann, and D. Lohse. Salinity transfer in bounded double diffusive convection. *J. Fluid Mech.*, 768:476–491, 2015.

[133] Y. Yang, R. Verzicco, and D. Lohse. From convection rolls to finger convection in double-diffusive turbulence. *Proceedings of the National Academy of Sciences*, 113(1):69–73, 2016.

[134] Y. Yang, R. Verzicco, and D. Lohse. Vertically bounded double diffusive convection in the fingering regime: comparing no-slip versus free-slip boundary conditions. *Phys. Rev. Lett.*, 117(18), 2016.

[135] Y. Yang, R. Verzicco, and D. Lohse. Scaling laws and flow structures of double diffusive convection in the finger regime. *J. Fluid Mech.*, 802:667–689, 2016.

[136] Y. Yang, R. Verzicco, and D. Lohse. Two-scalar turbulent "Rayleigh-Bénard" convection: numerical simulations and unifying theory. *J. Fluid Mech.*, 848: 648–659, 2018.

[137] K. Yeo, B. G. Kim, and C. Lee. Eulerian and lagrangian statistics in stably stratified turbulent channel flows. *J. Turbul.*, 10:1–26, 2009.

[138] P. Yue, J.J. Feng, C. Liu, and J. Shen. A diffuse-interface method for simulating two-phase flows of complex fluids. *J. Fluid Mech.*, 515(1):293–317, 2004.

[139] X. Zhang, F. Zonta, Z.F. Tian, G.J. Nathan, R.C. Chin, and A. Soldati. Dynamics of semi- and neutrally-buoyant particles in thermally stratified turbulent channel flow. *Int. J. Multiph. Flow*, 139:103595, 2021. ISSN 0301-9322.

[140] F. Zonta. Nusselt number and friction factor in thermally stratified turbulent channel flow under non-oberbeck-boussinesq conditions. *Intl. J. Heat Fluid Flow*, 44:489–494, 2013.

[141] F. Zonta and S. Chibbaro. Entropy production and fluctuation relation in turbulent thermal convection. *Europhys. Lett.*, 114(50011), 2016.

[142] F. Zonta and A. Soldati. Stably stratified wall-bounded turbulence. *ASME Appl. Mech. Rev.*, 70, 2018.

[143] F. Zonta, C. Marchioli, and A. Soldati. Modulation of turbulence in forced convection by temperature-dependent viscosity. *J. Fluid Mech.*, 697:150–174, 2012.

[144] F. Zonta, M. Onorato, and A. Soldati. Turbulence and internal waves in stably-stratified channel flow with temperature-dependent fluid properties. *J. Fluid Mech.*, 697:175–203, 2012.